

# Low-energy microscopic models for iron-based superconductors: a review

Rafael M. Fernandes and Andrey V. Chubukov

*School of Physics and Astronomy, University of Minnesota, Minneapolis 55455, USA*

The development of sensible microscopic models is essential to elucidate the normal-state and superconducting properties of the iron-based superconductors. Because these materials are mostly metallic, a good starting point is an effective low-energy model that captures the electronic states near the Fermi level and their interactions. However, in contrast to cuprates, iron-based high- $T_c$  compounds are multi-orbital systems with Hubbard and Hund interactions, resulting in a rather involved 10-orbital lattice model. Here we review different minimal models that have been proposed to unveil the universal features of these systems. We first review minimal models defined solely in the orbital basis, which focus on a particular subspace of orbitals, or solely in the band basis, which rely only on the geometry of the Fermi surface. The former, while providing important qualitative insight into the role of the orbital degrees of freedom, do not distinguish between high-energy and low-energy sectors and, for this reason, generally do not go beyond mean-field. The latter allow one to go beyond mean-field and investigate the interplay between superconducting and magnetic orders as well as Ising-nematic order. However, they cannot capture orbital-dependent features like spontaneous orbital order. We then review recent proposals for a minimal model that operates in the band basis but fully incorporates the orbital composition and symmetries of the low-energy excitations. We discuss the results of the renormalization group study of such a model, particularly of the interplay between superconductivity, magnetism, and spontaneous orbital order, and compare theoretical predictions with experiments on iron pnictides and chalcogenides. We also discuss the impact of the glide-plane symmetry on the low-energy models, highlighting the key role played by the spin-orbit coupling.

## CONTENTS

I. Introduction	1	5. Inclusion of the $d_{xy}$ orbital contribution and 5-pocket model	28
II. Orbital-basis models	4	D. Ising-nematic order vs orbital order	29
A. Non-interacting Hamiltonian	5	V. 1-Fe versus 2-Fe unit cells	29
1. Five-orbital model	5	A. Orbital-basis models	31
2. Two-orbital model	5	B. Orbital-projected band models	32
3. Three-orbital model	6	VI. Concluding remarks	33
B. Order parameters	7	Acknowledgments	33
C. Interaction effects	8	A. Band dispersion parameters	34
III. Band-basis models	9	1. Five-orbital model	34
A. Non-interacting Hamiltonian	10	2. Two-orbital model	34
B. Order parameters	11	3. Three-orbital model	35
C. Interaction effects	12	4. Orbital-projected band model	35
1. Renormalization Group (RG) analysis: the basics	12	References	36
2. Two-band model	13		
3. Three-band model	14		
IV. Orbital-projected band models	18		
A. Non-interacting Hamiltonian	18		
B. Order parameters	21		
1. SDW and CDW orders	21		
2. SC order	21		
3. $\mathbf{Q} = 0$ orbital order	22		
C. Interaction effects	23		
1. RPA approach	23		
2. Spin-fermion model	24		
3. RG analysis	24		
4. RG for the 4-pocket model without $d_{xy}$ orbital contribution	25		

## I. INTRODUCTION

The discovery of a rich family of iron-based superconductors (FeSC) with a variety of different chemical compositions [1, 2], such as LaFeAsO (1111 material), BaFe<sub>2</sub>As<sub>2</sub> (122 material), NaFeAs (111 material), and FeSe (11 material), opened a new route to study high-temperature superconductivity. Similarly to high- $T_c$  cuprates, which are made of coupled CuO<sub>2</sub> layers, FeSC are also layered systems made of coupled FeAs layers. In both cases, the Cu and Fe atoms form a simple square lattice.

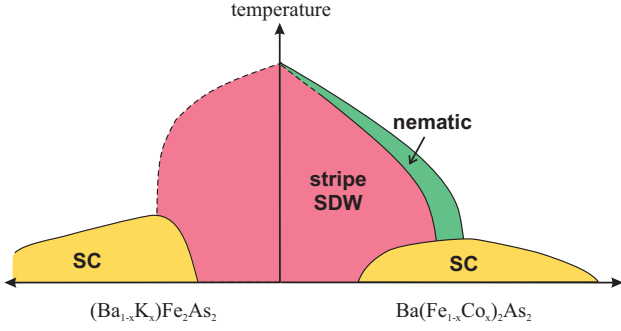


Figure 1. Schematic phase diagram of electron-doped (Co-doped) and hole-doped (K-doped)  $\text{BaFe}_2\text{As}_2$ , displaying stripe spin-density wave (SDW) order, nematic order, and superconductivity (SC).

The phase diagrams of FeSC are also quite similar to those of the cuprates. Although details of the phase diagrams vary between different families of FeSC, most materials display the key features shown in Fig. 1 (for reviews, see [3–6]). Specifically, the parent compounds of most (but not all) FeSC are magnetically ordered metals. In most cases, the magnetic order is of a stripe type – i.e. spins are ferromagnetically aligned in one direction in the Fe plane and antiferromagnetically aligned in the other. This is usually known as the  $(0, \pi)/(\pi, 0)$  spin-density wave (SDW) state. Upon hole or electron doping, or upon substitution of one pnictide atom by another, magnetic order goes away and a dome of superconductivity emerges. In addition, there is a region on the phase diagram where the system displays nematic order, in which the  $C_4$  lattice rotation symmetry is spontaneously broken ( $C_4$  is the point group symmetry associated with a square, whereas  $C_2$  is the point group symmetry associated with a rectangle). The nematic order naturally coexists with the stripe magnetic order and in some systems also coexists with superconductivity [7].

Despite the similarities in their phase diagrams, there are important differences between the cuprates and FeSC. The most pronounced difference is that the low-energy electronic states of the cuprates arise from  $\text{Cu}^{2+}$ , which is in a  $3d^9$  electronic configuration, while in the FeSC the low-energy states arise from  $\text{Fe}^{2+}$ , which is in a  $3d^6$  configuration. One immediate consequence of this difference is that parent compounds of the cuprates are Mott insulators, while parent compounds of FeSC are metals. The relevance of metallicity of FeSC has been discussed in earlier reviews and we will not dwell on this [8–10]. In this review we focus on another immediate consequence of the difference between  $3d^9$  and  $3d^6$  electronic configurations, namely the fact that the  $3d^6$  configuration involves five  $3d$  orbitals –  $d_{xz}$ ,  $d_{yz}$ ,  $d_{xy}$ ,  $d_{x^2-y^2}$ , and  $d_{3z^2-r^2}$ , while  $3d^9$  configuration contains a single  $d_{x^2-y^2}$  orbital. This brings important consequences for microscopic models constructed to describe  $3d^9$  and  $3d^6$  systems.

In a free space, the five  $3d$  orbitals are all degenerate. In a crystalline environment the degeneracy is lifted, and

the energy levels are split into two subsets,  $t_{2g}$  and  $e_g$ , with three and two orbitals, respectively:  $d_{xz}$ ,  $d_{yz}$ , and  $d_{xy}$  for  $t_{2g}$  and  $d_{x^2-y^2}$  and  $d_{3z^2-r^2}$  for  $e_g$  (the subscript  $g$  implies that the states are symmetric under inversion). In some multi-orbital systems, such as the manganites ( $3d^5$ ) and the cobaltates ( $3d^7$ ), the crystal-field splitting is large, and this allows one to focus on only one subset. In FeSC the situation is more subtle because the As/Se positions alternate between the ones above and below the center of the Fe plaquettes, as shown in Fig. 2. Because of such puckering of the As/Se atoms, the crystalline environment experienced by Fe atoms is somewhat in between a tetrahedral one, in which the energy of the  $t_{2g}$  orbitals is higher than that of the  $e_g$  orbitals, and a tetragonal one, in which the energy of the  $t_{2g}$  orbitals is lower (see Fig. 2 and Ref. [11]). As a result, the crystal splitting between the orbitals is weakened in FeSC and, consequently, all five  $d$ -orbitals must be kept in the kinetic energy Hamiltonian:

$$\mathcal{H}_0 = \sum_{ij, \mu\nu} \sum_{\sigma} t_{\mu i, \nu j} d_{\mu, i\sigma}^\dagger d_{\nu, j\sigma} \quad (1)$$

Here  $d_{\mu, i\sigma}^\dagger$  creates an electron at site  $i$  and orbital  $\mu$  ( $\mu = 1, \dots, 5$ ) with spin  $\sigma$ , and  $t_{\mu i, \nu j}$  are hopping amplitudes. The diagonal terms describe the dispersions of electrons from separate orbitals, whereas the non-diagonal terms account for the hopping from one orbital to the other. The latter give rise to hybridization of the eigenstates from different orbitals. The hopping parameters  $t_{\mu i, \nu j}$  can either be directly fit to the band dispersions obtained in first-principle calculations [12, 13] or calculated in a perturbative Slater-Koster approach as functions of the distance between Fe and As [14]. In the former case, one usually needs several-neighbors hopping parameters to achieve a good fit, which makes the fitting procedure itself involved. In the latter, one has to rely on first principle calculations to get several parameters which are inputs for the Slater-Koster approach.

Both diagonal and non-diagonal  $t_{\mu i, \nu j}$  between different sites  $i$  and  $j$  result from either a direct hopping from one Fe site to the other, or indirect hopping via As/Se. Because of the two non-equivalent position of the As/Se atoms with respect to the Fe plane, the fundamental period in the Fe plane is the distance between next-nearest-neighbor Fe atoms, i.e. the crystallographic unit cell must contain two Fe atoms. Thus, to respect all symmetries of the lattice, the kinetic energy must include ten Fe orbitals [15, 16].

Because  $\mathcal{H}_0$  is not diagonal in the orbital basis, one invariably needs to diagonalize  $10 \times 10$  matrices in the orbital space to obtain quasiparticle dispersions. The diagonalization yields a 10-band non-interacting Hamiltonian

$$\mathcal{H}_0 = \sum_{m=1}^N \varepsilon_m(\mathbf{k}) c_{m, \mathbf{k}\sigma}^\dagger c_{m, \mathbf{k}\sigma} \quad (2)$$

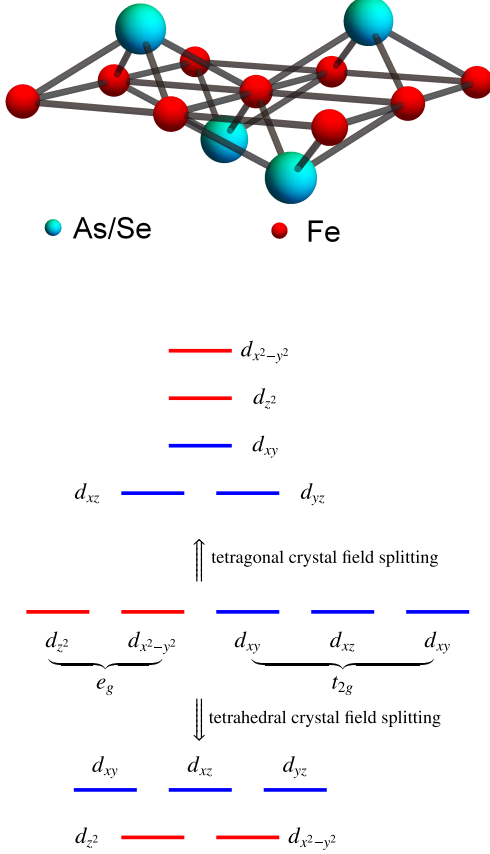


Figure 2. (upper panel) Schematic crystal structure of an FeAs or FeSe plane, displaying the puckering of the As/Se atoms above and below the square Fe plane. (lower panel) The crystal field splittings of the  $3d$   $e_g$  (red) and  $t_{2g}$  (blue) orbitals from a tetragonal and a tetrahedral environment (see also Ref. [11]).

where  $c_{m,\mathbf{k}\sigma}^\dagger$  creates an electron in band  $m$  with momentum  $\mathbf{k}$  and spin  $\sigma$ . The band and orbital operators are related by the matrix elements associated with the diagonalization of  $\mathcal{H}_0$ ,  $a_{m\mu}(\mathbf{k}) \equiv \langle m\mathbf{k} | \mu \rangle$

$$c_{m,\mathbf{k}\sigma} = \sum_{\mu} a_{m\mu}(\mathbf{k}) d_{\mu,\mathbf{k}\sigma} \quad (3)$$

Although diagonalizing  $10 \times 10$  matrices is numerically straightforward, it becomes difficult to gain qualitative understanding and insights into the problem once interactions are included, even if the Coulomb interaction is heavily screened and can be approximated as a local one. In the cuprates, the interaction between electrons from a single orbital is fully described by the Hubbard repulsion  $U$ . In FeSC, there are at least four onsite interaction

terms involving  $3d$  electrons [12, 17, 18]:

$$\begin{aligned} \mathcal{H}_{\text{int}} = & U \sum_{i,\mu} n_{\mu,i\uparrow} n_{\mu,i\downarrow} + J \sum_{i,\mu < \nu} \sum_{\sigma,\sigma'} d_{\mu,i\sigma}^\dagger d_{\nu,i\sigma'}^\dagger d_{\mu,i\sigma'} d_{\nu,i\sigma} \\ & + U' \sum_{i,\mu < \nu} n_{\mu,i} n_{\nu,i} + J' \sum_{i\mu \neq \nu} d_{\mu,i\uparrow}^\dagger d_{\mu,i\downarrow}^\dagger d_{\nu,i\downarrow} d_{\nu,i\uparrow} \quad (4) \end{aligned}$$

Here  $U$  is the usual Hubbard repulsion between electrons on the same orbitals,  $U'$  is the onsite repulsion between electrons on different orbitals,  $J$  is the Hund's exchange that tends to align spins at different orbitals, and  $J'$  is another exchange term, often called the pair-hopping term. The presence of four different interactions enlarges the parameter space and makes calculations much more involved.

Several works attempted to simplify the  $U, U', J, J'$  model by invoking rotational invariance to argue that the interaction must be expressed in terms of the squares of the total number and the total spin of  $3d$ -electrons on a given site,  $\sum_{\mu,\alpha} d_{\mu,i\alpha}^\dagger d_{\mu,i\alpha}$  and  $\sum_{\mu,\alpha} d_{\mu,i\alpha}^\dagger \vec{\sigma}_{\alpha\beta} d_{\mu,i\beta}$ , respectively. This would reduce the number of independent interaction terms in the Hamiltonian to two via the relationships  $U' = U - 2J$  and  $J' = J$ . However, this would be true if As/Se states were irrelevant. This is not the case in FeSC because the hopping from one Fe site to the other partly goes through As/Se atoms. These As/Se states must then be included also in the interaction term. They are high-energy states (around 5 eV away from the Fermi level) and one can integrate them out for studies of the physics at much smaller scales, related to magnetism, superconductivity, and electronic nematic order. But by integrating out As/Se states, one breaks spin rotational invariance of the  $3d$  orbitals, and, as a result, breaks the relations  $U' = U - 2J$  and  $J' = J$ . Besides, by integrating high-energy parts of the spectra of the Fe  $3d$  orbitals, one necessarily generates interactions between neighboring Fe sites. This additionally breaks the relations between  $U'$  and  $U - 2J$  and between  $J'$  and  $J$ .

All these complications raise the important question of whether one can construct a sensible and simpler minimal microscopic model to capture the low-energy physics of the FeSC without the need for  $10 \times 10$  (or  $5 \times 5$ ) matrices and a large number of interaction terms. In this review, we discuss microscopic models that have been proposed and solved to understand distinct aspects of the FeSC. We will highlight the advantages of these models and their drawbacks.

In Section II we discuss approximate orbital models with a smaller number of  $3d$  Fe orbitals and review the computations done solely in terms of orbital operators. In Section III we discuss the models which use the experimental knowledge of the location of the Fermi surfaces as an input and analyze the effects of the interactions in the band basis, without referring to the orbital content of the excitations. In Section IV we discuss works in which the analysis of the instabilities is done in the band basis, but the interactions in all channels are constructed from the orbital basis and retain the full memory about the orbital

content of the low-energy states. We review RPA studies of magnetically-mediated pairing interaction and discuss recent works on the interplay between superconductivity, magnetism, and a spontaneous orbital order. We discuss the minimal model for the analysis of the competing orders and show the results of the renormalization group (RG) study of such a model.

The models in Sections II-IV are constructed in the 1-Fe unit cell and as such neglect the Fe-As/Se hybridization. In Section V we analyze the consequences of this approximation and discuss extensions of these models to the 2-Fe unit cell. We first show how the dispersions change if we just convert from 1-Fe to 2-Fe basis, then briefly discuss the effect of additional terms with momentum transfer  $(\pi, \pi)$  in  $\mathcal{H}_0$  and  $\mathcal{H}_{\text{int}}$ , which originate from the actual non-equivalence of neighboring Fe cells in 1-Fe basis, and then discuss the role of spin-orbit coupling. We present concluding remarks in Section VI.

The main points of this comparative analysis are the following:

- Approximate orbital models (hereafter called orbital-basis models) with two and three orbitals are attractively simple and offer interesting insights into the orbital physics of FeSCs. However, because the analysis in the orbital basis does not rely on the presence of the Fermi surface, it necessarily involves excitations with all momenta. It turns out that the three-band model correctly captures the low-energy sector of the full five-orbital model, but *cannot* correctly describe how the excitations evolve from one low-energy sector to the other. The minimum model which correctly describes both the low-energy sectors and the evolution of excitations between them must involve at least four orbitals.
- Multi-band models (hereafter called band-basis models) with phenomenologically-derived interactions between low-energy electronic states offer an appealing and simple framework to study superconductivity and magnetism, the interplay between the two, and vestigial Ising-nematic order caused by magnetic fluctuations. They ignore, however, the orbital content of the low-energy states, and as such they are generally blind to phenomena involving orbital physics.
- The models which operate in the band basis but use the full knowledge of the orbital content of the low-energy excitations (hereafter called orbital-projected band models) seem to be the most promising ones. These models include three orbitals ( $d_{xz}$ ,  $d_{yz}$ , and  $d_{xy}$ ), from which the low-energy excitations are constructed, and the interactions between low-energy states contain angle-dependent prefactors that reflect the orbital composition of the Fermi surfaces. The full model of this kind still contains too many coupling constants, but most of the physics is captured already

by simplified models with a smaller number of couplings.

- The phenomena associated with the sizable spin-orbit coupling of the FeSC can only be captured in the 2-Fe unit cell. The orbital-projected band models can naturally be extended to this case without the need to double the number of terms in the kinetic part of the Hamiltonian.

Throughout this review we assume that none of the low-energy electronic states is localized by interactions. We believe this is a sensible starting point, as most of the FeSC are metals, with a pronounced Drude peak in the AC conductivity (see, for instance, [19]). This does not imply that we consider weak coupling. Rather, in the analysis of band models in Sections III and IV we assume that the renormalizations by high-energy electronic states change the “band masses” and the offset energies of low-energy excitations, and modify the residues  $Z_i$  of low-energy states, while keeping these excitations coherent. The renormalized dispersion parameters can be extracted from the experimental data on the electronic dispersion, and the residues  $Z_i$  can be incorporated into the interactions. This indeed changes the values of the bare interaction terms, but we will see that the interactions flow under RG (renormalization group) towards universal values, independent on the bare ones. The actual (measured) electronic excitations do indeed have a finite lifetime  $1/\tau$ . Our assumptions imply that the dominant contribution to  $1/\tau$  for each low-energy fermion comes from the processes involving only low-energy states, i.e.,  $1/\tau$  is not an input but rather has to be determined within the low-energy analysis.

Alternative low-energy models have been proposed based on Heisenberg or Kugel-Khomskii type Hamiltonians [20–23], which effectively assume that the system is an insulator. The argument here is that, while FeSC do display the metallic behavior at low temperatures, some orbitals may be either localized or near localization [24–27]. Because of space constraints, we will not discuss these models further in the present review. We also will not discuss here an interesting concept that the Hund’s interaction  $J$  plays an important role in promoting bad metallic (but still metallic) behavior up to large values of the Hubbard  $U$  [28–34]. As we said, in the next three sections we discuss the electronic structure and the interplay between superconductivity, magnetism, and nematic order within the 1-Fe unit cell, i.e., we restrict ourselves to the five-orbital model ( $N = 5$ ). Physically, this assumption implies that we neglect terms in the Hamiltonian with momentum transfer  $(\pi, \pi)$  and also neglect the spin-orbit interaction.

## II. ORBITAL-BASIS MODELS

In this section we focus on approximate models defined and analyzed in the orbital basis. We first discuss

the non-interacting part of the Hamiltonian  $\mathcal{H}_0$ , and investigate whether it is possible to restrict the number of orbitals to 2 or 3 and keep the symmetry constraints intact. We then briefly review the studies of interactions in the orbital basis.

### A. Non-interacting Hamiltonian

We discuss the full 5-orbital model in subsection II A 1 and discuss the models that restrict the number of orbitals to 2 and 3 in Subsections II A 2 and II A 3, respectively. We remind that the goal to analyze models with smaller number of orbitals is to simplify the analysis in order to gain qualitative understanding and insights into the issue of competing instabilities, once interactions are included.

#### 1. Five-orbital model

The non-interacting part of the Hamiltonian of the five-orbital model is given by  $\mathcal{H}_0$  in Eq. (1). Taking its Fourier transform gives:

$$\mathcal{H}_0 = \sum_{\mu\nu} [\epsilon_{\mu\nu}(\mathbf{k}) - \bar{\mu}\delta_{\mu\nu}] d_{\mu,\mathbf{k}\sigma}^\dagger d_{\nu,\mathbf{k}\sigma} \quad (5)$$

where  $\bar{\mu}$  is the chemical potential. The explicit expressions for the tight-binding dispersions  $\epsilon_{\mu\nu}(\mathbf{k})$  with hopping up to fourth-neighbors are given in Appendix A, together with the values of the tight-binding parameters of Ref. [12] (see Table I).

In Fig. 3, we show the band dispersion and the Fermi surfaces corresponding to the parameters for LaFeAsO from Ref. [18]. The Fermi surfaces are colored according to which orbital gives the largest spectral weight, the latter being defined by the matrix element  $|a_{m\mu}(\mathbf{k})|^2$  in Eq. (3). Along the Fermi surface, we have  $\mathbf{k} = \mathbf{k}_F$  and  $|a_{m\mu}(\mathbf{k})| = |a_{m\mu}(\theta)|$ , where  $\theta$  is the angle with respect to  $k_x$ . The Fermi surface is composed of small pockets centered at high-symmetry points of the Brillouin zone (BZ), namely  $\Gamma = (0, 0)$ ,  $X = (\pi, 0)$ ,  $Y = (0, \pi)$ , and  $M = (\pi, \pi)$  (all momenta hereafter are given in units of  $1/a$ , where  $a$  is the length of the corresponding unit cell).

There are two hole-like bands that cross the Fermi level near the  $\Gamma$  point, giving rise to two hole pockets  $h_1$  and  $h_2$ . As shown in Fig. 4, the angle-dependent spectral weights  $|a_{h_i\mu}(\theta)|^2$  on these Fermi pockets mostly come from the  $d_{xz}$  and  $d_{yz}$  orbitals. Similarly, two electron-like bands cross the Fermi level near the  $X$  and  $Y$  points, giving rise to two electron pockets  $e_X$  and  $e_Y$ . The spectral weight on the pocket  $e_X$  is dominated by the  $d_{yz}$  and  $d_{xy}$  orbitals, whereas the spectral weight on the pocket  $e_Y$  is dominated by  $d_{xz}$  and  $d_{xy}$ . Tetragonal symmetry enforces the following conditions, which can be readily observed in the figure:

$$\begin{aligned} |a_{e_X d_{yz}}(\theta)|^2 &= |a_{e_Y d_{xz}}(\theta + \pi/2)|^2 \\ |a_{e_X d_{xy}}(\theta)|^2 &= |a_{e_Y d_{xy}}(\theta + \pi/2)|^2 \end{aligned} \quad (6)$$

An additional hole-pocket  $h_M$  crosses the Fermi level near the  $M$  point. Its spectral weight is almost entirely due to the  $d_{xy}$  orbital, as shown in the figure. Inspection of the band dispersion reveals that the top of this hole-like band is very close to the Fermi level, and that small changes in the crystal lattice parameters or in the chemical potential may make it sink below the Fermi level, effectively erasing the corresponding Fermi pocket [35]. Thus, the presence of this third hole pocket is rather material dependent. It is absent in NaFeAs and FeSe, but present in BaFe<sub>2</sub>As<sub>2</sub> and LiFeAs. Note that, while all hole pockets must have  $C_4$ -symmetric shapes, the electron pockets have  $C_2$  symmetric shapes, which are related to each other by a  $\pi/2$  rotation.

This generic Fermi surface can be tuned by changes in the chemical potential, which is achieved via electron doping (such as Co-doped NaFeAs) or hole doping (such as Na-doped BaFe<sub>2</sub>As<sub>2</sub>), see Refs. [36, 37]. For sufficiently electron-doped systems, such as K<sub>1-y</sub>Fe<sub>2-x</sub>Se<sub>2</sub> and electrostatically gated FeSe, the hole pockets disappear and only electron pockets remain. Analogously, for systems with strong hole doping, such as K-doped BaFe<sub>2</sub>As<sub>2</sub>, the electron pockets disappear and only hole pockets are left. Isovalent substitution, achieved e.g. via gradual replacement of As by P or Fe by Ru in 122 systems, alters the Fermi surface due to the changes in the crystal lattice parameters (more prominently the Fe-As distance) and also by the disorder potential which isovalent substitution introduces to the system.

#### 2. Two-orbital model

It is clear from Fig. 3 that not all five orbitals contribute equally to the low-energy states near the Fermi energy. In fact, the Fermi surface states are made almost exclusively from  $d_{xz}$ ,  $d_{yz}$ , and  $d_{xy}$  orbitals (see Figs. 3 and 4). One can then conjecture that at least some of the physics of FeSC can be understood within a simplified model with only this subset of orbitals. Raghu *et al.* assumed, on top of this, that the hopping via the  $d_{xy}$  orbital could be integrated out and absorbed into next-nearest-neighbor hopping terms involving  $d_{xz}$  and  $d_{yz}$  orbitals [38]. They proposed the effective two-orbital model:

$$\mathcal{H}_0 = \sum_{\mu\nu=xz,yz} [\epsilon_{\mu\nu}(\mathbf{k}) - \bar{\mu}\delta_{\mu\nu}] d_{\mu,\mathbf{k}\sigma}^\dagger d_{\nu,\mathbf{k}\sigma} \quad (7)$$

with tight-binding parameters (see Table II in Appendix A):

$$\begin{aligned} \epsilon_{xx,xz}(\mathbf{k}) &= -2t_1 \cos k_x - 2t_2 \cos k_y - 4t_3 \cos k_x \cos k_y \\ \epsilon_{yz,yz}(\mathbf{k}) &= -2t_2 \cos k_x - 2t_1 \cos k_y - 4t_3 \cos k_x \cos k_y \\ \epsilon_{xz,yz}(\mathbf{k}) &= \epsilon_{yz,xz}(\mathbf{k}) = -4t_4 \sin k_x \sin k_y \end{aligned} \quad (8)$$

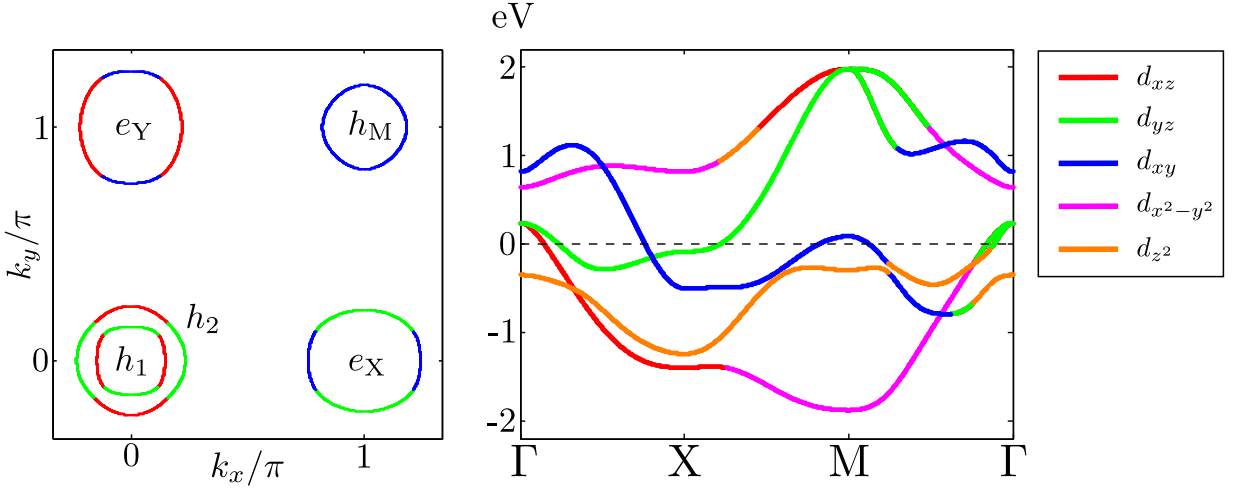


Figure 3. Tight-binding dispersion of Ref. [18] and the resulting Fermi surface in the 1-Fe BZ. The bands are colored according to the orbital that contributes the largest spectral weight.

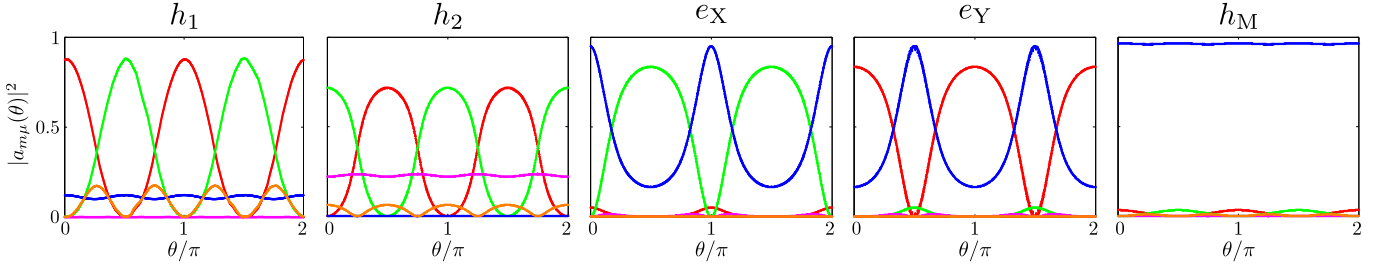


Figure 4. Orbital spectral weight  $|a_{m\mu}(\theta)|^2$  of each Fermi surface as function of the angle  $\theta$  measured relative to the  $k_x$  axis. The color code is the same as in Fig. 3.

Fig. 5 shows the corresponding band dispersion and the Fermi surfaces. In contrast to the 5-orbital model, one of the two  $d_{xz}/d_{yz}$  hole pockets is centered at the  $M$  point instead of the  $\Gamma$  point. Such an artifact of the 2-orbital model was not originally considered to be problematic because in the true crystallographic unit cell, containing two Fe atoms, the  $M$  point is folded onto the  $\Gamma$  point, restoring the existence of two hole pockets at the center of the BZ.

The simplicity of the 2-orbital model, which can be conveniently written in terms of Pauli matrices in the orbital space, led to many studies about the electronic properties and instabilities of this model [40–48]. Despite its appeal, there are issues with this model that go beyond the incorrect position of one of the hole pockets. Most importantly, the 2-orbital model does not respect all the symmetries of the FeAs plane – in particular, the symmetry related to a translation by  $(\frac{1}{2}, \frac{1}{2})$  followed by a mirror reflection with respect to the  $xy$  plane. As explained in Ref. [49], the two hole pockets formed by the  $d_{xz}$  and  $d_{yz}$  orbitals must be odd under this symmetry, whereas in the 2-orbital model only one of the pockets is odd. The absence of the  $d_{xy}$  orbital is also a potential issue, as it has been argued to play an important role in certain FeSC [29, 50, 51].

### 3. Three-orbital model

A possible way to remedy the issues of the 2-orbital model is to include the third orbital that contributes significantly to the spectral weight of the low-energy states, namely the  $d_{xy}$  orbital. The corresponding 3-orbital model is described by [52, 53]

$$\mathcal{H}_0 = \sum_{\mu\nu=xz,yz,xy} [\epsilon_{\mu\nu}(\mathbf{k}) - \bar{\mu}\delta_{\mu\nu}] d_{\mu,\mathbf{k}\sigma}^\dagger d_{\nu,\mathbf{k}\sigma} \quad (9)$$

with the tight-binding dispersions (see Table III in Appendix A):

$$\begin{aligned} \epsilon_{xz,xz}(\mathbf{k}) &= -2t_1 \cos k_x - 2t_2 \cos k_y - 4t_3 \cos k_x \cos k_y \\ \epsilon_{yz,yz}(\mathbf{k}) &= -2t_2 \cos k_x - 2t_1 \cos k_y - 4t_3 \cos k_x \cos k_y \\ \epsilon_{xy,xy}(\mathbf{k}) &= -2t_5 (\cos k_x + \cos k_y) - 4t_6 \cos k_x \cos k_y + \Delta_{\text{CF}} \end{aligned} \quad (10)$$

as well as:

$$\begin{aligned} \epsilon_{xz,yz}(\mathbf{k}) &= -4t_4 \sin k_x \sin k_y \\ \epsilon_{xz,xy}(\mathbf{k}) &= -2it_7 \sin k_x - 4it_8 \sin k_x \cos k_y \\ \epsilon_{yz,xy}(\mathbf{k}) &= -2it_7 \sin k_y - 4it_8 \sin k_y \cos k_x \end{aligned} \quad (11)$$

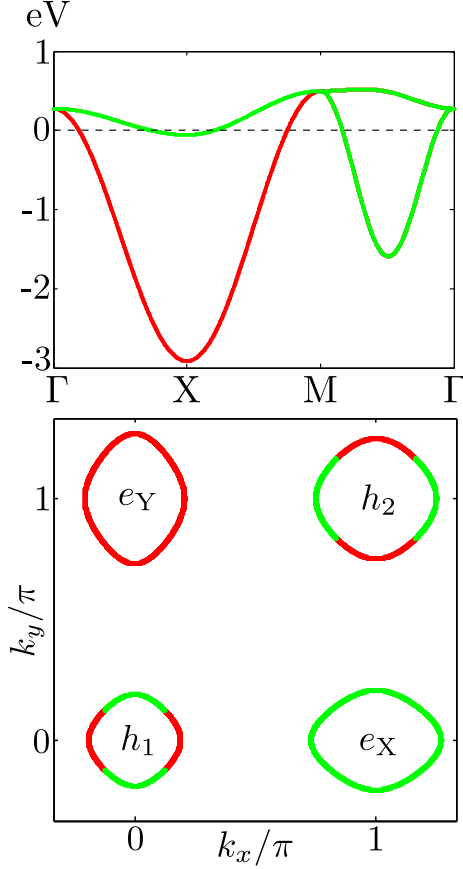


Figure 5. Two-orbital model of Ref. [38]: band dispersion (upper panel) and the Fermi surface (lower panel). In the latter, the Fermi surface is colored according to the orbital that contributes the largest spectral weight (red for  $d_{xz}$  and green for  $d_{yz}$ ). The tight-binding parameters used here are those from Ref. [39].

where  $\Delta_{\text{CF}}$  is the crystal field splitting. Note that  $\epsilon_{\mu\nu}(\mathbf{k}) = \epsilon_{\nu\mu}^*(\mathbf{k})$ . Although more complex than the 2-orbital model, the 3-orbital model is still much simpler than the 5-orbital one, and may be conveniently expressed in terms of the eight  $3 \times 3$  Gell-Mann matrices.

The main issue with restricting the orbitals to the  $t_{2g}$  subspace (i.e.  $d_{xz}$ ,  $d_{yz}$ , and  $d_{xy}$ ) is the presence of an additional, spurious Fermi surface pocket due to the lack of hybridization with the  $e_g$  orbitals ( $d_{x^2-y^2}$  and  $d_{z^2}$ ) [49, 52]. To illustrate this point, we consider again the 5-orbital model of Fig. 3 but turn off the hybridization between the  $t_{2g}$  and  $e_g$  orbitals. The result, shown in Fig. 6, reveals an additional hole-like pocket near the  $M$  point due to the fact that one of the (hybridized)  $e_g$  bands and the  $d_{xz}/d_{yz}$ -dominated band cross the Fermi level. A comparison with Fig. 3 shows that it is the hybridization between this  $e_g$  band and the  $d_{xz}/d_{yz}$  band that prevents both bands from crossing the Fermi level. This clearly indicates that all five orbitals are necessary to obtain the correct geometry of the Fermi pockets, despite the fact that the low-energy states in the correct geometry are

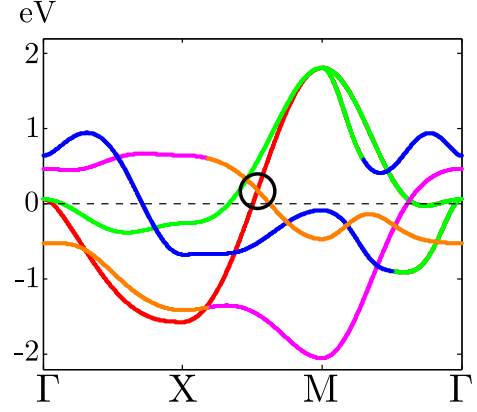


Figure 6. The five-orbital model of Fig. 3 with the hybridization between the  $t_{2g}$  orbitals ( $d_{xz}$ ,  $d_{yz}$ ,  $d_{xy}$ ) and the  $e_g$  orbitals ( $d_{x^2-y^2}$ ,  $d_{z^2}$ ) turned off. The orbital color code is the same as Fig. 3. The absence of hybridization leads to a spurious crossing of one of the  $t_{2g}$  bands at the Fermi level (highlighted area).

composed only from  $t_{2g}$  orbitals.

This generic difficulty with the 3-orbital model can be overcome by changing the tight-binding parameters in Eq. 5 to alter the ordering of the bands at the  $M$  point. In particular, one can move the  $d_{xz}/d_{yz}$  bands below the Fermi level at the  $M$  point, while keeping the  $d_{xy}$  band at  $M$  above the Fermi level [53]. As a result, the spurious Fermi pocket is removed, as shown in Fig. 7. While this alternative is appealing, it cannot capture the  $d_{xy}$  hole pocket at the  $M$  point without reintroducing the spurious  $d_{xz}/d_{yz}$  pocket around  $M$ .

## B. Order parameters

The order parameters whose condensation leads to density-waves, superconductivity, and orbital order, are bilinear combinations of fermions in the particle-hole and particle-particle channels, either with zero transferred momentum (or total momentum, in the case of superconductivity), or with a finite momentum. In general, each order parameter is a  $5 \times 5$  matrix in the orbital space [12, 53–55]. The CDW and SDW order parameters are

$$\begin{aligned}\Delta_{\text{CDW},j}^{\mu\nu}(\mathbf{k}) &= d_{\mu,\mathbf{k}\alpha}^\dagger \delta_{\alpha\beta} d_{\nu,\mathbf{k}+\mathbf{Q}_j\beta} + h.c. \\ \Delta_{\text{iCDW},j}^{\mu\nu}(\mathbf{k}) &= i d_{\mu,\mathbf{k}\alpha}^\dagger \delta_{\alpha\beta} d_{\nu,\mathbf{k}+\mathbf{Q}_j\beta} + h.c. \\ \Delta_{\text{SDW},j}^{\mu\nu}(\mathbf{k}) &= d_{\mu,\mathbf{k}\alpha}^\dagger \sigma_{\alpha\beta} d_{\nu,\mathbf{k}+\mathbf{Q}_j\beta} + h.c. \\ \Delta_{\text{iSDW},j}^{\mu\nu}(\mathbf{k}) &= i d_{\mu,\mathbf{k}\alpha}^\dagger \sigma_{\alpha\beta} d_{\nu,\mathbf{k}+\mathbf{Q}_j\beta} + h.c.\end{aligned}\quad (12)$$

where  $\mu, \nu$  label the orbitals and  $j = X, Y$ , with  $\mathbf{Q}_X = (\pi, 0)$  and  $\mathbf{Q}_Y = (0, \pi)$ . SC order parameters for spin-singlet pairing with zero center-of-mass pair momentum are defined for a given  $\mathbf{k}$  according to

$$\Delta_{\text{SC}}^{\mu\nu}(\mathbf{k}) = d_{\mu,\mathbf{k}\alpha}^\dagger \left( i \sigma_{\alpha\beta}^y \right) d_{\nu,-\mathbf{k}\beta} f_{\text{SC}}(\mathbf{k}) + h.c. \quad (13)$$

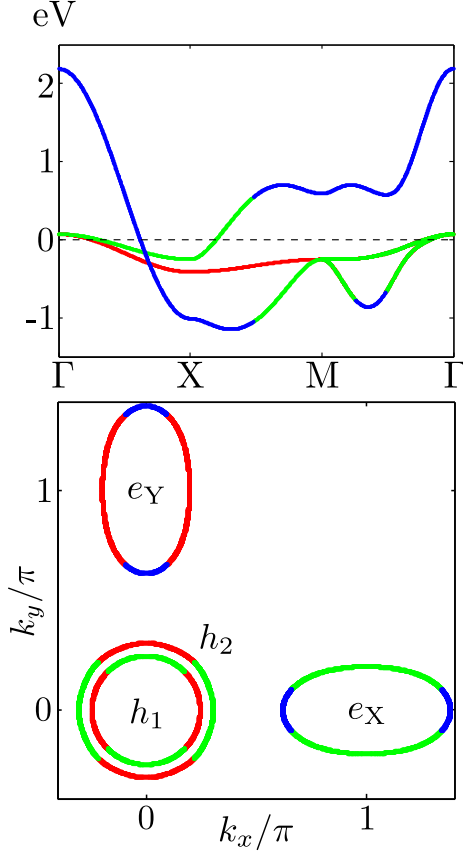


Figure 7. Three-orbital model of Ref. [53]: band dispersion (upper panel) and Fermi surface (lower panel). In the latter, the Fermi surface is colored according to the orbital that contributes the largest spectral weight (red for  $d_{xz}$ , blue for  $d_{xy}$ , and green for  $d_{yz}$ ).

where  $f_{\text{SC}}(\mathbf{k})$  is an even function of  $\mathbf{k}$  that has the full lattice symmetry, but can change sign between, e.g.,  $\mathbf{k} = 0$  and  $\mathbf{k} = (0, \pi)/(\pi, 0)$ . Out of these order parameters one can construct the combinations that transform as  $A_{1g}$ ,  $B_{1g}$ ,  $B_{2g}$ , and  $A_{2g}$  irreducible representations of the  $D_{4h}$  group. For instance,  $\Delta_{\text{SC}}^{xz,xz} + \Delta_{\text{SC}}^{yz,yz}$  belongs to the  $A_{1g}$  representation, while  $\Delta_{\text{SC}}^{xz,xz} - \Delta_{\text{SC}}^{yz,yz}$  belongs to the  $B_{1g}$  representation. These two are often called  $s$ -wave and  $d$ -wave, by analogy with isotropic systems. Alternatively, one can classify linear combinations of the order parameters in the orbital basis as orbitally in-phase and orbitally anti-phase [56, 57]

The eigenfunctions from each representation can be further classified into sub-classes depending on how  $f_{\text{SC}}(\mathbf{k})$  evolves between the high-symmetry points  $(0, 0)$ ,  $(0, \pi)/(\pi, 0)$ , and  $(\pi, \pi)$ . These symmetry points coincide with the center of hole and electron pockets, but their presence is not explicitly emphasized in the analysis in the orbital basis. The two most known sub-classes, called “plus-plus” and “plus-minus” [17, 58–60], correspond to  $f_{\text{SC}}(0) = f_{\text{SC}}(0, \pi) = f_{\text{SC}}(\pi, 0) = f_{\text{SC}}(\pi, \pi)$  (plus-plus) and  $f_{\text{SC}}(0) = f_{\text{SC}}(\pi, \pi) = -f_{\text{SC}}(0, \pi) = -f_{\text{SC}}(\pi, 0)$  (plus-minus). In the  $A_{1g}$  ( $B_{1g}$ ) channels, these subclasses

are called  $s^{++}$  ( $d^{++}$ ) and  $s^{+-}$  ( $d^{+-}$ ), respectively.

Orbital order is an instability in the charge channel. It gives rise to a CDW if the order parameter has a finite momentum, in which case the corresponding order parameter is a particular combination of the terms from Eq. 12. Orbital order with zero momentum emerges as a Pomeranchuk instability, and the corresponding order parameter is given by

$$\Delta_{\text{POM}}^{\mu\nu}(\mathbf{k}) = d_{\mu, \mathbf{k}\alpha}^\dagger \delta_{\alpha\beta} d_{\nu, \mathbf{k}\beta} f_{\text{POM}}(\mathbf{k}) \quad (14)$$

Similarly to superconductivity, one can form linear combinations of  $\Delta_{\text{POM}}^{\mu\nu}(k)$  that transform as the  $A_{1g}$ ,  $B_{1g}$ ,  $B_{2g}$ , and  $A_{2g}$  irreducible representations of the  $D_{4h}$  space group. In particular,  $\Delta^{xz,xz} + \Delta^{yz,yz}$  belongs to the  $A_{1g}$  representation,  $\Delta^{xz,xz} - \Delta^{yz,yz}$  belongs to the  $B_{1g}$  representation,  $\Delta^{xz,yz} + \Delta^{yz,xz}$  belongs to the  $B_{2g}$  representation, and  $\Delta^{xz,yz} - \Delta^{yz,xz}$  belongs to the  $A_{2g}$  representation. In the literature, ferro-orbital order [22, 61–65] is usually associated with the  $B_{1g}$  order parameter  $\Delta^{xz,xz} - \Delta^{yz,yz}$ . Again, each representation can be further classified into sub-classes, depending on the symmetry properties of  $f_{\text{POM}}(\mathbf{k})$ . The notations “plus-plus” and “plus-minus” apply to the cases  $f_{\text{POM}}(0) = f_{\text{POM}}(0, \pi) = f_{\text{POM}}(\pi, 0)$  and  $f_{\text{POM}}(0) = -f_{\text{POM}}(0, \pi) = -f_{\text{POM}}(\pi, 0)$ , respectively. In real space, plus-plus  $B_{1g}$  (i.e.  $d$ -wave) order is on-site ferro-orbital order, while plus-minus order is a bond order. An  $s$ -wave charge order with zero momentum ( $s^{++}$  or  $s^{+-}$ ) does not break any symmetry and therefore does not represent a true order parameter since the mean values of  $\Delta^{xz,xz} + \Delta^{yz,yz}$  are non-zero at any temperature. Fluctuations in the  $s^{++}$  Pomeranchuk channel are frozen due to the constraint of a constant occupation number (Luttinger’s theorem). Fluctuations in the  $s^{+-}$  Pomeranchuk channel, however, are not frozen, and the corresponding susceptibility can sharply increase around a certain temperature, mimicking the development of a true order parameter. The  $d$ -wave Pomeranchuk order parameter, on the other hand, can develop spontaneously, and its condensation breaks the tetragonal symmetry of the system (i.e. the  $x$  and  $y$  spatial directions become inequivalent), but preserves the translational symmetry.

### C. Interaction effects

As we discussed above, the main goal of the studies of the effects of interactions in the orbital basis is to understand the ordered states which we just introduced, namely magnetism, superconductivity, and orbital order, without focusing *a priori* on the low-energy states near the Fermi pockets. Another goal of these studies is to find how strong the effects leading to electron localization are, and how these effects differentiate between distinct orbitals.

Nearly all studies of the interaction effects in FeSC within the orbital basis depart from the onsite interaction

Hamiltonian from Eq. (4), with inter-orbital and intra-orbital terms, and use mean-field (RPA) self-consistent analysis. For magnetism, such an analysis revealed magnetic instabilities towards a SDW order with momenta  $\mathbf{Q}_X$  or  $\mathbf{Q}_Y$ , as well as a subleading instability towards a Neel order with  $\mathbf{Q}_M = (\pi, \pi)$  [12, 40, 54, 66–69]. The selection of magnetic order – i.e. whether both  $\mathbf{Q}_X$  and  $\mathbf{Q}_Y$  are condensed in a double- $\mathbf{Q}$  tetragonal state, or a single- $\mathbf{Q}$  stripe phase is stabilized – has only been considered more recently, for instance via unrestricted Hartree-Fock calculations [54]. Although for a wide range of parameters the magnetic ground state is stripe-like (single- $\mathbf{Q}$ ), and therefore breaks tetragonal symmetry, hole-doped systems have been shown to display double- $\mathbf{Q}$  tetragonal magnetic states, consistent with what is observed experimentally [70–72]. In another set of studies of SDW order within the orbital basis, robust nodes in the SDW gap have been found, which give rise to “Dirac-like” band dispersions in the magnetically ordered state [41, 73, 74].

RPA calculations have also been employed to study the onset of on-site ferro-orbital order characterized by unequal occupations of the  $d_{xz}$  and  $d_{yz}$  orbitals [44, 45, 65]. A spontaneous ferro-orbital order is found within RPA, but only if  $2U' - J > U$ , i.e., when inter-orbital  $U'$  is substantially strong. For smaller  $U'$  ferro-orbital order does not develop. We return to this issue in Sec. IV, where we question the validity of RPA for such an analysis.

The main issue with orbital-basis models is that they do not distinguish high-energy and low-energy states, which makes it difficult to implement methods beyond RPA within this approach. The proposed modification of RPA relies on the assumption that magnetism comes from electronic states at higher energies and can be reasonably well captured within RPA in the orbital basis, while superconductivity and nematic order originate from interactions between low-energy fermions, mediated by already developed magnetic fluctuations. Along these lines, several groups used RPA in the orbital basis to obtain the magnetic susceptibility, and then focused on the low-energy sector to study magnetically-mediated superconductivity within BCS theory (Refs. [8, 12, 17, 18, 66, 75]) or magnetically-mediated nematicity [76, 77]. We will come back to these RPA studies in Section IV.

A different approach to superconductivity is based on models mixing localized spins interacting with itinerant electrons [20, 21, 78]. One idea promoted by some of these studies is that the SC gap is present everywhere in the BZ and its momentum-dependence closely follows one of the  $C_4$  symmetric lattice functions, e.g.,  $\cos k_x + \cos k_y$  [79]. This is very far from BCS theory, in which the gap is confined to the Fermi surface, because only there the pairing interaction can be logarithmically enhanced. We believe that the presence of a robust SC gap everywhere on the Fermi surface is highly unlikely in the first place because the interactions in FeSC are not overly strong, otherwise these systems would not display a metallic be-

havior. Another possibility studied in orbital-basis models [46, 56, 80] is an exotic pairing involving the combination of orbital and SC degrees of freedom.

### III. BAND-BASIS MODELS

We now discuss an alternative approach, which starts directly from the band-basis representation and treats the band states as the fundamental low-energy states instead of expressing them as linear combinations of orbital states  $d_{\mu, \mathbf{k}\sigma}^\dagger$ . In the band representation, the non-interacting Hamiltonian is diagonal in band indices and describes excitations near hole and electron pockets:

$$\mathcal{H}_0 = \sum_{m=1}^5 \varepsilon_m(\mathbf{k}) c_{m, \mathbf{k}\sigma}^\dagger c_{m, \mathbf{k}\sigma} \quad (15)$$

The band dispersions are parametrized as simple tight-binding or parabolic dispersions, according to the symmetries imposed by the positions of the centers of the various Fermi pockets, with no reference to their orbital content. The interacting Hamiltonian contains all possible interactions between these low-energy electronic states. These interactions were argued to contain angle-dependent terms, but in band-basis models these angle dependencies are imposed by the underlying  $C_4$  symmetry and the locations of the Fermi pockets, rather than the orbital content of the excitations [81]. For example, all pairing interactions contain  $\cos 4n\theta$  dependencies, because these angular dependencies are consistent with  $C_4$  symmetry. The pairing interactions involving states near the electron pockets, however, also contain  $\cos(4n+2)\theta$  terms, because the center of the electron pockets are not along the diagonal directions in the 1-Fe BZ.

We emphasize that these band-basis models cannot be described as the low-energy versions of the orbital-basis models from Section (II), expressed in a different basis. In particular, these band models cannot describe orbital order simply because they do not distinguish between different orbitals. We will discuss the proper low-energy models later, in Section IV.

Band models were quite successful in the description of SDW and SC orders and the interplay between them [11, 59, 82–85]. This success implies that, while the orbital composition of the low-energy states does play some role for magnetism and superconductivity, it does not provide the crucial ingredient for these two orders, as opposed to orbital order.

Band-based models are constructed to capture the low-energy states near the Fermi surfaces and their application to FeSCs is based on the assumption that not only superconductivity but also SDW magnetism are low-energy phenomena. Namely, SDW magnetism is viewed as the result of near-nesting between hole-like and electron-like bands. In this respect, the reasonings for band-basis models and for orbital-basis models are different.

Because only low energies are involved in band-basis models, one can go beyond RPA and, e.g., analyze the interplay not only between long-range SDW and SC orders but also between SC and SDW fluctuations. Another advantage of band-basis models is that they can be straightforwardly extended to analyze composite Ising-nematic order [86–88], which is related to the order parameter manifold of stripe SDW magnetism rather than with the orbital composition of the excitations.

This discussion raises the question of whether it may be more appropriate to use the band basis to describe magnetism and superconductivity in FeSC [74]. In this section we briefly review the results of the models conceived entirely in the band basis. As in the previous section, we first discuss the non-interacting Hamiltonian, then introduce the order parameters, and then include interactions to discuss the instabilities of these models at the mean-field level and beyond it.

### A. Non-interacting Hamiltonian

As discussed above, a generic FeSC contains two small hole pockets at the  $\Gamma$  point, two electron pockets at  $X$  and  $Y$  points with similar sizes, and may also contain another hole pocket at the  $M$  point. The tetragonal symmetry requires that the hole pockets must be  $C_4$  symmetric (i.e. invariant under a  $90^\circ$  rotation), since they are centered at either the center or the corner of the BZ, whereas the electron pockets only need to be  $C_2$  symmetric (i.e. invariant under a  $180^\circ$  rotation), since they are centered at the sides of the BZ. Note that the two electron pockets are related to each other by a  $90^\circ$  rotation. Also, because the pockets are assumed to be small, their band dispersions can be expanded in powers of the relative momentum with respect to the center of the pockets, in which case one can assume parabolic dispersions.

Under these conditions, one can write an effective 5-band model for electronic states residing near the hole and electron pockets. Here, we focus on a simplified model containing three bands [85, 86] – one central hole pocket and two elliptical electron pockets centered at the  $X$  and  $Y$  points, as shown in Fig. 8. The motivation to neglect the  $M$  hole pocket is because it is not generically present in all compounds [27]. The restriction to a single hole-pocket at the  $\Gamma$  point is less justified, but the argument is that in general one hole pocket has better nesting with the electron pockets than the other [85].

The non-interacting Hamiltonian of the 3-band model is written as:

$$\begin{aligned} \mathcal{H}_0 = & \sum_{\mathbf{k}} \varepsilon_h(\mathbf{k}) c_{h,\mathbf{k}\sigma}^\dagger c_{h,\mathbf{k}\sigma} \\ & + \sum_{\mathbf{k}, i=X,Y} \varepsilon_{e_i}(\mathbf{k} + \mathbf{Q}_i) c_{e_i,\mathbf{k}+\mathbf{Q}_i,\sigma}^\dagger c_{e_i,\mathbf{k}+\mathbf{Q}_i,\sigma} \end{aligned} \quad (16)$$

with parabolic band dispersions:

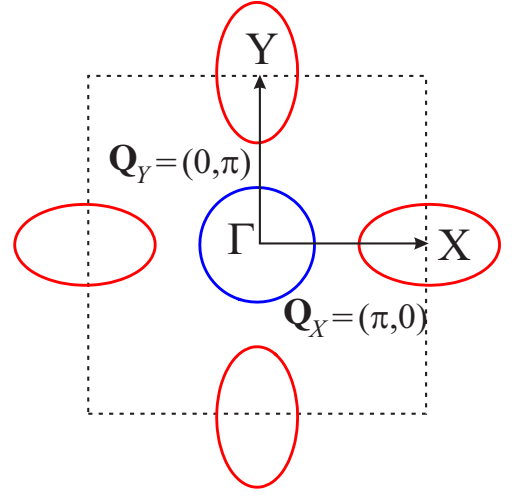


Figure 8. The effective three-band model: in the 1-Fe BZ, a circular hole pocket (blue) is centered at  $\Gamma$ , whereas elliptical electron pockets (red) are centered at  $X$  and  $Y$ . Figure adapted from Ref. [86].

$$\begin{aligned} \varepsilon_h(\mathbf{k}) &= \varepsilon_{h,0} - \frac{k^2}{2m} - \mu \\ \varepsilon_{e_X}(\mathbf{k} + \mathbf{Q}_X) &= -\varepsilon_{e,0} + \frac{k_x^2}{2m_x} + \frac{k_y^2}{2m_y} - \mu \\ \varepsilon_{e_Y}(\mathbf{k} + \mathbf{Q}_Y) &= -\varepsilon_{e,0} + \frac{k_x^2}{2m_x} + \frac{k_y^2}{2m_y} - \mu \end{aligned} \quad (17)$$

Similarly, one can consider effective tight-binding dispersions for each band, as done in Refs. [87, 89]. The main advantage of the parabolic dispersions is their simplicity and convenience for analytical calculations. Hereafter, we simplify the notation by leaving it implicit that the momenta of the electron-like states are measured relative to the respective  $\mathbf{Q}_i$ .

One of the goals of the band-basis models is to relate SDW magnetism to nesting properties of the band structure, as manifested in Fig. 8. Perfect nesting requires  $\varepsilon_h(\mathbf{k}) = -\varepsilon_{e_i}(\mathbf{k} + \mathbf{Q}_i)$ , which is clearly not the case for the real materials, as the hole and electron pockets do not have identical shapes. Instead, the FeSC usually display pairs of points satisfying the condition  $\varepsilon_h(\mathbf{k}_{\text{hs}}) = \varepsilon_{e_i}(\mathbf{k}_{\text{hs}} + \mathbf{Q}_i) = 0$  – the so-called hot spots. Yet, the hypothetical limit of perfect nesting is very useful to gain insight into the generic properties of the model, as we will show latter. In this regard, it is useful to consider an alternative parametrization of the band dispersions in terms of the angle  $\theta$  measured with respect to the  $k_x$  axis [84]:

$$\begin{aligned} \varepsilon_h(\mathbf{k}) &= -\varepsilon_{\mathbf{k}} \\ \varepsilon_{e_X}(\mathbf{k} + \mathbf{Q}_X) &= \varepsilon_{\mathbf{k}} - (\delta_\mu + \delta_m \cos 2\theta) \\ \varepsilon_{e_Y}(\mathbf{k} + \mathbf{Q}_Y) &= \varepsilon_{\mathbf{k}} - (\delta_\mu - \delta_m \cos 2\theta) \end{aligned} \quad (18)$$

The parameter  $\delta_\mu$  is proportional to the sum of the chemical potential and the offset between the top of the hole pocket and the bottom of the electron pocket, whereas the parameter  $\delta_m$  is proportional to the ellipticity of the electron pockets. The condition for perfect nesting is  $\delta_\mu = \delta_m = 0$ . This parametrization is convenient because the expansion near perfect nesting can be performed in powers of these two parameters.

## B. Order parameters

Before discussing the effects of interactions we introduce different order parameters in the band basis. To avoid lengthy formulas, we focus on the 3-band model. The existence of the nesting vectors  $\mathbf{Q}_X$  and  $\mathbf{Q}_Y$  allows one to introduce several density-wave order parameters involving fermions from the electron and hole pockets [11, 59, 82, 90]. We define:

$$\begin{aligned}\Delta_{\text{CDW},j}(\mathbf{k}) &\propto c_{h,\mathbf{k}\alpha}^\dagger \delta_{\alpha\beta} c_{e_j,\mathbf{k}+\mathbf{Q}_j\beta} + h.c. \\ \Delta_{\text{iCDW},j}(\mathbf{k}) &\propto i c_{h,\mathbf{k}\alpha}^\dagger \delta_{\alpha\beta} c_{e_j,\mathbf{k}+\mathbf{Q}_j\beta} + h.c. \\ \Delta_{\text{SDW},j}(\mathbf{k}) &\propto c_{h,\mathbf{k}\alpha}^\dagger \sigma_{\alpha\beta} c_{e_j,\mathbf{k}+\mathbf{Q}_j\beta} + h.c. \\ \Delta_{\text{iSDW},j}(\mathbf{k}) &\propto i c_{h,\mathbf{k}\alpha}^\dagger \sigma_{\alpha\beta} c_{e_j,\mathbf{k}+\mathbf{Q}_j\beta} + h.c.\end{aligned}\quad (19)$$

where  $j = X, Y$  and  $c_h, c_{e_j}$  label fermionic operators near hole and electron pockets. The order parameters  $\Delta_{\text{CDW},j}$  and  $\Delta_{\text{SDW},j}$  describe charge and spin density-waves (CDW and SDW, respectively) with transferred momenta  $\mathbf{Q}_j$ , whereas  $\Delta_{\text{iCDW},j}$  and  $\Delta_{\text{iSDW},j}$  describe charge-current (iCDW) and spin-current (iSDW) density-waves. It is also useful to introduce the order parameters with momentum  $\mathbf{Q}_X + \mathbf{Q}_Y = (\pi, \pi)$ , which involve fermions from the two electron pockets, e.g., the Neel order parameter:

$$\Delta_{\text{Neel}}(\mathbf{k}) \propto c_{e_X,\mathbf{k}+\mathbf{Q}_X\alpha}^\dagger \sigma_{\alpha\beta} c_{e_Y,\mathbf{k}+\mathbf{Q}_Y\beta} + h.c. \quad (20)$$

However, because the two electron pockets are not nested, the instabilities at momentum  $\mathbf{Q}_X + \mathbf{Q}_Y$  are sub-leading to the ones at momenta  $\mathbf{Q}_X$  and  $\mathbf{Q}_Y$ , at least at weak coupling.

We also introduce the SC order parameters. In principle, they have angular dependencies already in the band basis due to the locations and symmetries of the Fermi surfaces. In some cases, this dependence can even lead to accidental nodes, particularly on electron pockets [81, 84, 91–94]. We will not dwell into this issue here and focus instead on the angle-independent parts of SC order parameters. It is useful to define the order parameters for each pocket:

$$\begin{aligned}\Delta_h(\mathbf{k}) &\propto c_{h,-\mathbf{k}\downarrow} c_{h,\mathbf{k}\uparrow} + h.c. \\ \Delta_{e_X}(\mathbf{k}) &\propto c_{e_X,-\mathbf{k}-\mathbf{Q}_X\downarrow} c_{e_X,\mathbf{k}+\mathbf{Q}_X\uparrow} + h.c. \\ \Delta_{e_Y}(\mathbf{k}) &\propto c_{e_Y,-\mathbf{k}-\mathbf{Q}_Y\downarrow} c_{e_Y,\mathbf{k}+\mathbf{Q}_Y\uparrow} + h.c.\end{aligned}\quad (21)$$

Each SC order parameter  $\Delta$  (often called the gap function) has an amplitude and a phase. We define all gaps such that in the ordered state they have the same global phase and will not consider phase fluctuations. Because the system has tetragonal symmetry, the three gap functions can be recast in terms of three different combinations, two of which transform as  $A_{1g}$  (*s*-wave) representation, and one as  $B_{1g}$  (*d*-wave) representation [95]:

$$\begin{aligned}\Delta_{s^{++}} &= \sin \Psi \Delta_h + \frac{\cos \Psi}{\sqrt{2}} (\Delta_{e_X} + \Delta_{e_Y}) \\ \Delta_{s^{+-}} &= \cos \Psi \Delta_h - \frac{\sin \Psi}{\sqrt{2}} (\Delta_{e_X} + \Delta_{e_Y}) \\ \Delta_d &= \frac{1}{\sqrt{2}} (\Delta_{e_X} - \Delta_{e_Y})\end{aligned}\quad (22)$$

The mixing angle  $\Psi$  depends on the strength of the pairing interactions  $V_1$  between the *h* and the  $e_{X/Y}$  pockets and  $V_2$  between the  $e_X$  and  $e_Y$  pockets according to:

$$\tan \Psi = \frac{\sqrt{8V_1^2 + V_2^2} - V_2}{2\sqrt{2}V_1} \quad (23)$$

The interpretation of these three SC order parameters is straightforward: in the  $s^{++}$ -wave state the gap functions on different pockets all have the same sign; in the  $s^{+-}$ -state the gaps on the hole and on the electron pockets have different signs; and in the *d*-wave state the gaps on the two electron pockets have opposite signs. Note that the absence of the *d*-wave component on the hole pockets is just the result of our neglect of the angular dependencies. In reality, a *d*-wave gap on the hole pocket behaves as  $\cos 2\theta$ .

One can also define Pomeranchuk order parameters at zero momentum transfer  $\mathbf{Q} = 0$ . In the charge channel we have

$$\begin{aligned}\Delta_{\text{POM}}^h(\mathbf{k}) &\propto c_{h,\mathbf{k}\alpha}^\dagger \delta_{\alpha\beta} c_{h,\mathbf{k}\beta} + h.c. \\ \Delta_{\text{POM}}^X(\mathbf{k}) &\propto c_{e_X,\mathbf{k}+\mathbf{Q}_X\alpha}^\dagger \delta_{\alpha\beta} c_{e_X,\mathbf{k}+\mathbf{Q}_X\beta} + h.c. \\ \Delta_{\text{POM}}^Y(\mathbf{k}) &\propto c_{e_Y,\mathbf{k}+\mathbf{Q}_Y\alpha}^\dagger \delta_{\alpha\beta} c_{e_Y,\mathbf{k}+\mathbf{Q}_Y\beta} + h.c.\end{aligned}\quad (24)$$

The development of a non-zero  $\sum_{\mathbf{k}} \langle \Delta_{\text{POM}}^X(\mathbf{k}) - \Delta_{\text{POM}}^Y(\mathbf{k}) \rangle$  breaks  $C_4$  lattice rotational symmetry down to  $C_2$  and gives rise to nematic order [86], which in the band-only model is not identified with any orbital order, but still gives rise to a *d*-wave distortion of the electron Fermi surfaces. Another possibility is the appearance of  $s^{+-}$  Pomeranchuk order with  $\sum_{\mathbf{k}} \langle \Delta_{\text{POM}}^X(\mathbf{k}) + \Delta_{\text{POM}}^Y(\mathbf{k}) \rangle$  and  $\sum_{\mathbf{k}} \langle \Delta_{\text{POM}}^h(\mathbf{k}) \rangle$  with opposite signs. This leads to either shrinking or expansion of the sizes of both hole and electron pockets, such that the total number of charge carriers is preserved [96, 97]. Like we said, an order parameter of this kind does not break any symmetry and is generally non-zero at any temperature, but it can be strongly enhanced around a particular temperature.

### C. Interaction effects

The interactions in the band-basis model are not necessarily given by on-site terms only. Instead, they include all possible interactions involving pairs of fermions from the same or from different bands. As a result, the number of interaction terms increases with the number of bands. For the three-band model introduced above, there are eight distinct interaction terms [81]:

$$\begin{aligned}
\mathcal{H}_{\text{int}} = & U_1 \sum_i c_{h\alpha}^\dagger c_{e_i\beta}^\dagger c_{e_i\beta} c_{h\alpha} + U_2 \sum_i c_{h\alpha}^\dagger c_{e_i\beta}^\dagger c_{h\beta} c_{e_i\alpha} \\
& + \frac{U_3}{2} \sum_i \left( c_{h\alpha}^\dagger c_{h\beta}^\dagger c_{e_i\beta} c_{e_i\alpha} + \text{h.c.} \right) \\
& + \frac{U_4}{2} \sum_i c_{e_i\alpha}^\dagger c_{e_i\beta}^\dagger c_{e_i\beta} c_{e_i\alpha} + \frac{U_5}{2} \sum c_{h\alpha}^\dagger c_{h\beta}^\dagger c_{h\beta} c_{h\alpha} \\
& + U_6 \sum c_{e_X\alpha}^\dagger c_{e_Y\beta}^\dagger c_{e_Y\beta} c_{e_X\alpha} + U_7 \sum c_{e_X\alpha}^\dagger c_{e_Y\beta}^\dagger c_{e_X\beta} c_{e_Y\alpha} \\
& + \frac{U_8}{2} \sum \left( c_{e_X\alpha}^\dagger c_{e_X\beta}^\dagger c_{e_Y\beta} c_{e_Y\alpha} + \text{h.c.} \right) \quad (25)
\end{aligned}$$

These terms correspond to density-density interactions ( $U_1$ ,  $U_4$ ,  $U_5$ ,  $U_6$ ), spin-exchange interactions ( $U_2$ ,  $U_7$ ), and pair-hopping interactions ( $U_3$ ,  $U_8$ ), all of which have purely electronic origin. These interactions should be viewed as input parameters rather than the combinations of Hubbard and Hund interactions from Eq. (4). The reasoning is that Hubbard and Hund interaction terms become angle-dependent once we transform from orbital to band basis, due to the matrix elements of Eq. (5), while  $U_i$  in Eq. (25) are taken to be angle-independent. We will come back to this point in Section IV.

#### 1. Renormalization Group (RG) analysis: the basics

As we discussed above, the advantage of using the band basis is that one can focus on the low-energy sector and go beyond mean-field (RPA) analysis. To do this, in this and next Sections we apply the RG technique. The RG machinery (either numerical functional RG or analytical parquet RG) allows one to analyze how different interaction channels compete with each other as one progressively integrates out fermions with higher energies, starting from the upper energy cutoff  $\Lambda$  of the low-energy sector (loosely defined as the scale at which corrections to the parabolic dispersion near the  $X$ ,  $Y$ , and  $\Gamma$  points become substantial) and moving down in energy [59, 98–101]. The couplings in different interaction channels all evolve in this process. The flow of the couplings is described by a set of differential equations

$$\frac{dU_i(L)}{dL} = a_{ijk} U_j(L) U_k(L) \quad (26)$$

where  $L \equiv \log(\frac{\Lambda}{E})$  is a running RG variable, which increases as the energy  $E$  decreases away from the cutoff  $\Lambda$ .

The running interactions  $U_i$  are all functions of  $L$ . An instability develops at a critical RG scale  $L_c = \log \Lambda/E_c$ , at which at least some of the couplings diverge. The critical temperature for the instability is of the order of  $E_c$ .

One of the goals of the RG analysis is to verify whether the low-energy behavior of a system is universal, i.e., that the running couplings tend to the same values under RG for different initial interactions. In the cases we discuss below, some couplings diverge upon approaching the scale  $L_c$ , but their ratios tend to finite, fixed values (the value of  $L_c$  itself does depend on the bare values of the interactions). In RG language, this is called a fixed trajectory. There can be more than one fixed trajectory, in which case each has a finite basin of attraction in the parameter space of initial interactions. For each fixed trajectory, one can find with certainty what is the leading and the subleading instability in the system.

To select what kind of order develops at  $L = L_c$ , one needs to move the RG analysis to the next level and obtain the RG equations for the flow of the vertices in different instability channels,  $\Gamma_j$ . Each vertex is renormalized by a particular combination of the interactions  $U_i$ . For the channels in which the vertex renormalizations are logarithmical, like SC or SDW, vertex renormalizations are given by the series of ladder diagrams with either particle-hole or particle-particle bubble in every cross-section, and with interactions treated as the running ones. To logarithmical accuracy the summation of these diagrams is equivalent to solving the differential equations

$$\frac{d\Gamma_j}{dL} = \Gamma_j u^j \quad (27)$$

where  $u^j$  is a dimensionless coupling in the channel  $j$  (the combination of  $U_i N_i$ , where  $N_i$  is of the order of the density of states  $N_F$ ). The susceptibilities  $\chi_j$  are given by bubble diagrams with  $\Gamma_j$  in the vertices and obey

$$\frac{d\chi_j}{dL} = \Gamma_j^2 \quad (28)$$

Solving Eq. (27) with the RG solution for  $u_j$  as an input, substituting the result into (28) and solving for  $\chi_j(L)$ , one obtains  $\chi_j(L) \propto 1/(L_c - L)^{\alpha_j}$ . In general, the exponents  $\alpha_j$  are all different. The channel in which  $\alpha_j$  has the largest value is the leading candidate among the logarithmical channels to develop an order below the instability.

We will see, however, that the situation in at least some FeSC is more involved because the susceptibility in initially non-logarithmical channels, like Pomeranchuk channels, also flows with  $L$  due to renormalizations that involve the running couplings  $U_i(L)$ . We will show that the corresponding susceptibilities scale with  $L$  as  $\chi_j(L) \propto 1/(L_c - L)$ . If  $\alpha_j$  in the leading logarithmical channel is smaller than one, the susceptibilities in the Pomeranchuk channels diverge with a higher exponent. In this situation, the system may actually develop

a Pomeranchuk order below the instability. We discuss this in more detail in Sec. IV C 4.

The advantage of the RG approach over mean-field approaches, such as RPA, is that it allows one to analyze mutual feedbacks between fluctuations in different channels (e.g., how superconducting fluctuations modify SDW fluctuations, which in turn contribute to the pairing interaction). The drawback of RG is that it is, by construction, a weak-coupling analysis. Moreover, the selection of diagrams which are included into RG analysis is justified only if vertex renormalizations in the particle-hole channel (associated with density-wave instabilities) are logarithmic at some transferred momentum, like in the Cooper channel (associated with the superconducting instabilities). In FeSC, this condition is generally satisfied because renormalizations in the particle-hole channel with transfer momenta  $\mathbf{Q}_X$  and/or  $\mathbf{Q}_Y$  involve electronic states from hole-like and electron-like bands, and a particle-hole bubble made of fermions from a hole and an electron band depends logarithmically of the external frequency, much like a Cooper bubble. But this only holds at energies larger than  $|\delta_m|$  and  $|\delta_\mu|$  in Eq. 18, i.e. RG can be rigorously justified down to the lowest energies only at perfect nesting. Away from perfect nesting, the parquet RG flow of the couplings towards one or another fixed trajectory holds between the upper cutoff of the low-energy theory and, roughly, the largest Fermi energy,  $E_F$ . At  $E < E_F$  different channels no longer “talk” to each other. If the scale  $L = L_c$  falls into this range, the selection of the leading instability can be fully described within parquet RG. If the RG scale  $L$  reaches  $L_F = \log \Lambda/E_F$  before the instability develops, parquet RG allows one to determine the values of the running couplings at  $L = L_F$ . At smaller energies (larger  $L$ ) one can use, e.g., RPA with these couplings as inputs. For a recent approach to extend RG equations to  $L \rightarrow L_F$  see Ref. [102].

## 2. Two-band model

To analyze how interactions select between different density-wave and SC instabilities, we first consider a toy two-band model with one hole and one of the two electron pockets, i.e. we consider SDW and CDW orders with a single ordering vector. This model is blind to  $d$ -wave superconductivity and  $d$ -wave Pomeranchuk order, yet it offers interesting insights into the interplay between SDW, iCDW, and  $s^{+-}$  superconductivity. In terms of the interactions, this toy model has five couplings  $U_1 - U_5$ , while  $U_6 = U_7 = U_8 = 0$ .

*Perfect nesting,  $E_F = 0$*

We first consider the limit of perfect nesting,  $\delta_\mu = \delta_m = 0$  in Eq. (18), when both hole and electron bands just touch the Fermi level:  $\epsilon_{e,h} = \pm k^2/(2m)$ . The masses will be absorbed into dimensional couplings. For

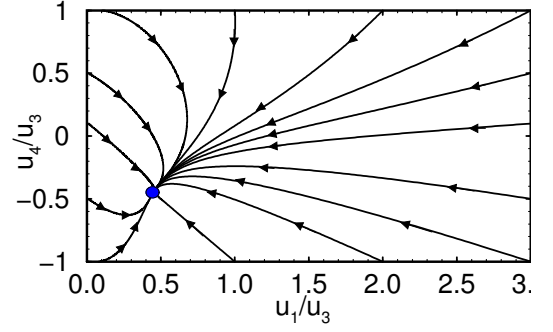


Figure 9. RG flows of the two-band model in the  $\left(\frac{u_1}{u_3}, \frac{u_4}{u_3}\right)$  plane. The fixed point is shown in blue. Figure from Ref. [59].

free fermions, the susceptibilities in the SDW and CDW channels with real and imaginary order parameters and in  $s^{++}$  and  $s^{+-}$  SC channels are all degenerate and scale as  $\chi_0 \propto \ln(\Lambda/T)$ , where  $\Lambda$  is the bandwidth. Once the interactions from Eq.(25) are included, this degeneracy is lifted. Within RPA, different susceptibilities become  $\chi_j = \chi_0 / (1 - \Gamma_j \chi_0)$ , where [59]:

$$\begin{aligned} \Gamma_{\text{SDW}} &= U_1 + U_3 & \Gamma_{i\text{SDW}} &= U_1 - U_3 \\ \Gamma_{\text{CDW}} &= U_1 - U_3 - 2U_2 & \Gamma_{i\text{CDW}} &= U_1 + U_3 - 2U_2 \\ \Gamma_{s^{+-}} &= -U_4 + U_3 & \Gamma_{s^{++}} &= -U_4 - U_3 \end{aligned} \quad (29)$$

When all  $U_i$  are equal (Hubbard model in the band basis), the leading instability within RPA is towards SDW magnetism. The interaction in the SC  $s^{++}$  channel is repulsive, and the one in the  $s^{+-}$  channel vanishes ( $\Gamma_{s^{+-}} = 0$ ,  $\Gamma_{s^{++}} < 0$ ).

We now apply RG. We do not give the details of this calculation, and just list the results. The reader interested in details is referred to the relevant literature [59]. There is one stable fixed trajectory for positive (repulsive) interactions  $U_1 - U_5$ . All interactions diverge near  $L = L_c$ , but their ratios tend to finite values. Specifically, the dimensionless  $u_j = U_j N_F$ , where  $N_F$  is the density of states, evolve near  $L = L_c$  as  $u_1 \propto 1/(L_c - L)$ ,  $u_1/u_3 = -u_4/u_3 = -u_5/u_3 = 1/\sqrt{5}$ , and  $u_2/u_3 = 0$ . Fig. 9 illustrates the RG flow in the  $\left(\frac{u_1}{u_3}, \frac{u_4}{u_3}\right)$  plane, highlighting the stable fixed point  $\left(\frac{1}{\sqrt{5}}, -\frac{1}{\sqrt{5}}\right)$ .

We now analyze use the running couplings  $u_i$  as inputs and analyze the flow of the vertices and susceptibilities in different channels. Solving Eqs. (27) and (28) we obtain that the susceptibilities in the SDW, iCDW, and  $s^{+-}$  SC channel diverge as  $1/(L_0 - L)^\alpha$  with the same exponent  $\alpha = (\sqrt{5} - 2)/3 = 0.08$ , while susceptibilities in the iSDW, CDW, and  $s^{++}$  SC channel do not diverge. The outcome is that the system has an emergent enhanced  $O(6)$  symmetry – the three order parameters form a 6-dimensional super-vector  $\mathbf{N} = (\Delta_{\text{SDW}}, \Delta_{s^{+-}}, \Delta_{i\text{CDW}})$  [59, 103]. This has important implications for the competition between superconductivity and SDW, as we

discuss below.

*Away from perfect nesting, finite  $E_F$ .*

At non-zero  $E_F$  (and hence non-zero  $\delta_\mu$  and, in general, also  $\delta_m$ ), the parquet RG flow discussed above holds as long as the running energy is larger than  $E_F$ , i.e. as long as  $L < L_F$ . For  $L > L_F$ , the RG equations change as the six different channels decouple. In most FeSC, the largest Fermi energy is about 100 meV, while  $\Lambda$  is of order of eV. Thus, even though  $E_F \ll \Lambda$ , it is likely that  $L_F < L_c$ , implying that the instability is not really reached within parquet RG. At  $L = L_F$ , the coupling in the SDW channel is the largest, and the ones in iCDW and  $s^{+-}$  channels are smaller (Refs. [59, 81]). At  $L > L_F$ , the only channel in which interactions continue to grow logarithmically is the  $s^{+-}$  SC channel, while the couplings in SDW and iCDW channels eventually saturate. If the superconducting  $u^{SC}(L)$  is already attractive at  $L = L_F$  and is close to  $u^{SDW}$ ,  $s^{+-}$  superconductivity is the most likely outcome. If  $u^{SDW}(L_F)$  is large while the other  $u^j$  are smaller, the system likely develops SDW order, and if all  $u^j$  are small at  $L = L_F$  and the SC interaction is repulsive, the system likely remains a metal down to  $T = 0$  (see Fig. 10). For some initial input parameters, the system may also develop iCDW order [90, 104].

*Ginzburg-Landau free energy*

Within the two-band model one can study the interplay between  $s^{+-}$  superconductivity and SDW at  $E < E_F$  in more detail by deriving the Ginzburg-Landau free energy for the coupled  $s^{+-}$  and SDW order parameters  $\Delta_{s^{+-}}$  and  $\Delta_{SDW}$ . This is accomplished by performing a Hubbard-Stratonovich transformation of the interaction terms in Eq. (25) in the SDW and  $s^{+-}$  channels. One can then integrate out the electronic degrees of freedom and expand in powers of the two order parameters. This yields [83, 84, 105]:

$$F(\Delta_{s^{+-}}, \Delta_{SDW}) = \frac{a_s}{2} \Delta_{s^{+-}}^2 + \frac{u_s}{4} \Delta_{s^{+-}}^4 + \frac{a_m}{2} \Delta_{SDW}^2 + \frac{u_m}{4} \Delta_{SDW}^4 + \frac{\gamma}{2} \Delta_{s^{+-}}^2 \Delta_{SDW}^2 \quad (30)$$

All Ginzburg-Landau coefficients are given microscopically in terms of the band dispersions (17) and the effective SDW and  $s^{+-}$  SC interactions (see Refs. [83, 84] for details). Despite the fact that  $\gamma > 0$ , indicating that the two orders compete with each other, they coexist microscopically if  $\gamma < \sqrt{u_s u_m}$ . Otherwise, if  $\gamma > \sqrt{u_s u_m}$ , the SDW and  $s^{+-}$  SC states phase-separate as the transition from one phase to the other is first-order. Thus, it is convenient to define the parameter  $\bar{g} \equiv \gamma - \sqrt{u_s u_m}$ .

The microscopic calculation reveals that, for perfect nesting,  $\bar{g} = 0$ , i.e. the system is at the edge between coexistence and phase separation [105]. In this case, it is clear that the free energy near the multi-critical point

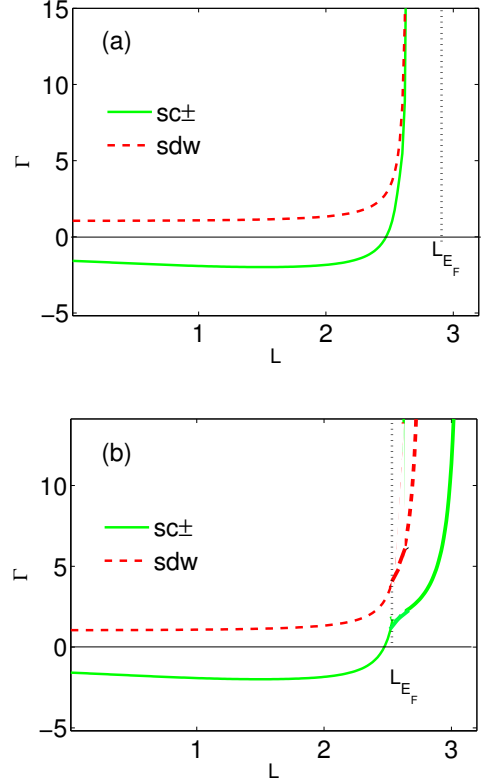


Figure 10. RG flow of the SDW (red/dashed curve) and  $s^{+-}$  SC (green/solid curve) vertices for the two-band model; (a) denotes the case  $L_F > L_c$ , whereas (b) denotes the case  $L_F < L_c$ . Figure from Ref. [81].

has an emergent  $O(5)$  symmetry, since only the combination  $(\Delta_{s^{+-}}^2 + \Delta_{SDW}^2)$  appears in Eq. (30). This is another manifestation of the degeneracy between SDW and  $s^{+-}$  SC at perfect nesting. Deviations from perfect nesting may tip the balance to either  $\bar{g} < 0$  (promoting microscopic coexistence) or  $\bar{g} > 0$  (promoting macroscopic phase separation), as shown in Fig. 11.

### 3. Three-band model

Despite all the interesting insights offered by the 2-band model, it has a major drawback: by considering the coupling between one hole- and one electron-pocket only, it assumes that the selected magnetic order has a single ordering vector and is therefore insensitive to spontaneous tetragonal symmetry breaking, which is present in the phase diagram of the FeSC (see Fig. 1). The tetragonal symmetry breaking can be captured within the 3-band model as there are two possibilities for SDW order there, with ordering vectors  $\mathbf{Q}_X$  and  $\mathbf{Q}_Y$ . A spontaneous selection of one of these orders breaks  $C_4$  symmetry down to  $C_2$ .

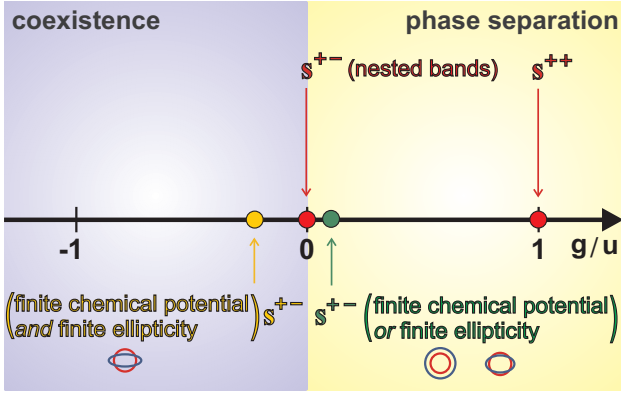


Figure 11. Schematic representation of the fate of the competing SC and SDW orders in the two-band model: for perfect nesting,  $s^{+-}$  is at the verge of microscopic coexistence or macroscopic phase separation with SDW ( $\bar{g} = 0$ ), whereas  $s^{++}$  is deep in the phase-separation region ( $\bar{g} > 0$ ). Deviations from perfect nesting may take the  $s^{+-}$  state to either regime, whereas  $s^{++}$  remains in the phase-separation region. Figure adapted from Ref. [105].

### RG analysis

We first briefly discuss how the RG results of the 2-band model are modified in the 3-band case [81]. Again, we just quote the results and refer to Ref. [81] for details. Similarly to the 2-band case, one finds a divergence of the vertices  $\Gamma_{\text{SDW}}$  and  $\Gamma_{s^{+-}}$  at a finite running coupling  $L_c \equiv \log\left(\frac{\Lambda}{E_c}\right)$ . However, in contrast to the 2-band model, where the two instabilities are degenerate, here  $u^{s^{+-}}$  becomes larger than  $u^{\text{SDW}}$  as the instability is approached, as shown in Fig. 12. This happens by purely geometrical reasons (two electron pockets instead of one). As a result,  $s^{+-}$  superconductivity wins over SDW even in the case of perfect nesting. The situation however changes if the Fermi energy is not small, i.e. if  $L_F < L_c$ . Then, the leading instability is given by whichever vertex is larger at the scale  $L_F$ . As shown in the same figure, for large enough Fermi energy values, the leading instability becomes the SDW and not the SC one [81].

To complete the RG analysis, one should use the results for the flow of the couplings and compute the susceptibilities in the SDW and SC channels, and also in the channels with  $\mathbf{Q} = 0$  order. This analysis shows that not only  $s^{+-}$  superconductivity wins over SDW, but also that the growth of the SDW susceptibility is halted due to the negative feedback effect from increasing SC fluctuations. It also shows that the susceptibilities in the  $\mathbf{Q} = 0$  channels for the order parameters in Eq. (24), which either break  $C_4$  symmetry down to  $C_2$  (leading to a nematic order) or simultaneously shrink/expand hole and electron pockets, grow with larger exponents than the SC susceptibility. Thus, these  $\mathbf{Q} = 0$  orders may occur before superconductivity, if the system parameters

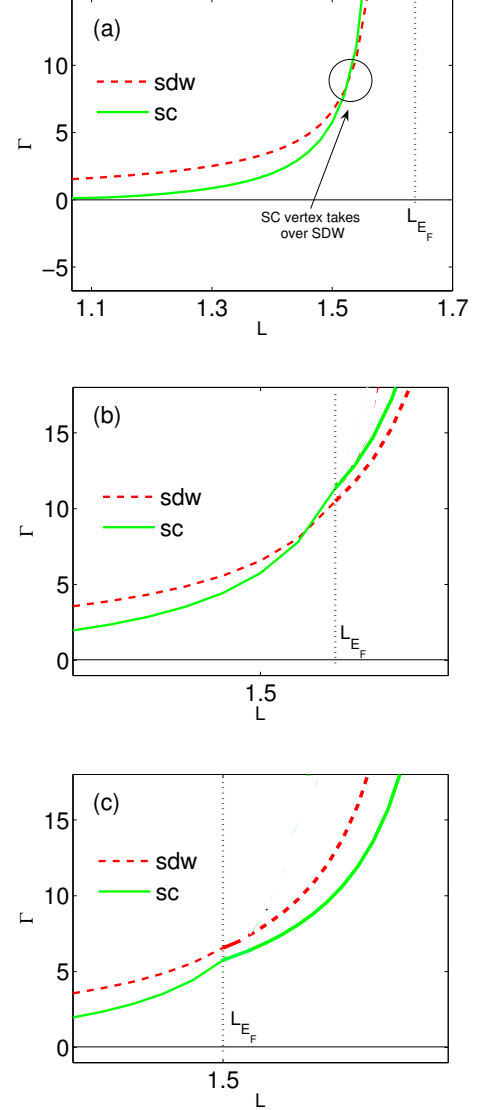


Figure 12. RG flows of the  $s^{+-}$  SC (green/solid) and SDW (red/dashed) vertices for the three-band model for different values of the ratio  $L_F/L_c$ . Figure from Ref. [81].

allow the RG flow run long enough. We will not focus on this physics here but discuss it in detail in Sec. IV where we include the orbital composition of the Fermi pockets.

### The selection of the magnetic order

An important question is which type of magnetic order is selected, if the SDW instability occurs prior to superconductivity. Because there are two possible SDW order parameters,  $\Delta_{\text{SDW},X}$  and  $\Delta_{\text{SDW},Y}$ , with two different ordering vectors,  $\mathbf{Q}_X$  and  $\mathbf{Q}_Y$ , there are two possibilities for the magnetically ordered state: either both order parameters condense simultaneously, giving rise to a double- $\mathbf{Q}$  magnetic phase, or only one of the

order parameters condense, giving rise to a single- $\mathbf{Q}$  stripe magnetic phase [54, 85, 87, 106–109]. This issue has important implications for the onset of nematic order, as we will discuss shortly. The selection of the magnetic order cannot be determined coming from the magnetically-disordered phase because the susceptibilities  $\chi_{\mathbf{Q}_X}$  and  $\chi_{\mathbf{Q}_Y}$  are identical in this regime. To select the type of SDW order one needs to go into the ordered phase and analyze quartic couplings between the two magnetic order parameters  $\Delta_{\text{SDW},X}$  and  $\Delta_{\text{SDW},Y}$ .

To do this, one can derive the Ginzburg-Landau free energy for  $\Delta_{\text{SDW},X}$  and  $\Delta_{\text{SDW},Y}$  from the low-energy fermionic model. The procedure is similar to the one described above to study the competition between magnetism and superconductivity. Here we only focus on the SDW component. The interacting terms in Eq. (25) are decoupled in the SDW channel via appropriate Hubbard-Stratonovich transformations. After integrating out the electronic degrees of freedom in the partition function and expanding in powers of the order parameters, we obtain the magnetic free energy (the SDW subscript is omitted for simplicity) [86]:

$$F[\Delta_X, \Delta_Y] = \frac{a}{2} (\Delta_X^2 + \Delta_Y^2) + \frac{u}{4} (\Delta_X^2 + \Delta_Y^2)^2 - \frac{g}{4} (\Delta_X^2 - \Delta_Y^2)^2 + w (\Delta_X \cdot \Delta_Y)^2 \quad (31)$$

Before discussing the values of the Ginzburg-Landau coefficients obtained from the microscopic model, we discuss the possible ground states of Eq. (31). The first two terms depend only on the combination  $(\Delta_X^2 + \Delta_Y^2)$ , and therefore do not distinguish between single- $\mathbf{Q}$  or double- $\mathbf{Q}$  phases. The last two terms do:  $g > 0$  favors a state in which either  $\Delta_X$  or  $\Delta_Y$  vanish (single- $\mathbf{Q}$ ), whereas  $g < 0$  favors a state in which  $\Delta_X = \Delta_Y$  (double- $\mathbf{Q}$ ). Within the double- $\mathbf{Q}$  subspace,  $w > 0$  favors the configuration in which  $\Delta_X \perp \Delta_Y$ , whereas  $w < 0$  favors the configuration in which  $\Delta_X \parallel \Delta_Y$ .

Fig. 13 shows the complete phase diagram in the  $(g, w)$  plane, together with the depictions of different ground states in real space [110]. For  $g > \max(0, -w)$ , the system develops a stripe-type magnetic state in which either  $\Delta_X \neq 0$  or  $\Delta_Y \neq 0$ . As it is apparent in the figure, this state breaks the  $C_4$  tetragonal symmetry of the system down to orthorhombic  $C_2$ . For  $g < -w$  and  $w < 0$ , the ground state is the so-called charge-spin density-wave (CSDW) [109], characterized by  $\Delta_X = \Delta_Y$  and  $\Delta_X \parallel \Delta_Y$ . This is a double- $\mathbf{Q}$  state that preserves the tetragonal symmetry of the system and displays a non-uniform magnetization in the Fe sites. Finally, for  $g < 0$  and  $w > 0$ , the magnetic configuration is a non-collinear one, called a spin-vortex crystal (SVC) [109], in which  $\Delta_X = \Delta_Y$  and  $\Delta_X \perp \Delta_Y$ . This is another double- $\mathbf{Q}$  state that preserves the tetragonal symmetry.

The Ginzburg-Landau coefficients  $u$ ,  $g$ , and  $w$  are expressed via fermionic propagators and depend on the band dispersions of the underlying fermionic model. The terms  $u$  and  $g$  are given by [86]:

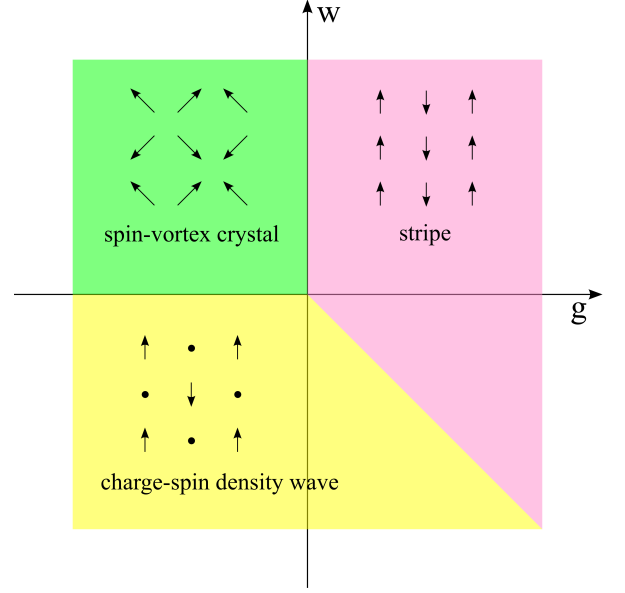


Figure 13. Phase diagram of the SDW free energy (31) displaying the double- $\mathbf{Q}$  spin-vortex crystal and charge-spin density-wave phases, as well as the stripe single- $\mathbf{Q}$  phase. Figure adapted from Ref. [110].

$$u = \frac{1}{2} \sum_n \int \frac{d^2\mathbf{k}}{(2\pi)^2} G_{h,\mathbf{k}}^2 (G_{e_X,\mathbf{k}} + G_{e_Y,\mathbf{k}})^2$$

$$g = -\frac{1}{2} \sum_n \int \frac{d^2\mathbf{k}}{(2\pi)^2} G_{h,\mathbf{k}}^2 (G_{e_X,\mathbf{k}} - G_{e_Y,\mathbf{k}})^2 \quad (32)$$

where  $G_{j,\mathbf{k}}^{-1} = i\omega_n - \varepsilon_{j,\mathbf{k}}$  is the free-fermion Green's function of band  $j$ . The coefficient  $w$  vanishes due to phase space and momentum conservation constraints.

For perfect nesting,  $g = 0$ , since  $G_{e_X,\mathbf{k}} = G_{e_Y,\mathbf{k}}$ . In this case, the magnetic ground state manifold has a larger  $O(6)$  symmetry, because only the combination  $(\Delta_X^2 + \Delta_Y^2)$  appears in the free energy. Small deviations from perfect nesting yield  $g > 0$ , which implies the existence of a single- $\mathbf{Q}$  stripe magnetic state, as observed experimentally. Stronger deviations from perfect nesting, however, may change the sign of  $g$  and promote a double- $\mathbf{Q}$  phase, as shown in Ref. [108]. Experimentally, tetragonal double- $\mathbf{Q}$  phases have been recently observed in hole-doped FeSC [70–72]. Note that, within this model,  $w = 0$  and the two types of double- $\mathbf{Q}$  phases are degenerate. To lift this degeneracy, one needs to include effects beyond those arising from the electronic structure. In particular, residual interactions in Eq. (25) that do not contribute to the SDW instability favor  $w > 0$  (and therefore a spin-vortex crystal) [85, 108] whereas coupling to disorder favors  $w < 0$  (and hence a charge-spin density-wave) [111]. Recent Mossbauer experiments have shown that, at least in some of the compounds where the double- $\mathbf{Q}$  phase has been reported, it is of the charge-spin density-wave

type [72].

### Ising-nematic order

The 3-band model also offers a suitable platform to study the onset of nematic order [19, 112–120], by which we mean the order which breaks  $C_4$  symmetry down to  $C_2$  but does not break spin-rotational symmetry. In the case where the magnetic ground state is the single- $\mathbf{Q}$  stripe one ( $g > 0$ ), the system actually has a doubly-degenerate ground state corresponding to either  $\Delta_Y = 0$  ( $\mathbf{Q}_X$  order) or  $\Delta_X = 0$  ( $\mathbf{Q}_Y$  order). In the former, the stripes are parallel to the  $y$  axis, whereas in the latter they are parallel to the  $x$  axis. Therefore, these two ground states are not related by an overall rotation of the spins, but rather by a  $90^\circ$  rotation. As a result, the ground state manifold in the  $g > 0$  case is  $O(3) \times Z_2$ , with  $O(3)$  referring to the spin-rotational symmetry and  $Z_2$  to the tetragonal symmetry of the system. In a mean-field approach both symmetries are broken simultaneously, but fluctuations in general suppress the continuous  $O(3)$  symmetry-breaking transition to lower temperatures than the discrete  $Z_2$  symmetry-breaking transition, particularly in anisotropic layered systems. As a result, there appears an intermediate phase where the  $Z_2$  symmetry is broken (i.e. the system is orthorhombic) but the  $O(3)$  symmetry is preserved (i.e. the system is paramagnetic). In other words, the stripe SDW phase melts in two stages, giving rise to an intermediate phase with  $O(3)$  symmetry restored but  $Z_2$  broken [7, 86, 121–126]. In analogy with liquid crystals, the stripe SDW phase can be viewed as a smectic phase and the intermediate  $Z_2$  phase as a nematic phase.

The spin-driven nematic order parameter  $\varphi$  (also often called Ising-nematic order parameter to underline that it breaks  $Z_2$  symmetry) is a composite operator made out of products of two SDW order parameters.

$$\varphi \propto \Delta_X^2 - \Delta_Y^2 \quad (33)$$

When the mean value of  $\varphi$  is non-zero, the tetragonal symmetry is broken, because magnetic fluctuations around  $\mathbf{Q}_X$  become larger or smaller than magnetic fluctuations around  $\mathbf{Q}_Y$ , as shown in Fig. 14.

The properties of the nematic phase can be obtained directly from the microscopically-derived free energy (31) by either computing the susceptibility for the  $\varphi$  field within RPA, or using bosonic RG or large- $N$ . We refer the interested reader to the relevant literature [7, 86, 122, 123, 127].

The calculation of the static nematic susceptibility within RPA yields [125]:

$$\chi_{\text{nem}} = \frac{\int_k \chi_{\text{SDW}}^2(k)}{1 - g \int_k \chi_{\text{SDW}}^2(k)} \quad (34)$$

where we introduced the notation  $k = (\omega_n, \mathbf{k})$ . To understand the meaning of this expression, consider that

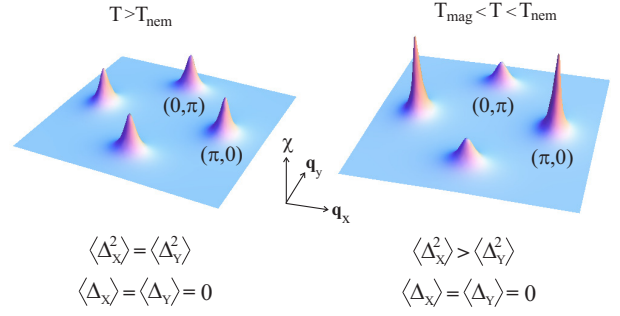


Figure 14. Schematic representation of the nematic phase promoted by the partial melting of the stripe SDW state. Below the nematic transition temperature  $T_{\text{nem}}$  but above the magnetic transition temperature  $T_{\text{mag}}$ , the inelastic magnetic peaks become different around  $\mathbf{Q}_X = (\pi, 0)$  and  $\mathbf{Q}_Y = (0, \pi)$ . Figure adapted from Ref. [86].

the system is approaching an SDW transition from high temperatures. At the SDW transition, the quantity  $\int_k \chi_{\text{SDW}}^2(k)$  must diverge. However, before it diverges, it will reach the value  $1/g$ , no matter how small  $g$  is, as long as  $g > 0$ . Thus,  $\chi_{\text{nem}} \rightarrow \infty$  before  $\chi_{\text{SDW}} \rightarrow \infty$ . The close relationship between these two transitions is evident: if the magnetic transition temperature is suppressed, then  $\int_k \chi_{\text{SDW}}^2(k)$  will only reach the value  $1/g$  at a lower temperature. Because of this, the nematic transition line follows the magnetic transition line, in agreement with the experimental phase diagrams of most FeSC (except for FeSe, see next section).

Note that in more sophisticated RG or large- $N$  approaches, the nematic transition is not always a second order transition. It can be first-order, with a jump in  $\varphi$  from zero to a finite value. Furthermore, in some cases the jump in  $\varphi$  triggers the magnetic order, giving rise to a simultaneous first-order magnetic-nematic transition (see Ref. [86] for details).

As for the interplay between superconductivity and SDW, the 3-band model reveals a new ingredient absent in the 2-band model. Similarly to the 2-band model (see Eq. (30)), we can derive from the microscopic model the Ginzburg-Landau free energy for the magnetic ( $\Delta_X$ ,  $\Delta_Y$ ) and SC ( $\Delta_{s+-}$ ,  $\Delta_{s++}$ ,  $\Delta_d$ ) order parameters. The competition between SDW and superconductivity is still present, as the biquadratic couplings  $\Delta_{s+-}^2 - \Delta_{X/Y}^2$  have positive coefficients. But besides this, a new coupling appears in the free energy [95, 128]:

$$\tilde{F} = \lambda (\Delta_{s+-}^* - \Delta_d + \Delta_{s+-} - \Delta_d^*) (\Delta_X^2 - \Delta_Y^2) \quad (35)$$

This term can be interpreted as a trilinear coupling between the  $s^{+-}$  and  $d$ -wave SC order parameters and the nematic order parameter. The consequences of this term are interesting: an obvious one is that long-range nematic order leads to an admixture of the  $s^{+-}$  and  $d$ -wave gaps. This is not unexpected, since in the orthorhombic

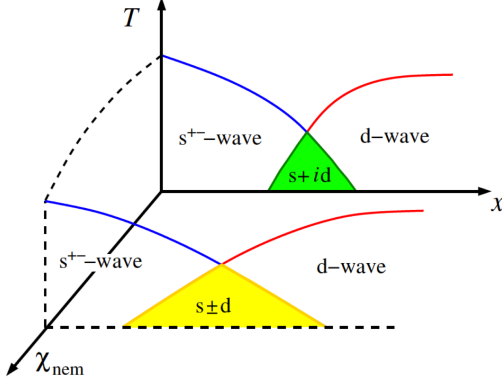


Figure 15. Interplay between  $d$ -wave and  $s^{+-}$ -wave superconductivity as function of the intensity of nematic fluctuations ( $\chi_{\text{nem}}$ ): for weak nematic fluctuations, the coexistence state  $s \pm id$  breaks time-reversal symmetry, whereas for moderate fluctuations, the coexistence state  $s \pm d$  breaks tetragonal symmetry.

phase these two gaps no longer belong to different irreducible representations. What is more interesting is that  $T_c$  can actually increase in the presence of nematic order, because the pairing frustration between  $s^{+-}$  or  $d$ -wave is lifted by long-range nematic order [95, 129]. This is particularly relevant when  $s^{+-}$  and  $d$ -wave channels are nearly degenerate [12, 130]. Analogously, if the system condenses in a single- $\mathbf{Q}$  stripe phase, the suppression of  $T_c$  due to the competition between SDW and superconductivity may be alleviated by this effect. This is to be contrasted with the case of a double- $\mathbf{Q}$  phase, in which  $\Delta_X^2 = \Delta_Y^2$ , and the term (35) does not contribute to an energy gain [131].

Even in the tetragonal phase, where there is no long-range nematic order, the trilinear coupling (35) can become important – as long as the  $s^{+-}$  and  $d$ -wave SC states have comparable energies and nematic fluctuations are strong. After integrating out nematic fluctuations, we find that nematic fluctuations promote an effective attraction between the  $s^{+-}$  and  $d$ -wave channels. As a result, an exotic nematic-SC state  $s \pm d$  that spontaneously breaks tetragonal symmetry can be stabilized [95, 132] instead of the  $s \pm id$  state that would appear in the absence of nematic fluctuations [133], see Fig. 15.

To summarize, the analysis of the 2-band and 3-band models reveal that, despite their simplicity, they offer deep insights into the rich physics of the FeSC, particularly the interplay between SDW and SC orders, the selection of SDW order by fluctuations, and vestigial Ising-nematic order. The main drawback of the band models is the neglect of orbital degrees of freedom, e.g. band models cannot describe the phenomena associated with spontaneous orbital order. They also cannot detect specific orbital-induced features in the SDW and SC phases, such as nodal SDW and orbital anti-phase pairing state.

#### IV. ORBITAL-PROJECTED BAND MODELS

We now discuss recent works that aim to capture the low-energy physics of FeSC by focusing on band excitations near the Fermi surface, while fully keeping the orbital content of these excitations [49, 55, 97]. The inputs for this approach are the Fermi surface geometry (the location of the Fermi surfaces near  $\Gamma$ ,  $X$ ,  $Y$ , and  $M$  points in the 1-Fe BZ) and the fact that the excitations near the Fermi surfaces are composed predominantly of three orbitals –  $d_{xz}$ ,  $d_{yz}$ , and  $d_{xy}$ . The electronic states near each pocket are treated as separate excitations, as in the band-basis approach of the previous section. However, the interactions between the low-energy electronic states are not treated phenomenologically. Instead, they are obtained directly from the underlying orbital model and contain information about the orbital composition of the low-energy states via the orbital-band matrix elements from Eq (3).

As discussed above, with the  $d_{xz}$ ,  $d_{yz}$ , and  $d_{xy}$  orbitals, one can successfully describe the low-energy sector of the electronic dispersion, but one cannot describe the dispersions over the whole BZ. Accordingly, the restriction to states near the Fermi pockets is justified if the excitations with momenta far from the high-symmetry points of the BZ have high enough energy and do not contribute to the low-energy physics. This generally requires all Fermi pockets to be small and all excitations at, say, half the distance between different pockets, to be high in energy. The first condition is satisfied in most FeSC, particularly the ones with only two hole and two electron pockets. The second condition needs to be verified for each specific material as some bands remain rather flat between the  $\Gamma$ -centered hole pockets and the  $X$ - and  $Y$ -centered electron pockets.

In the discussion below we assume that the conditions for the separation into low-energy states near the pockets and high-energy states between the pockets are met and analyze how the orbital content of the excitations affects the hierarchy of instabilities towards SC, density-wave, and orbital orders.

##### A. Non-interacting Hamiltonian

There are different ways to construct low-energy excitations near the Fermi pockets. One way is to exploit the properties of the  $P4/nmm$  space group of a single FeAs layer and construct the minimal model using the Luttinger's method of invariants [49]. The free parameters of the non-interacting part of the model can then be extracted from the fit to first-principle calculations. Another way is to start directly from the five-orbital model of Eq. (5)

$$\mathcal{H}_0 = \sum_{\mu\nu} [\epsilon_{\mu\nu} - \bar{\mu}\delta_{\mu\nu}](\mathbf{k}) d_{\mathbf{k}\mu\sigma}^\dagger d_{\mathbf{k}\nu\sigma} \quad (36)$$

where  $\epsilon_{\mu\nu}(\mathbf{k})$  is the  $5 \times 5$  dispersion matrix, and restrict  $\epsilon_{\mu\nu}(\mathbf{k})$  to the subspace of  $d_{xz}$ ,  $d_{yz}$ , and  $d_{xy}$  orbitals that dominate the low-energy states near the desired high-symmetry point [55, 97]. Expanding near each high-symmetry point and diagonalizing the quadratic Hamiltonian, one obtains the dispersion of low-energy excitations in the band basis. In this case, the band dispersion parameters are given in terms of the original tight-binding parameters of the orbital model. The drawback of this procedure is that the actual low-energy dispersions, extracted from ARPES experiments, generally differ from the ones obtained from the truncated tight-binding model due to interaction-driven renormalizations involving high-energy states [96, 134]. According to ARPES, such renormalizations change the hopping parameters by orbital-dependent numerical factors, which range between one and three in most of FeSC, but can be as high as seven [135]. In other words, to obtain the actual low-energy dispersion from the underlying  $5 \times 5$  orbital model, one has to integrate out high-energy states (including the ones from the other orbitals) rather than just neglect them. It is therefore more convenient to fit the expansion parameters to the experiments rather than to first-principle calculations.

We start by considering the region near the  $\Gamma$  point. As shown previously in Fig. 4, the spectral weight of the low-energy states arises mainly from the  $d_{xz}$  and  $d_{yz}$  orbitals. In the absence of spin-orbit coupling, these two orbitals are degenerate at the  $\Gamma$  point, i.e.,  $\epsilon_{xz,xz}(k=0) = \epsilon_{yz,yz}(k=0)$  and  $\epsilon_{xz,yz}(k=0) = 0$ . The degeneracy is exact and stems from the fact that in group theoretical language  $d_{xz}$  and  $d_{yz}$  states form the two-dimensional  $E_g$  irreducible representation of the  $D_{4h}$  group. Introducing the spinor

$$\psi_{\Gamma,\mathbf{k}} = \begin{pmatrix} d_{yz,\mathbf{k}\sigma} \\ -d_{xz,\mathbf{k}\sigma} \end{pmatrix} \quad (37)$$

one can write the kinetic energy part of the Hamiltonian as

$$\mathcal{H}_{0,\Gamma} = \sum_{\mathbf{k}} \psi_{\Gamma,\mathbf{k}}^\dagger h_{\Gamma}(\mathbf{k}) \psi_{\Gamma,\mathbf{k}} \quad (38)$$

To obtain the elements of the  $2 \times 2$  matrix  $h_{\Gamma}(\mathbf{k})$  one can either expand the  $2 \times 2$  matrix  $\epsilon_{\mu\nu}(\mathbf{k})$  for small  $\mathbf{k}$  (with  $\mu, \nu = d_{xz}, d_{yz}$ ) or write down all the trigonometric invariants that satisfy the symmetry property that one orbital transforms into the other under a rotation by  $\pi/2$ . In both cases, we obtain [49, 55]

$$h_{\Gamma}(\mathbf{k}) = \begin{pmatrix} \epsilon_{\Gamma} + \frac{k^2}{2m_{\Gamma}} + bk^2 \cos 2\theta & ck^2 \sin 2\theta \\ ck^2 \sin 2\theta & \epsilon_{\Gamma} + \frac{k^2}{2m_{\Gamma}} - bk^2 \cos 2\theta \end{pmatrix} \otimes \sigma^0 \quad (39)$$

where the Pauli matrix  $\sigma^0$  refers to the spin space and the angle  $\theta$  is measured with respect to the  $k_x$  axis. The

parameters  $\epsilon_{\Gamma}$ ,  $m_{\Gamma}$ ,  $b$ , and  $c$  could be related to the tight-binding parameters of  $\epsilon_{\mu\nu}(\mathbf{k})$ . However, due to the reasons discussed above, they should better be understood as input parameters that can be obtained from fits to ARPES data. The Hamiltonian is diagonalized by transforming to hole-band operators  $c_{h_1,\mathbf{k}\sigma}$  and  $c_{h_2,\mathbf{k}\sigma}$  via the rotation

$$\begin{aligned} c_{h_1,\mathbf{k}\sigma} &= \cos \theta_{\mathbf{k}} d_{xz,\mathbf{k}\sigma} - \sin \theta_{\mathbf{k}} d_{yz,\mathbf{k}\sigma} \\ c_{h_2,\mathbf{k}\sigma} &= \cos \theta_{\mathbf{k}} d_{yz,\mathbf{k}\sigma} + \sin \theta_{\mathbf{k}} d_{xz,\mathbf{k}\sigma} \end{aligned} \quad (40)$$

The Hamiltonian in the band basis is:

$$\mathcal{H}_{0,\Gamma} = \sum_{i=1,2} \sum_{\mathbf{k}\sigma} \epsilon_{h_i}(\mathbf{k}) c_{h_i,\mathbf{k}\sigma}^\dagger c_{h_i,\mathbf{k}\sigma} \quad (41)$$

where

$$\epsilon_{h_{1,2}}(\mathbf{k}) = \epsilon_{\Gamma} + \frac{k^2}{2m_{\Gamma}} \mp k^2 \sqrt{b^2 \cos^2 \theta + c^2 \sin^2 \theta} \quad (42)$$

The angle  $\theta_{\mathbf{k}}$  is related to the polar angle  $\theta$  by:

$$\tan 2\theta_{\mathbf{k}} = \frac{c}{b} \tan 2\theta \quad (43)$$

The two angles satisfy a simple relationship when  $c^2 = b^2$ . Then  $\theta_{\mathbf{k}} = -\text{sign}(c) \theta$  if  $b < 0$  and  $\theta_{\mathbf{k}} = \text{sign}(c) \theta + \frac{\pi}{2}$  if  $b > 0$ . In either case, the condition  $c^2 = b^2$  implies that the dispersions  $\epsilon_{h_{1,2}}(\mathbf{k})$  are isotropic, i.e. the two hole Fermi surfaces are circles of different radii:

$$\epsilon_{h_{1,2}}(\mathbf{k}) = \epsilon_{\Gamma} + \frac{k^2}{2m_{1,2}} \quad (44)$$

with:

$$m_{1,2} = \frac{m_{\Gamma}}{1 \mp 2|c|/m_{\Gamma}} \quad (45)$$

Consider now the momentum range near the  $X$  pocket. The low-energy orbital excitations in this region are composed out of  $d_{yz}$  and  $d_{xy}$  orbitals (see Fig. 4 above). By this reason, we can restrict the analysis to the  $2 \times 2$  subspace spanned by the  $d_{yz}$  and  $d_{xy}$  orbitals and express the kinetic energy in the orbital space in terms of a spinor

$$\psi_{X,\mathbf{k}} = \begin{pmatrix} d_{yz,\mathbf{k}+\mathbf{Q}_X\sigma} \\ d_{xy,\mathbf{k}+\mathbf{Q}_X\sigma} \end{pmatrix} \quad (46)$$

as

$$\mathcal{H}_{0,X} = \sum_{\mathbf{k}} \psi_{X,\mathbf{k}}^\dagger h_X(\mathbf{k}) \psi_{X,\mathbf{k}} \quad (47)$$

Note that  $\mathbf{k}$  in  $h_X(\mathbf{k})$  is measured relative to  $\mathbf{Q}_X$ . The elements of the matrix  $h_X(\mathbf{k})$  obey certain symmetry conditions, which can also be obtained by expanding the  $2 \times 2$  matrix  $\epsilon_{\mu\nu}(\mathbf{k})$  for small  $\mathbf{k} + \mathbf{Q}_X$  (with  $\mu, \nu = d_{yz}, d_{xy}$ ) [49, 55]:

$$h_X(\mathbf{k}) = \begin{pmatrix} \epsilon_1 + \frac{k^2}{2m_1} - a_1 k^2 \cos 2\theta & -2ivk \sin \theta \\ 2ivk \sin \theta & \epsilon_3 + \frac{k^2}{2m_3} - a_3 k^2 \cos 2\theta \end{pmatrix} \otimes \sigma^0 \quad (48)$$

Because the non-diagonal terms in  $h_X(\mathbf{k})$  are imaginary, the transformation to band operators involves complex factors

$$\begin{aligned} c_{e_{X1}, \mathbf{k} + \mathbf{Q}_X \sigma} &= \cos \theta_{\mathbf{k}} d_{yz, \mathbf{k} + \mathbf{Q}_X \sigma} - i \sin \theta_{\mathbf{k}} d_{xy, \mathbf{k} + \mathbf{Q}_X \sigma} \\ c_{e_{X2}, \mathbf{k} + \mathbf{Q}_X \sigma} &= \cos \theta_{\mathbf{k}} d_{xy, \mathbf{k} + \mathbf{Q}_X \sigma} - i \sin \theta_{\mathbf{k}} d_{yz, \mathbf{k} + \mathbf{Q}_X \sigma}. \end{aligned} \quad (49)$$

The diagonal Hamiltonian in the band basis is

$$\mathcal{H}_{0,X} = \sum_{\mathbf{k}\sigma i} \varepsilon_{e_{Xi}}(\mathbf{k} + \mathbf{Q}_X) c_{e_{Xi}, \mathbf{k} + \mathbf{Q}_X \sigma}^\dagger c_{e_{Xi}, \mathbf{k} + \mathbf{Q}_X \sigma} \quad (50)$$

where

$$\begin{aligned} \varepsilon_{e_{X1,X2}}(\mathbf{k} + \mathbf{Q}_X) &= \frac{A_1 + A_3}{2} \\ &\pm \sqrt{\left(\frac{A_1 - A_3}{2}\right)^2 + 4k^2 v^2 \sin^2 \theta} \end{aligned} \quad (51)$$

Here,  $A_1 = \epsilon_1 + k^2/(2m_1) - a_1 k^2 \cos 2\theta$  and  $A_3 = \epsilon_3 + k^2/(2m_3) - a_3 k^2 \cos 2\theta$  are the diagonal elements of the matrix  $h_X(\mathbf{k})$ . The angle  $\theta_{\mathbf{k} + \mathbf{Q}_X}$  is related to the polar angle  $\theta$  by

$$\tan 2\theta_{\mathbf{k} + \mathbf{Q}_X} = \frac{4vk \sin 2\theta}{A_1 - A_3} \quad (52)$$

Out of the two dispersions in (51), only one crosses the Fermi level. Let us first consider the angles  $\theta = 0, \pi$ , for which the hybridization between the  $d_{xy}$  and  $d_{yz}$  orbitals vanishes. ARPES measurements show that at  $k = 0$  (i.e. at the  $X$  point) both  $A_1$  and  $A_3$  are negative and the  $d_{xy}$  orbital has a lower energy, i.e.  $A_3 < A_1$  [136, 137]. However, for  $k = k_F$ , the band that crosses the Fermi level has a pure  $d_{xy}$  character. As a result,  $A_3 < A_1$  for  $k = 0$  and  $A_3 > A_1$  for  $k = k_F$  and  $\theta = 0, \pi$ . Consequently, the band that crosses the Fermi level at these angles must be  $\varepsilon_{e_{X1}}(\mathbf{k}) = \left(\frac{A_1 + A_3}{2}\right) + \left|\frac{A_1 - A_3}{2}\right|$ , which interpolates between pure  $d_{yz}$  character at  $k = 0$  ( $A_3 < A_1$ ) and pure  $d_{xy}$  character at  $k = k_F$  ( $A_3 > A_1$ ).

For any other value of  $\theta$ , the  $d_{yz}$  and  $d_{xy}$  orbital dispersions become hybridized. By continuity, the dispersion which crosses the Fermi level must be  $\varepsilon_{e_{X1}}(\mathbf{k})$ . Hereafter, we drop the subscript and denote this dispersion by  $\varepsilon_{e_X}(\mathbf{k})$  and the corresponding band operator by  $c_{e_X, \mathbf{k} + \mathbf{Q}_X \sigma}$ . The second dispersion  $\varepsilon_{e_{X2}}(\mathbf{k})$  does not cross the Fermi level and we assume that it does not belong to the low-energy sector.

Similarly, for the electron pocket at  $Y$  we consider the  $2 \times 2$  subspace spanned by the  $d_{xz}$  and  $d_{xy}$  orbitals, define the spinor:

$$\psi_{Y, \mathbf{k}} = \begin{pmatrix} d_{xz, \mathbf{k} + \mathbf{Q}_Y \sigma} \\ d_{xy, \mathbf{k} + \mathbf{Q}_Y \sigma} \end{pmatrix} \quad (53)$$

and write the kinetic energy as

$$\mathcal{H}_{0,Y} = \sum_{\mathbf{k}} \psi_{Y, \mathbf{k}}^\dagger h_Y(\mathbf{k}) \psi_{Y, \mathbf{k}} \quad (54)$$

with

$$h_Y(\mathbf{k}) = \begin{pmatrix} \epsilon_1 + \frac{k^2}{2m_1} + a_1 k^2 \cos 2\theta & -2ivk \cos \theta \\ 2ivk \cos \theta & \epsilon_3 + \frac{k^2}{2m_3} + a_3 k^2 \cos 2\theta \end{pmatrix} \otimes \sigma^0 \quad (55)$$

The dispersion that crosses the Fermi level is

$$\varepsilon_{e_Y}(\mathbf{k} + \mathbf{Q}_Y) = \varepsilon_{e_{Y1}}(\mathbf{k} + \mathbf{Q}_Y) = \frac{\bar{A}_1 + \bar{A}_3}{2} + \sqrt{\left(\frac{\bar{A}_1 - \bar{A}_3}{2}\right)^2 + 4k^2 v^2 \cos^2 \theta}. \quad (56)$$

where  $\bar{A}_1 = \epsilon_1 + k^2/(2m_1) + a_1 k^2 \cos 2\theta$  and  $\bar{A}_3 = \epsilon_3 + k^2/(2m_3) + a_3 k^2 \cos 2\theta$  are diagonal components of  $h_Y(\mathbf{k})$ . We label the corresponding band operator as  $c_{e_Y, \mathbf{k} + \mathbf{Q}_Y \sigma}$ .

Combining Eqs. (38), (47), and (54), we obtain the the free-fermion part of the low-energy Hamiltonian:

$$\mathcal{H}_0 = \sum_{\mathbf{k}} \Psi_{\mathbf{k}}^\dagger [\hat{H}_0(\mathbf{k}) - \mu \hat{1}] \Psi_{\mathbf{k}} \quad (57)$$

where  $\Psi_{\mathbf{k}}$  is the enlarged spinor

$$\Psi_{\mathbf{k}} = \begin{pmatrix} \psi_{Y, \mathbf{k}} \\ \psi_{X, \mathbf{k}} \\ \psi_{\Gamma, \mathbf{k}} \end{pmatrix} \quad (58)$$

and the Hamiltonian in the matrix form is

$$\hat{H}_0(\mathbf{k}) = \begin{pmatrix} h_Y(\mathbf{k}) & 0 & 0 \\ 0 & h_X(\mathbf{k}) & 0 \\ 0 & 0 & h_\Gamma(\mathbf{k}) \end{pmatrix} \quad (59)$$

Fig. 16 shows the resulting Fermi surfaces from this model. For this figure, the input parameters were obtained from the fit to first-principle calculations [49] (see Table IV in Appendix A; higher-order off-diagonal terms have been included to yield a better looking Fermi surface). As discussed above, alternatively one can treat  $\epsilon_\Gamma$ ,  $\epsilon_1$ ,  $\epsilon_3$ ,  $m_\Gamma$ ,  $m_1$ ,  $m_3$ ,  $a_1$ ,  $a_3$ ,  $b$ ,  $c$ , and  $v$  as input parameters and obtain them from fits to ARPES data. The advantage of this last procedure is that it deals with the actual measured dispersion and hence includes all regular renormalizations from high-energy fermions, which shrink and move the bands [34, 50, 96]. Note also that although the number of input parameters (11 total) is not small, it is still much smaller than the number of input parameters for the full-fledged five-orbital model from Sec. II A 1

We emphasize that the model presented here is not equivalent to the 3-orbital model which we considered in Sec. II. To be more precise, the 3-orbital model considered here describes the low-energy sector of the lattice model made out of  $d_{xz}$ ,  $d_{yz}$ , and  $d_{xy}$  orbitals near points  $\Gamma$ ,  $X$ , and  $Y$ . We remind that the 3-orbital lattice model has additional Fermi surfaces, not observed in the experiments. In the present analysis we take as an input the fact that additional Fermi surfaces are eliminated by the

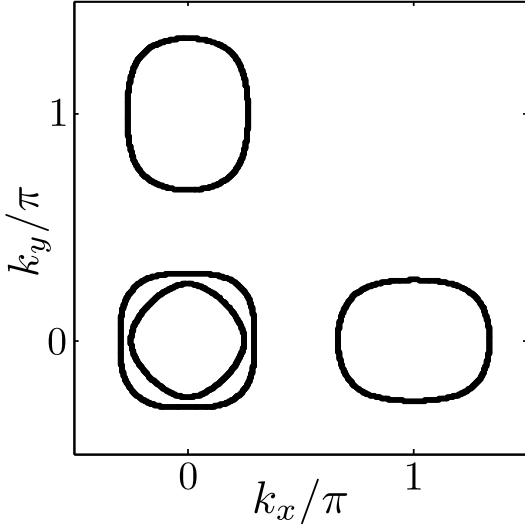


Figure 16. Fermi surface of the orbital-projected band model in the 1-Fe Brillouin zone.

hybridization between the  $t_{2g}$  and  $e_g$  subsets, and focus on the experimentally-observed Fermi surface geometry.

If the Fermi surface geometry is such that there exists an additional hole pocket at the  $M$  point, the analysis can be straightforwardly extended to include it. Because this pocket is made out of the  $d_{xy}$  orbital, we just introduce an additional operator  $\psi_{M,\mathbf{k}} \equiv d_{xy,\mathbf{k}+\mathbf{Q}_X+\mathbf{Q}_Y\sigma}$  and write an additional kinetic energy term:

$$\mathcal{H}_{0,M} = \sum_{\mathbf{k}} \psi_{M,\mathbf{k}}^\dagger h_M(\mathbf{k}) \psi_{M,\mathbf{k}} \quad (60)$$

with

$$h_M(\mathbf{k}) = \epsilon_M + \frac{k^2}{2m_M} - b_M k^4 \sin^2 2\theta \quad (61)$$

With this extra term, the free-fermion Hamiltonian describes all five Fermi pockets in terms of three distinct orbital states.

## B. Order parameters

The order parameters can be defined either in the orbital or in the band basis, similarly to how it was done in the previous two sections. The difference with respect to the purely orbital models is that now the momenta are confined to the vicinity of the  $\Gamma$ ,  $X$ ,  $Y$ , and  $M$  points. Consequently, some order parameters that seem different when viewed in the full BZ become indistinguishable (see below). Conversely, the difference with respect to the purely band models is that now the order parameters do depend on the angles along the Fermi pockets due to variation of the orbital content of the low-energy excitations. The order parameters can be straightforwardly converted from one basis to the other using the

transformations from Eqs. (40) and (49). The full list of potential order parameters is rather long, and for brevity we list below only the order parameters composed of combinations of  $d_{xz}$  and  $d_{yz}$  orbitals.

### 1. SDW and CDW orders

There are four possible order parameters describing SDW order with momenta  $\mathbf{Q}_X$  and  $\mathbf{Q}_Y$  [97]:

$$\begin{aligned} \Delta_{\text{SDW},Y}(\mathbf{k}) &= d_{xz,\mathbf{k}+\mathbf{Q}_Y\alpha}^\dagger \sigma_{\alpha\beta} d_{xz,\mathbf{k}\beta} + h.c. \\ \Delta_{\text{SDW},X}(\mathbf{k}) &= d_{yz,\mathbf{k}+\mathbf{Q}_X\alpha}^\dagger \sigma_{\alpha\beta} d_{yz,\mathbf{k}\beta} + h.c. \\ \bar{\Delta}_{\text{iSDW},Y}(\mathbf{k}) &= i d_{xz,\mathbf{k}+\mathbf{Q}_Y\sigma}^\dagger \sigma_{\alpha\beta} d_{xz,\mathbf{k}\beta} + h.c. \\ \bar{\Delta}_{\text{iSDW},X}(\mathbf{k}) &= i d_{yz,\mathbf{k}+\mathbf{Q}_X\sigma}^\dagger \sigma_{\alpha\beta} d_{yz,\mathbf{k}\beta} + h.c. \end{aligned} \quad (62)$$

The momentum  $\mathbf{k}$  is assumed to be small, what implies that the relevant electronic states are near the  $\Gamma$  and the  $X$  or  $Y$  points. These order parameters are diagonal in the orbital index, and correspond to real SDW or imaginary SDW (i.e. spin-current density-wave). In addition, there are four possible orbital off-diagonal SDW order parameters:

$$\begin{aligned} \bar{\Delta}_{\text{SDW},Y}(\mathbf{k}) &= d_{xz,\mathbf{k}+\mathbf{Q}_Y\alpha}^\dagger \sigma_{\alpha\beta} d_{yz,\mathbf{k}\beta} + h.c. \\ \bar{\Delta}_{\text{SDW},X}(\mathbf{k}) &= d_{yz,\mathbf{k}+\mathbf{Q}_X\alpha}^\dagger \sigma_{\alpha\beta} d_{xz,\mathbf{k}\beta} + h.c. \\ \bar{\Delta}_{\text{iSDW},Y}(\mathbf{k}) &= i d_{xz,\mathbf{k}+\mathbf{Q}_Y\alpha}^\dagger \sigma_{\alpha\beta} d_{yz,\mathbf{k}\beta} + h.c. \\ \bar{\Delta}_{\text{iSDW},X}(\mathbf{k}) &= i d_{yz,\mathbf{k}+\mathbf{Q}_X\alpha}^\dagger \sigma_{\alpha\beta} d_{xz,\mathbf{k}\beta} + h.c. \end{aligned} \quad (63)$$

In the band basis, these order parameters are bilinear combinations of  $c_{h,\mathbf{k}\sigma}$  and  $c_{e_X,\mathbf{k}+\mathbf{Q}_X\sigma}$  or  $c_{h,\mathbf{k}\sigma}$  and  $c_{e_Y,\mathbf{k}+\mathbf{Q}_Y\sigma}$ . Below we consider the effects of interactions for the simplified model with electron pockets consisting entirely of  $d_{xz}$  and  $d_{yz}$  orbitals. For this model, we obtain in the band basis:

$$\begin{aligned} \Delta_{\text{SDW},Y/X}(\mathbf{k}) &= c_{h_{1/2},\mathbf{k}\alpha}^\dagger \sigma_{\alpha\beta} c_{e_{Y/X},\mathbf{k}+\mathbf{Q}_{Y/X}\beta} \cos \theta \\ &\quad \pm c_{h_{2/1},\mathbf{k}\alpha}^\dagger \sigma_{\alpha\beta} c_{e_{Y/X},\mathbf{k}+\mathbf{Q}_{Y/X}\beta} \sin \theta + h.c. \\ \bar{\Delta}_{\text{SDW},Y/X}(\mathbf{k}) &= c_{h_{2/1},\mathbf{k}\alpha}^\dagger \sigma_{\alpha\beta} c_{e_{Y/X},\mathbf{k}+\mathbf{Q}_{Y/X}\beta} \cos \theta \\ &\quad \mp c_{h_{1/2},\mathbf{k}\alpha}^\dagger \sigma_{\alpha\beta} c_{e_{Y/X},\mathbf{k}+\mathbf{Q}_{Y/X}\beta} \sin \theta + h.c. \end{aligned} \quad (64)$$

where the upper sign is for  $Y$  and the lower for  $X$ . The expressions for the imaginary SDW order parameters are analogous. CDW order parameters can be constructed by just replacing  $\sigma_{\alpha\beta} \rightarrow \delta_{\alpha\beta}$  in the expressions above.

### 2. SC order

We consider only spin-singlet pairing. There are four possible pairing channels with non-zero order parameters:  $A_{1g}$ ,  $B_{1g}$ ,  $B_{2g}$ , and  $A_{2g}$ . The order parameter in the

$A_{2g}$  channel vanishes under simultaneous interchange of orbital indices and spin projections. The  $A_{1g}$ ,  $B_{1g}$ , and  $B_{2g}$  order parameters in the orbital basis are [97]:

$$\begin{aligned}\Delta_e^{A_1} &= d_{xz,\mathbf{k}+\mathbf{Q}_Y\uparrow}d_{xz,-\mathbf{k}-\mathbf{Q}_Y\downarrow} + d_{yz,\mathbf{k}+\mathbf{Q}_X\uparrow}d_{yz,-\mathbf{k}-\mathbf{Q}_X\downarrow} \\ \Delta_h^{A_1} &= d_{xz,\mathbf{k}\uparrow}d_{xz,-\mathbf{k}\downarrow} + d_{yz,\mathbf{k}\uparrow}d_{yz,-\mathbf{k}\downarrow} \\ \Delta_e^{B_1} &= d_{xz,\mathbf{k}+\mathbf{Q}_Y\uparrow}d_{xz,-\mathbf{k}-\mathbf{Q}_Y\downarrow} - d_{yz,\mathbf{k}+\mathbf{Q}_X\uparrow}d_{yz,-\mathbf{k}-\mathbf{Q}_X\downarrow} \\ \Delta_h^{B_1} &= d_{xz,\mathbf{k}\uparrow}d_{xz,-\mathbf{k}\downarrow} - d_{yz,\mathbf{k}\uparrow}d_{yz,-\mathbf{k}\downarrow} \\ \Delta_e^{B_2} &= 0 \\ \Delta_h^{B_2} &= d_{xz,\mathbf{k}\uparrow}d_{yz,-\mathbf{k}\downarrow} + d_{yz,\mathbf{k}\uparrow}d_{xz,-\mathbf{k}\downarrow}\end{aligned}\quad (65)$$

In the band basis, these order parameters become:

$$\begin{aligned}\Delta_e^{A_1} &= c_{eY,\mathbf{k}+\mathbf{Q}_Y\uparrow}c_{eY,-\mathbf{k}-\mathbf{Q}_Y\downarrow} + c_{eX,\mathbf{k}+\mathbf{Q}_X\uparrow}c_{eX,-\mathbf{k}-\mathbf{Q}_X\downarrow} \\ \Delta_h^{A_1} &= c_{h1,\mathbf{k}\uparrow}c_{h1,-\mathbf{k}\downarrow} + c_{h2,\mathbf{k}\uparrow}c_{h2,-\mathbf{k}\downarrow} \\ \Delta_e^{B_1} &= c_{eY,\mathbf{k}+\mathbf{Q}_Y\uparrow}c_{eY,-\mathbf{k}-\mathbf{Q}_Y\downarrow} - c_{eX,\mathbf{k}+\mathbf{Q}_X\uparrow}c_{eX,-\mathbf{k}-\mathbf{Q}_X\downarrow} \\ \Delta_h^{B_1} &= (c_{h1,\mathbf{k}\uparrow}c_{h1,-\mathbf{k}\downarrow} - c_{h2,\mathbf{k}\uparrow}c_{h2,-\mathbf{k}\downarrow}) \cos 2\theta \\ &\quad + (c_{h1,\mathbf{k}\uparrow}c_{h2,-\mathbf{k}\downarrow} - c_{h2,\mathbf{k}\uparrow}c_{h1,-\mathbf{k}\downarrow}) \sin 2\theta \\ \Delta_e^{B_2} &= 0 \\ \Delta_h^{B_2} &= (c_{h2,\mathbf{k}\uparrow}c_{h2,-\mathbf{k}\downarrow} - c_{h1,\mathbf{k}\uparrow}c_{h1,-\mathbf{k}\downarrow}) \sin 2\theta \\ &\quad + (c_{h1,\mathbf{k}\uparrow}c_{h2,-\mathbf{k}\downarrow} + c_{h2,\mathbf{k}\uparrow}c_{h1,-\mathbf{k}\downarrow}) \cos 2\theta\end{aligned}\quad (66)$$

For non-circular hole pockets, there are additional order parameters in each representation. They have the same structure as the ones above, but contain additional powers of  $C_4$ -symmetric factors  $\cos 4\theta$  either on the hole or on the electron pockets. When the  $d_{xy}$  orbital content on the two electron pockets is included, certain gaps acquire additional contributions that depend on the angle along the electron pockets as  $\cos(4n+2)\theta$ . These additional terms, when large enough, give rise to the emergence of accidental nodes in an  $s$ -wave gap [81, 138].

### 3. $\mathbf{Q} = 0$ orbital order

As discussed in Sec. II, the order parameters with zero momentum transfer in the particle-hole charge channel are

$$\Delta_{\text{POM},\mu\mu'} = d_{\mu\sigma}^\dagger d_{\mu'\sigma} \quad (67)$$

where  $\mu, \mu' = xz, yz$  and the summation over spin indices is assumed. We label the corresponding combinations near the hole and the electron pockets as  $\Delta_{\mu\mu'}^e$  and  $\Delta_{\mu\mu'}^h$ . The bilinear combinations, which are even under inversion, can be classified by irreducible representations of the  $D_{4h}$  group. The most relevant ones for comparison with experiments are in the  $A_{1g}$  and  $B_{1g}$  channels [97]:

$$\begin{aligned}\Delta_{\text{POM},A_{1g}/B_{1g}}^e &= d_{xz,\mathbf{k}+\mathbf{Q}_Y\sigma}^\dagger d_{xz,\mathbf{k}+\mathbf{Q}_Y\sigma} \\ &\quad \pm d_{yz,\mathbf{k}+\mathbf{Q}_X\sigma}^\dagger d_{yz,\mathbf{k}+\mathbf{Q}_X\sigma} \\ \Delta_{\text{POM},A_{1g}/B_{1g}}^h &= d_{xz,\mathbf{k}\sigma}^\dagger d_{xz,\mathbf{k}\sigma} \pm d_{yz,\mathbf{k}\sigma}^\dagger d_{yz,\mathbf{k}\sigma}\end{aligned}\quad (68)$$

In the band basis, they become

$$\begin{aligned}\Delta_{\text{POM},A_{1g}}^e &= c_{eY,\mathbf{k}+\mathbf{Q}_Y\sigma}^\dagger c_{eY,\mathbf{k}+\mathbf{Q}_Y\sigma} + c_{eX,\mathbf{k}+\mathbf{Q}_X\sigma}^\dagger c_{eX,\mathbf{k}+\mathbf{Q}_X\sigma} \\ \Delta_{\text{POM},A_{1g}}^h &= c_{h1,\mathbf{k}\sigma}^\dagger c_{h1,\mathbf{k}\sigma} + c_{h2,\mathbf{k}\sigma}^\dagger c_{h2,\mathbf{k}\sigma} \\ \Delta_{\text{POM},B_{1g}}^e &= c_{eY,\mathbf{k}+\mathbf{Q}_Y\sigma}^\dagger c_{eY,\mathbf{k}+\mathbf{Q}_Y\sigma} - c_{eX,\mathbf{k}+\mathbf{Q}_X\sigma}^\dagger c_{eX,\mathbf{k}+\mathbf{Q}_X\sigma} \\ \Delta_{\text{POM},B_{1g}}^h &= \left( c_{h1,\mathbf{k}\sigma}^\dagger c_{h1,\mathbf{k}\sigma} - c_{h2,\mathbf{k}\sigma}^\dagger c_{h2,\mathbf{k}\sigma} \right) \cos 2\theta \\ &\quad + \left( c_{h1,\mathbf{k}\sigma}^\dagger c_{h2,\mathbf{k}\sigma} + c_{h2,\mathbf{k}\sigma}^\dagger c_{h1,\mathbf{k}\sigma} \right) \sin 2\theta\end{aligned}\quad (69)$$

The order parameters in the band basis describe the distortions of the Fermi surface and can be classified as Pomeranchuk order parameters in either the  $s$ -wave ( $A_{1g}$ ) or  $d$ -wave ( $B_{1g}$ ) channels. In general, there is no requirement that  $\Delta_{\text{POM},A_{1g}/B_{1g}}^e$  and  $\Delta_{\text{POM},A_{1g}/B_{1g}}^h$  are the same. To make this point explicit, we introduce symmetric and antisymmetric combinations of  $\Delta_j^e$  and  $\Delta_j^h$  in different irreducible channels. In analogy to the SC case, we label these combinations “plus-plus” and “plus-minus”:

$$\begin{aligned}\Delta_{s,\text{POM}}^{++} &= \Delta_{\text{POM},A_{1g}}^e + \Delta_{\text{POM},A_{1g}}^h \\ \Delta_{s,\text{POM}}^{+-} &= \Delta_{\text{POM},A_{1g}}^e - \Delta_{\text{POM},A_{1g}}^h \\ \Delta_{d,\text{POM}}^{++} &= \Delta_{\text{POM},B_{1g}}^e + \Delta_{\text{POM},B_{1g}}^h \\ \Delta_{d,\text{POM}}^{+-} &= \Delta_{\text{POM},B_{1g}}^e - \Delta_{\text{POM},B_{1g}}^h\end{aligned}\quad (70)$$

The average value  $\langle \Delta_{s,\text{POM}}^{++} \rangle$  is never zero and just reflects the fact that the chemical potential varies with the interaction. A non-zero average  $\langle \Delta_{s,\text{POM}}^{+-} \rangle$  accounts for an interaction-driven simultaneous shrinking (or expansion) of hole and electron pockets that does not affect charge conservation (see Fig. 17). Because this order parameter does not break any symmetry of the system, it is generally non-zero at any temperature [96, 134], as we discussed in Sec. II B. Yet, the susceptibility towards an  $s^{+-}$  Pomeranchuk instability may have a strong temperature dependence. This seems to be the case for FeSe and, possibly, other materials [135, 139, 140].

On the other hand, the onset of either  $\langle \Delta_{d,\text{POM}}^{++} \rangle$  or  $\langle \Delta_{d,\text{POM}}^{+-} \rangle$  does break tetragonal symmetry, distorting the hole Fermi pockets into ellipses and changing the relative sizes of the two electron pockets (see Fig. 17). As a result, these two order parameters can only appear below a particular temperature  $T_{\text{nem}}$ . Because the two are not orthogonal to each other, both are generally non-zero below  $T_{\text{nem}}$ . An equivalent way to state this is to define the  $d$ -wave Pomeranchuk order parameter in the orbital basis as

$$\Delta_{d,\text{POM}}(\mathbf{k}) = \left( d_{xz,\mathbf{k}\sigma}^\dagger d_{xz,\mathbf{k}\sigma} - d_{yz,\mathbf{k}\sigma}^\dagger d_{yz,\mathbf{k}\sigma} \right) f(\mathbf{k}) \quad (71)$$

By construction,  $f(\mathbf{Q}_X) = f(\mathbf{Q}_Y) = f(\mathbf{Q})$ . The non-equivalence of the  $B_{1g}$  order parameters on the hole and

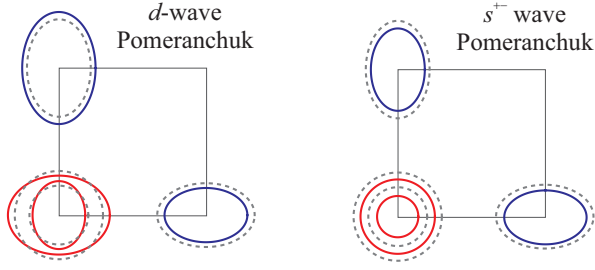


Figure 17. Pommeranchuk instabilities of the orbital-projected band model. Below the  $d$ -wave Pommeranchuk transition temperature, the originally circular hole pockets (dashed lines) are distorted into ellipses of opposite ellipticities (solid red lines), whereas the two electron pockets become inequivalent (solid blue lines). A non-zero  $s^{+-}$ -wave Pommeranchuk order parameter shrinks or expands all Fermi pockets equally, keeping the occupation number constant.

on the electron pockets implies that, in general,  $f(0) \neq f(\mathbf{Q})$ . Although the momentum range is confined to the vicinities of the  $\Gamma$  and  $X/Y$  points, one can still argue that in real space such an order parameter has on-site and bond components (between nearest neighbors, and, in general, also further neighbors). If  $f(0) \approx f(\mathbf{Q})$ , i.e.,  $\Delta_{d,\text{POM}}^{++} \gg \Delta_{d,\text{POM}}^{+-}$ , the on-site component is the largest, whereas if  $\Delta_{d,\text{POM}}^{++} \ll \Delta_{d,\text{POM}}^{+-}$ , the bond component is the dominant one.

Other forms of  $d$ -wave orbital order have been proposed [141, 142], but in the low-energy sector they are indistinguishable from the ones we introduced here – of course, as long as these order parameters do not mix the  $d$ -wave and  $s$ -wave symmetries, which remain strictly orthogonal within the model we discuss in this section due to the tetragonal symmetry of the system. To illustrate this, consider the  $d$ -wave orbital order with zero transferred momentum proposed in Ref. [141]:

$$\bar{\Delta}_{d,\text{POM}} = \left( d_{xz,\mathbf{k}\alpha}^\dagger d_{xz,\mathbf{k}\alpha} + d_{yz,\mathbf{k}\alpha}^\dagger d_{yz,\mathbf{k}\alpha} \right) (\cos k_x - \cos k_y) \quad (72)$$

One can readily verify that, if one restricts it to the low-energy sector, such an order parameter is the same as those in Eqs. (68) - (70), and it corresponds to  $\Delta_{B_{1g}}^h \ll \Delta_{B_{1g}}^e$ , i.e.  $\Delta_{d,\text{POM}}^{++} \approx \Delta_{d,\text{POM}}^{+-}$ .

### C. Interaction effects

We now turn to the analysis of the role of interactions. As before, our goal is to understand what kind of instabil-

ity (if any) develops in the system upon lowering the temperature, and whether different orders can coexist at the lowest temperature. We briefly review three approaches. Two fall into the “spin-fluctuation scenario”. The first is based on RPA and is not, strictly speaking, a low-energy approach. The second is a semi-phenomenological approach based on the low-energy spin-fluctuation model. The third approach is a low-energy one, based on RG. We consider these three approaches separately.

#### 1. RPA approach

This approach follows a similar analysis previously done for cuprate superconductors [75]. Its main goal is to understand the origin of SC pairing and the interplay between different pairing channels. The idea is to start with the full orbital model (no low-energy expansion) with on-site Hubbard and Hund interactions, split the interaction into the spin and charge channels, and use RPA to compute the effective spin-mediated pairing interaction between the electrons [12, 17, 18, 35, 91, 143, 144]. This procedure is uncontrolled but is generally justified on physics grounds because magnetism and superconductivity are close to each other on the phase diagram. The effective, magnetically-mediated pairing interaction can then be decomposed into different pairing channels and analyzed separately within each channel. This last analysis is done within the low-energy subset, by taking the pairing interaction as static but assuming that the upper cutoff for the pairing is much smaller than the bandwidth.

The RPA approach has been reviewed before [8, 75] and here we will just provide a brief description of the solution of the pairing problem with spin-mediated interaction. The pairing problem can be analyzed either numerically, by solving a large-size matrix equation for the eigenvalues in each pairing channel using the actual tight-binding band structure, or analytically. The analytical approach is based on the assumption that the pairing interaction  $\Gamma_{lm}(k, -k; p - p) \equiv \Gamma_{lm}(k, p)$ , where  $l, m$  label Fermi pockets, can be approximated by the lowest-order harmonics in the angular expansion, i.e., by the products of the terms that we listed in Eq. (66) (one for  $\mathbf{k}$ , another for  $\mathbf{p}$ ), and the terms with  $\cos 2\theta$  dependence along the electron pockets [145]. We show in Fig. 18 the comparison between the harmonic expansion and the actual interaction, showing that the two are close. Accordingly, we approximate  $\Gamma_{lm}(k, p)$  as

$$\begin{aligned}
\Gamma_{h_i h_j}(\theta_h, \theta'_h) &= U_{h_i h_j} + \tilde{U}_{h_i h_j} \cos 2\theta_h \cos 2\theta'_h \\
\Gamma_{h_i e_j}(\theta, \theta_e) &= U_{h_i e} (1 \pm 2\alpha_{h_i e} \cos 2\theta_e) + \tilde{U}_{h_i e} (\pm 1 + 2\tilde{\alpha}_{h_i e} \cos 2\theta_e) \cos 2\theta_h \\
\Gamma_{e_i e_j}(\theta_e, \theta'_e) &= U_{ee} [1 \pm 2\alpha_{ee} (\cos 2\theta_e + \cos 2\theta'_e) + 4\beta_{ee} \cos 2\theta_e \cos 2\theta'_e] + \tilde{U}_{ee} [1 \pm 2\tilde{\alpha}_{ee} (\cos 2\theta_e + \cos 2\theta'_e) + 4\tilde{\beta}_{ee} \cos 2\theta_e \cos 2\theta'_e] \\
\Gamma_{e_1 e_2}(\theta_e, \theta'_e) &= U_{ee} [1 + 2\alpha_{ee} (\cos 2\theta_e - \cos 2\theta'_e) - 4\beta_{ee} \cos 2\theta_e \cos 2\theta'_e] + \tilde{U}_{ee} [-1 - 2\tilde{\alpha}_{ee} (\cos 2\theta_e - \cos 2\theta'_e) + 4\tilde{\beta}_{ee} \cos 2\theta_e \cos 2\theta'_e]
\end{aligned} \tag{73}$$

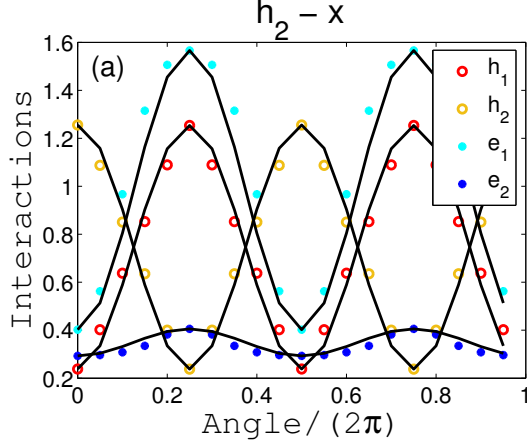


Figure 18. The pairing interactions  $\Gamma_{h_2\alpha}(0, \theta)$  involving the Fermi pocket  $h_2$  at the Fermi momentum corresponding to  $\theta_{h_2} = 0$  and the Fermi pocket  $\alpha = h_1, h_2, e_X, e_Y$  at the Fermi momentum corresponding to the polar angle  $\theta$ . Solid lines are the leading angular harmonic approximations in Eq. (73) whereas the symbols are the RPA results. Figure from Ref. [145].

Here the upper sign is for the electron pocket at  $Y$  (pocket  $e_Y$ ) and the lower sign is for the electron pocket at  $X$  (pocket  $e_X$ ). The indices  $i, j = 1, 2$  for the hole pockets and  $Y, X$  for the electron pockets. The angles  $\theta_h$  and  $\theta_e$  are along hole and electron pockets, respectively.

The coefficients are obtained by matching this  $\Gamma_{lm}(k, p)$  to the full RPA expression for spin-mediated pairing interaction. Once the prefactors are known, the pairing problem can be easily analyzed analytically within BCS theory. One cannot obtain the SC transition temperature  $T_c$  in this way, because the pairing interaction is taken as static, but one can compare eigenvalues in different channels. The first instability will be in the channel with the largest eigenvalue, at least at weak coupling.

Using this RPA-based spin-fluctuation approach, one can compare the eigenvalues in the  $s^{++}$ ,  $s^{+-}$ ,  $d_{x^2-y^2}$  and  $d_{xy}$  channels and also analyze the angular dependence of the gap function (the eigenfunction) corresponding to the largest eigenvalue. One also can analyze how many channels are attractive. In general, one finds that the leading SC instability is towards an  $s^{+-}$  state, but that

the  $d$ -wave state is very close in energy [12, 145, 146]. The same approach can be adapted to study pairing mediated by orbital fluctuations, if somehow the interaction in the CDW channel becomes attractive. The CDW-mediated interaction generally leads to superconducting instability in the  $s^{++}$  channel [60, 147].

The RPA approach clearly has advantages but also has its limitations. By construction, it analyzes the development of superconductivity prior to SDW magnetism, i.e. it does not address the issue of coexistence of magnetism and superconductivity (although the RPA approach can be modified to include this). It also neglects the feedback effect from SC fluctuations on the magnetic propagator. Finally, the approach has been designed to study only pairing and cannot be straightforwardly modified to study orbital order.

## 2. Spin-fermion model

An alternative reasoning is to abandon RPA and treat the static part of the magnetically-mediated interaction as an input for the low-energy model, with parameters taken from the experiment. The dynamical part of the magnetically-mediated interaction comes from fermions with low energies, and can be explicitly computed within the low-energy sector. One then use the full dynamical interaction to obtain  $T_c$ .

Such an approach has been applied to the cuprates and, more generally, to systems with interaction mediated by near-critical soft fluctuations (for a review, see Ref. [148]). In cases where the bosonic dynamics is dominated by Landau damping, bosons can be viewed as slow compared to fermions. In this situation, one can use Eliashberg theory to compute  $T_c$  and also the fermionic self-energy. Whether the same holds for FeSC needs further analysis because the bosonic dynamics is more complex than Landau damping due to the fact that both hole-like and electron-like excitations are present.

## 3. RG analysis

A third approach is to treat magnetism, superconductivity, and orbital order on equal footing and use the RG

technique described in Section III A to study the hierarchy of instabilities caused by interactions.

In contrast to the purely band-basis model discussed in that section, the orbital-projected band model contains information about the orbital content of the low-energy states. As a result, besides CDW, SDW, and SC, one can also study within RG the onset of orbital orders of different types [97].

One unavoidable complication is that the number of symmetry-allowed couplings between the low-energy states of the orbital-projected model is much larger than that in the purely band model. There, the maximum number of couplings was 8. Here the number of couplings for a generic model with two hole and two electron pockets made out of  $d_{xz}$ ,  $d_{yz}$ , and  $d_{xy}$  orbitals is 30 [49]. Once the  $d_{xy}$  pocket at the  $M$  point is added, the number grows to 40. These are also much larger numbers than the number of parameters  $U, U', J, J'$  in the onsite interaction Hamiltonian, Eq. (4). As we discussed in Sec. III C 1, the additional couplings can be viewed as interactions between Fe atoms on different sites.

The existence of 30 (or even 40) distinct couplings, which all flow under RG, complicates the analysis but also raises questions about the validity of RPA (or mean-field) approaches, which neglect the fact that the actual number of distinct couplings is much larger than those four in Eq. (4) – or, equivalently, that interactions between orbitals at nearest and further neighbors must be included into the theory, even if they are not present at the bare level. We argue below that non-onsite interactions are fundamental to describe the low-energy physics of FeSC.

To illustrate how the RG approach works and how its results differ from RPA, we consider below the simplified model in which the partial  $d_{xy}$  content of the  $X$  and  $Y$  electron pockets is neglected, i.e. we identify the electron pockets centered at  $X$  as purely  $d_{yz}$  and the one centered at  $Y$  as purely  $d_{xz}$ . To avoid repeating the RG analysis of the band models, we focus on the novel aspect of the RG analysis of the orbital-projected model, namely on the possibility that spontaneous orbital order may be a competitor to SDW and SC. Specifically, we discuss whether one can obtain attraction in the orbital channel despite

starting with purely repulsive interactions, and, if this is the case, whether orbital order can become the leading instability of the system. For details of this calculation we refer to Ref. [97].

#### 4. RG for the 4-pocket model without $d_{xy}$ orbital contribution

Without the  $d_{xy}$  contribution, the electron-pocket operators  $c_{e_i, \mathbf{k} + \mathbf{Q}_i \sigma}$  are pure orbital operators:

$$\begin{aligned} c_{e_X, \mathbf{k} + \mathbf{Q}_X \sigma} &= d_{yz, \mathbf{k} + \mathbf{Q}_X \sigma} \\ c_{e_Y, \mathbf{k} + \mathbf{Q}_Y \sigma} &= d_{xz, \mathbf{k} + \mathbf{Q}_Y \sigma} \end{aligned} \quad (74)$$

and the kinetic energy near the  $X$  and  $Y$  points is given by:

$$\begin{aligned} \mathcal{H}_{0,X} &= \sum_{\mathbf{k}\sigma} \varepsilon_{e_X}(\mathbf{k} + \mathbf{Q}_X) c_{e_X, \mathbf{k} + \mathbf{Q}_X \sigma}^\dagger c_{e_X, \mathbf{k} + \mathbf{Q}_X \sigma} \\ \mathcal{H}_{0,Y} &= \sum_{\mathbf{k}\sigma} \varepsilon_{e_Y}(\mathbf{k} + \mathbf{Q}_Y) c_{e_Y, \mathbf{k} + \mathbf{Q}_Y \sigma}^\dagger c_{e_Y, \mathbf{k} + \mathbf{Q}_Y \sigma} \end{aligned} \quad (75)$$

with effective band dispersions:

$$\begin{aligned} \varepsilon_{e_X}(\mathbf{k} + \mathbf{Q}_X) &= -\varepsilon_{e,0} + \frac{k_x^2}{2m_x} + \frac{k_y^2}{2m_y} \\ \varepsilon_{e_Y}(\mathbf{k} + \mathbf{Q}_Y) &= -\varepsilon_{e,0} + \frac{k_x^2}{2m_y} + \frac{k_y^2}{2m_x} \end{aligned} \quad (76)$$

The kinetic energy operator  $\mathcal{H}_{0,\Gamma}$ , presented in Eq. (41), remains unchanged because it does not have contributions from the  $d_{xy}$  orbital. To write down  $\mathcal{H}_{\text{int}}$ , we assemble all distinct interactions between low-energy fermions in the orbital basis. One can verify that there are 14 distinct electronic interactions involving the low-energy  $d_{xz}/d_{yz}$  orbital states near  $\Gamma$ ,  $X$ , and  $Y$ . We present all 14 in the formula below, where for simplicity of notation the momentum index is omitted and  $\tilde{d}$  operators are shorthand notations for  $\tilde{d}_{yz, \sigma} \equiv d_{yz, \mathbf{k} + \mathbf{Q}_X \sigma}$  and  $\tilde{d}_{xz, \sigma} \equiv d_{xz, \mathbf{k} + \mathbf{Q}_Y \sigma}$ :

$$\begin{aligned}
\mathcal{H}_{\text{int}} = & U_1 \sum \left[ \tilde{d}_{xz,\sigma}^\dagger \tilde{d}_{xz,\sigma} d_{xz,\sigma'}^\dagger d_{xz,\sigma'} + \tilde{d}_{yz,\sigma}^\dagger \tilde{d}_{yz,\sigma} d_{yz,\sigma'}^\dagger d_{yz,\sigma'} \right] + \bar{U}_1 \sum \left[ \tilde{d}_{yz,\sigma}^\dagger \tilde{d}_{yz,\sigma} d_{xz,\sigma'}^\dagger d_{xz,\sigma'} + \tilde{d}_{xz,\sigma}^\dagger \tilde{d}_{xz,\sigma} d_{yz,\sigma'}^\dagger d_{yz,\sigma'} \right] \\
& + U_2 \sum \left[ \tilde{d}_{xz,\sigma}^\dagger d_{xz,\sigma} d_{xz,\sigma'}^\dagger \tilde{d}_{xz,\sigma'} + \tilde{d}_{yz,\sigma}^\dagger d_{yz,\sigma} d_{yz,\sigma'}^\dagger \tilde{d}_{yz,\sigma'} \right] + \bar{U}_2 \sum \left[ \tilde{d}_{xz,\sigma}^\dagger d_{yz,\sigma} d_{yz,\sigma'}^\dagger \tilde{d}_{xz,\sigma'} + \tilde{d}_{yz,\sigma}^\dagger d_{xz,\sigma} d_{xz,\sigma'}^\dagger \tilde{d}_{yz,\sigma'} \right] \\
& + \frac{U_3}{2} \sum \left[ \tilde{d}_{xz,\sigma}^\dagger d_{xz,\sigma} \tilde{d}_{xz,\sigma'}^\dagger d_{xz,\sigma'} + \tilde{d}_{yz,\sigma}^\dagger d_{yz,\sigma} \tilde{d}_{yz,\sigma'}^\dagger d_{yz,\sigma'} \right] + \frac{\bar{U}_3}{2} \sum \left[ \tilde{d}_{xz,\sigma}^\dagger d_{yz,\sigma} \tilde{d}_{xz,\sigma'}^\dagger d_{yz,\sigma'} + \tilde{d}_{yz,\sigma}^\dagger d_{xz,\sigma} \tilde{d}_{yz,\sigma'}^\dagger d_{xz,\sigma'} \right] + h.c. \\
& + \frac{U_4}{2} \sum \left[ d_{xz,\sigma}^\dagger d_{xz,\sigma} d_{xz,\sigma'}^\dagger d_{xz,\sigma'} + d_{yz,\sigma}^\dagger d_{yz,\sigma} d_{yz,\sigma'}^\dagger d_{yz,\sigma'} \right] + \frac{\bar{U}_4}{2} \sum \left[ d_{xz,\sigma}^\dagger d_{yz,\sigma} d_{xz,\sigma'}^\dagger d_{yz,\sigma'} + d_{yz,\sigma}^\dagger d_{xz,\sigma} d_{yz,\sigma'}^\dagger d_{xz,\sigma'} \right] \\
& + \tilde{U}_4 \sum d_{xz,\sigma}^\dagger d_{xz,\sigma} d_{yz,\sigma'}^\dagger d_{yz,\sigma'} + \tilde{\bar{U}}_4 \sum d_{xz,\sigma}^\dagger d_{yz,\sigma} d_{yz,\sigma'}^\dagger d_{xz,\sigma'} \\
& + \frac{U_5}{2} \sum \left[ \tilde{d}_{xz,\sigma}^\dagger \tilde{d}_{xz,\sigma} \tilde{d}_{xz,\sigma'}^\dagger \tilde{d}_{xz,\sigma'} + \tilde{d}_{yz,\sigma}^\dagger \tilde{d}_{yz,\sigma} \tilde{d}_{yz,\sigma'}^\dagger \tilde{d}_{yz,\sigma'} \right] + \frac{\bar{U}_5}{2} \sum \left[ \tilde{d}_{xz,\sigma}^\dagger \tilde{d}_{yz,\sigma} \tilde{d}_{xz,\sigma'}^\dagger \tilde{d}_{yz,\sigma'} + \tilde{d}_{yz,\sigma}^\dagger \tilde{d}_{xz,\sigma} \tilde{d}_{yz,\sigma'}^\dagger \tilde{d}_{xz,\sigma'} \right] \\
& + \tilde{\bar{U}}_5 \sum \tilde{d}_{xz,\sigma}^\dagger \tilde{d}_{xz,\sigma} \tilde{d}_{yz,\sigma'}^\dagger \tilde{d}_{yz,\sigma'} + \tilde{\bar{U}}_5 \sum \tilde{d}_{xz,\sigma}^\dagger \tilde{d}_{yz,\sigma} \tilde{d}_{yz,\sigma'}^\dagger \tilde{d}_{xz,\sigma'} \quad (77)
\end{aligned}$$

If one departs from the model of Eq. (4) with only onsite interactions, the initial (bare) values of all 14 couplings are expressed in terms of  $U$ ,  $U'$ ,  $J$ , and  $J'$ :

$$\begin{aligned}
U_1 &= U_2 = U_3 = U_4 = U_5 = U, \\
\bar{U}_1 &= \tilde{U}_4 = \tilde{\bar{U}}_5 = U', \\
\bar{U}_2 &= \tilde{U}_4 = \tilde{\bar{U}}_5 = J, \\
\bar{U}_3 &= \bar{U}_4 = \bar{U}_5 = J' \quad (78)
\end{aligned}$$

However, as we said, different couplings evolve differently under RG. This can be interpreted as if the system generates interactions between  $d_{xz}$  and  $d_{yz}$  orbitals at neighboring sites.

Because the non-interacting Hamiltonian  $\mathcal{H}_0$  is diagonal in the band basis, it is useful to change the interacting part  $\mathcal{H}_{\text{int}}$  to the band basis as well. From Eqs. (40) and (74), it is clear that the effect of this change of basis is to dress the interactions with form factors that depend on the position at the Fermi pockets, i.e. to induce angle-dependent interactions enforced by the orbital contents of the Fermi pockets. Note in passing that the total number of different terms in the band basis is 152. They are clustered into 14 combinations and each combination flows as a whole under RG.

Before we discuss the results of the RG analysis, we briefly review the results of a mean-field approach. Within mean-field, different channels do not talk to each other and the susceptibility in each channel behaves as

$$\chi_j(T) = \frac{\chi_{j,0}(T)}{1 - \Gamma_j \chi_{j,0}(T)} \quad (79)$$

where  $j$  labels different channels: SDW, CDW, SC, Pomeranchuk, etc (positive  $\Gamma_j$  implies attraction). For the orbital-projected model with onsite interactions only, the couplings in the SDW,  $s^{+-}$  SC and  $d$ -wave Pomeranchuk channels are

$$\Gamma_{\text{SDW}} = 2U, \Gamma_{\text{SC}} = 0, \Gamma_{\text{POM}} = 2U' - U - J \quad (80)$$

We see that coupling in the  $s^{+-}$  SC channel vanishes, while the one in SDW channel is attractive and strong. The coupling in the Pomeranchuk channel is attractive if  $2U' > U + J$  (or  $U > 5J$  if we further impose spin-rotational invariance,  $U' = U - 2J$ ). Given that the susceptibility in the SDW channel is logarithmically enhanced and the one in the Pomeranchuk channel is just the density of states, it is obvious that SDW is the leading instability within mean-field.

We now turn to the RG analysis, which was formally explained above in Section III C 1. It turns out that for positive (repulsive)  $U_i$  in Eq. (77), there exists one stable fixed trajectory. Along this trajectory, the interactions  $\tilde{U}_{4,5}$  and  $\tilde{\bar{U}}_{4,5}$  flow to zero, whereas  $\bar{U}_i$  and  $U_i$  ( $i = 1, \dots, 5$ ) keep increasing and diverge at the same scale  $L_c = \log\left(\frac{\Lambda}{E_c}\right)$ . The ratios of the couplings approach universal numbers on a fixed trajectory, no matter what these ratios are at the bare level. In particular, in our case we obtain  $\bar{U}_i = U_i$  ( $i = 1, \dots, 5$ ) and universal values for the ratios  $U_i/U_1$ . All couplings flow as

$$U_i(L), \bar{U}_i(L) \sim \frac{1}{L_c - L} \quad (81)$$

We emphasize again that this result implies that commonly neglected non-onsite interactions become sizable and relevant.

The running couplings near the fixed trajectory are then used as inputs to compute the fully renormalized vertices in different channels and the corresponding susceptibilities  $\chi_j$ . These calculations show that the susceptibilities in the  $s^{+-}$  SC channel, the SDW channel, and the  $d$ -wave Pomeranchuk channel behave as [97]:

$$\chi_j \sim \frac{1}{(L_c - L)^{\alpha_j}} \quad (82)$$

In Fig. 19, we show the behavior of the exponents  $\alpha_j$  as functions of the ratio between the electron- and hole-pocket masses. Across the entire parameter space

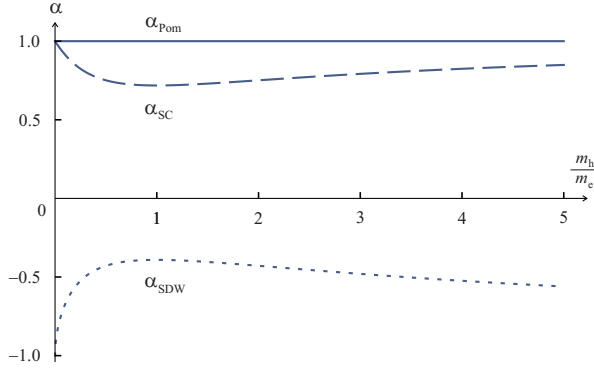


Figure 19. RG results from Ref. [97] for the orbital-projected band model showing the behavior of the susceptibility exponents defined in Eq. (82) as function of the ratio between the hole pocket mass  $m_h$  and the electron pocket mass  $m_e$ .

$\alpha_{\text{POM}} > \alpha_{\text{SC}} > 0 > \alpha_{\text{SDW}}$ , implying that at the energy scale  $E_c$  the leading instability is in the  $d$ -wave Pomeranchuk channel, towards a spontaneous orbital order. The SC susceptibility also diverges, albeit with a smaller exponent, implying that the instability in this channel is the subleading one. Interestingly, because  $\alpha_{\text{SDW}} < 0$ , the SDW susceptibility saturates and does not diverge at  $E_c$ , despite the fact that this susceptibility is the largest at the beginning of the RG flow.

A natural question that arises from these results is why the leading instability is towards orbital order despite the facts that the free-electron susceptibility  $\chi_{\text{POM},0}$  has no logarithmic divergence and the bare interaction  $\Gamma_{\text{POM}}$  is generally not attractive. The short answer is that the attractive interaction in this channel can be viewed as mediated by magnetic fluctuations, like the attraction in  $s^{+-}$  SC channel. In other words, magnetic fluctuations develop first in the process of the RG flow, and mediate an attractive interaction, which grows logarithmically as high-energy fluctuations get progressively integrated out and completely overcomes the bare interactions in both  $s^{+-}$  SC and  $d$ -wave Pomeranchuk channels. We see that the mechanisms for attraction in the Pomeranchuk and in the  $s^{+-}$  SC channel are quite similar.

The magnetically-mediated attractive interaction in the pairing channel also develops within RPA, and in this respect RG and RPA approaches describe the same physics. However, within RPA, one would always find the leading instability to be in the SC channel because the bare SC susceptibility grows logarithmically, while the bare Pomeranchuk susceptibility is just a constant. In contrast, the RG treatment goes farther than RPA and shows that, once the SC channel becomes attractive, it starts competing with the SDW channel, and, as a result of the competition, the tendency towards instabilities in both channels is reduced. This in practice implies that the exponents  $\alpha_{\text{SC}}$  and  $\alpha_{\text{SDW}}$  become smaller than one (which is their mean-field values), and that  $\alpha_{\text{SDW}}$  even changes sign and becomes negative. Because the susceptibility in the Pomeranchuk channel is non-logarithmic,

this channel competes much less with the other two channels. As a consequence, the exponent  $\alpha_{\text{POM}}$  remains equal to one. Such an intricate interplay between different channels illustrates the usefulness of unbiased methods such as RG.

An important point to note is that this result does not imply that in all cases the leading instability of the system is the Pomeranchuk one. As we explained previously in Section III, once  $E$  reaches the scale of the largest Fermi energy, i.e.  $L$  reaches  $L_F \equiv \log\left(\frac{\Lambda}{E_F}\right)$ , different instability channels decouple and the RG scheme breaks down. The most important point for our discussion is that  $\chi_{\text{POM}}$  freezes out at  $L = L_F$ , while the susceptibilities in the SC and SDW channels continue to grow (the SDW susceptibility eventually also freezes out due to non-perfect nesting, but at a much larger  $L$ ). Because  $\chi_{\text{POM}}$  is only enhanced very close to  $L_c$  [97], in systems where the ratio  $E_F/\Lambda$  is moderate, such as the 122, 1111, and 111 FeSC compounds, the RG flow is likely to stop before the Pomeranchuk channel becomes relevant. As a result, one basically recovers the results of the band-basis models of Section III, in that only SC and SDW channels are relevant. In this case, a nematic phase can only arise via a partial melting of the SDW stripe phase, as we discussed in Section III C 3. On the other hand, in systems where  $E_F/\Lambda$  is small, and  $E_F$  and  $E_c$  are comparable, the leading instability of the system is in the  $d$ -wave Pomeranchuk channel, the SC instability is the subleading one, and the SDW instability does not develop. In this case, nematicity is a result of spontaneous orbital order.

This general behavior agrees with the phase diagram of FeSe, where nematic order arises in the presence of weak magnetic fluctuations, and in the absence of long-range magnetic order [136, 149, 150]. Once pressure is applied and  $E_F/\Lambda$  necessarily increases for at least one pocket, the system crosses over to a typical iron-pnictide like behavior, with nematic order preempting a stripe SDW phase [151, 152].

Besides the SDW, SC, and  $d$ -wave Pomeranchuk instabilities, another susceptibility of the system that diverges at  $L_c$  within the one-loop RG analysis is in the  $s^{+-}$ -wave Pomeranchuk channel (see also [153]). For the model of Eq. (77), a more accurate analysis [97] shows that this susceptibility actually diverges at a larger energy (equivalent to a higher temperature) than the one in the  $d$ -wave channel. As we already said, the divergence of the susceptibility in the  $s^{+-}$  Pomeranchuk channel is an artifact of the one-loop RG, since in reality the  $s^{+-}$  Pomeranchuk order parameter is non-zero at all temperatures. Yet, the RG analysis shows that the magnitude of the  $s^{+-}$  order parameter strongly increases around the temperature at which the corresponding susceptibility diverges in RG. The analysis in Ref. [96] reveals a self-energy contribution that favors a shift between the top of the hole band and the bottom of the electron band such that the areas of both Fermi pockets decrease. Combined with the RG result, this implies that as temperature decreases, the system should show a significant temperature-dependent

shrinking of both hole-like and electron-like Fermi pockets.

### 5. Inclusion of the $d_{xy}$ orbital contribution and 5-pocket model

To incorporate the  $d_{xy}$  orbital into the previous analysis, we assume first that the  $M$ -point hole pocket is absent (for instance, it is sunk below the Fermi level, as in the 111 and 11 materials). Then the only difference with respect to the model analyzed above is the presence of  $d_{xy}$  spectral weight on the electron pockets. In the hypothetical case in which these electron pockets are entirely of  $d_{xy}$  character, i.e.  $c_{eX,\mathbf{k}+\mathbf{Q}_X\sigma} \equiv d_{xy,\mathbf{k}+\mathbf{Q}_X\sigma}$  and  $c_{eY,\mathbf{k}+\mathbf{Q}_Y\sigma} \equiv d_{xy,\mathbf{k}+\mathbf{Q}_Y\sigma}$ , the number of interactions remains 14, and the RG analysis yields the same results as for  $d_{xz}/d_{yz}$  electron pockets [97]. Because the results of the RG study are identical in the two limits, we expect them to hold in a generic situation in which electron pockets have both  $d_{xy}$  and  $d_{yz}/d_{xz}$  spectral weight.

The only additional effect introduced by the  $d_{xy}$  orbital is that the nematic order now has two components – one is the orbital order component  $n_{xz} - n_{yz}$ , and the other is  $n_{xy}^X - n_{xy}^Y$ , which is the difference between the  $d_{xy}$ -orbital charge densities at the  $X$  and  $Y$  electron pockets. The latter is not associated with any type of orbital order, but rather with the fact that the two electron pockets are located at non-diagonal  $X$  and  $Y$  points in the Brillouin zone. This second component can be interpreted as a  $C_4$ -symmetry breaking anisotropy of the hoppings between nearest-neighbor  $d_{xy}$  orbitals. It is closely related to the  $d$ -wave Pomeranchuk order in the pure 3-band model (see the discussion in Section III C 3). While the orbital order component of the nematic order parameter splits the on-site energies of the  $d_{xz}$  and  $d_{yz}$  orbitals at the  $\Gamma$ ,  $X$ , and  $Y$  points, the hopping anisotropy component splits the equivalence between the energy levels of the  $d_{xy}$  orbitals at the  $X$  and  $Y$  points. In general, both components are present, and their ratio depends on the details of the RG flow [137, 154].

We now include the fifth Fermi pocket, namely, the  $d_{xy}$  hole-pocket at  $M$ . An interesting issue is whether this leads to qualitatively new behavior. A recent analysis argues that the main results remain the same [154]. Specifically, there are several stable and “almost stable” fixed trajectories, each with its own basin of attraction in the parameters space. If the system parameters are such that the RG flow extends down to the lowest energy, the leading instability for each fixed trajectory is towards orbital order, the SC instability is the subleading one, and the SDW susceptibility does not diverge. If the system parameters are such that the RG flow is halted at higher energies, the system develops either SDW or SC order. The nematic order parameter generally has two components, one describing orbital order and another one the breaking of  $C_4$  symmetry within the subset of  $d_{xy}$  orbitals.

Nevertheless, the analysis of the RG flow for the orbital-projected 5-pocket model shows a new feature. Depending on the initial parameters, the system flows at low energies either into the “phase  $A$ ”, where the largest interactions are within the subset of the two  $\Gamma$  hole pockets and the two  $X$ ,  $Y$  electron pockets, or into the “phase  $B$ ”, where the largest interactions are within the subset of the  $M$  hole pocket and the two  $X$ ,  $Y$  electron pockets. Such a separation has been proposed earlier for LiFeAs [57], but for a different reason, related to the topology of the Fermi surfaces. This separation opens up the possibility for novel  $s^{+-}$  superconducting states, such as the orbital anti-phase state [56], in which the gap function on the  $M$  hole pocket has opposite sign with respect to the gaps on the  $\Gamma$  hole pockets.

The separation between the  $A$  and  $B$  phases can also provide interesting insight into the selection of magnetic order – i.e. whether it is stripe-like (single- $\mathbf{Q}$ ) or double- $\mathbf{Q}$ . If we consider only intra-orbital magnetism, we can generally define two magnetic order parameters for each set (the hermitian conjugate in each expression is left implicit for simplicity of notation):

$$\begin{aligned}\Delta_{\text{SDW},X}^A(\mathbf{k}) &\equiv \Delta_{A,X} \propto d_{yz,\mathbf{k}\alpha}^\dagger \sigma_{\alpha\beta} d_{yz,\mathbf{k}+\mathbf{Q}_X\beta} \\ \Delta_{\text{SDW},Y}^A(\mathbf{k}) &\equiv \Delta_{A,Y} \propto d_{xz,\mathbf{k}\alpha}^\dagger \sigma_{\alpha\beta} d_{xz,\mathbf{k}+\mathbf{Q}_Y\beta} \\ \Delta_{\text{SDW},X}^B(\mathbf{k}) &\equiv \Delta_{B,X} d_{xy,\mathbf{k}+\mathbf{Q}_X+\mathbf{Q}_Y\alpha}^\dagger \sigma_{\alpha\beta} d_{xy,\mathbf{k}+\mathbf{Q}_Y\beta} \\ \Delta_{\text{SDW},Y}^B(\mathbf{k}) &\equiv \Delta_{B,Y} \propto d_{xy,\mathbf{k}+\mathbf{Q}_X+\mathbf{Q}_Y\alpha}^\dagger \sigma_{\alpha\beta} d_{xy,\mathbf{k}+\mathbf{Q}_X\beta}\end{aligned}\quad (83)$$

The total free energy can then be written as

$$F = F_A + F_B + F_{AB} \quad (84)$$

The terms  $F_A$  and  $F_B$  are given by the same expression as in Eq. (31):

$$\begin{aligned}F_j &= \frac{a_j}{2} (\Delta_{j,X}^2 + \Delta_{j,Y}^2) + \frac{u_j}{4} (\Delta_{j,X}^2 + \Delta_{j,Y}^2)^2 \\ &\quad - \frac{g_j}{4} (\Delta_{j,X}^2 - \Delta_{j,Y}^2)^2 + w_j (\Delta_{j,X} \cdot \Delta_{j,Y})^2\end{aligned}\quad (85)$$

with  $j = A, B$ . The sign of  $g_j$  determines whether the ground state is single- $\mathbf{Q}$ ,  $g_j > 0$  (and therefore orthorhombic), or double- $\mathbf{Q}$ ,  $g_j < 0$  (and therefore tetragonal). Expansions near the perfect nesting limit show that  $g_A < 0$  whereas  $g_B > 0$ . That  $g_B > 0$  can be understood within the 3-band only model of Sec. III C 3 (see also Ref. [76], which includes the orbital content of the Fermi surface). To see that  $g_A < 0$ , one has to include explicitly the matrix elements associated with the change from orbital to band basis [155]. Because  $g_A$  and  $g_B$  have different signs, the two “phases” favor different magnetic states: the phase  $A$  favors a double- $\mathbf{Q}$  SDW phase and the phase  $B$  favors a single- $\mathbf{Q}$  phase. A similar observation was put forward by numerical evaluation of the elements of the rank-4 nematic tensor in the full five-orbital model [77].

Which of the two types of SDW order is developed by the system depends on the strength of the biquadratic coupling in the mixed term:

$$F_{AB} = \lambda (\Delta_{A,X}^2 - \Delta_{A,Y}^2) (\Delta_{B,X}^2 - \Delta_{B,Y}^2) + (\dots) \quad (86)$$

This term in generally renormalizes  $g_A$  and  $g_B$ . In particular, if nematic fluctuations arising from  $B$  are strong enough, they change the sign of  $g_A$  and stabilize the single- $Q$  phase, even if the  $M$  hole pocket rests below the Fermi level. While the complete analysis is more involved, this simple reasoning already reveals the key role played by the  $d_{xy}$  orbitals in promoting the experimentally observed stripe SDW phase.

#### D. Ising-nematic order vs orbital order

In the previous subsections we identified two possible microscopic mechanisms for nematic order – a spontaneous Pomeranchuk instability for small  $E_F/\Lambda$  and a partial melting of stripe SDW (a spin-driven Ising-nematic order) for larger  $E_F/\Lambda$ . Although these two scenarios may appear completely different, this is actually not the case because both orders develop due to magnetic fluctuations.

We illustrate this point in Fig. 20. The fundamental mechanism by which the exchange of magnetic fluctuations promotes attraction in the  $d$ -wave Pomeranchuk channel is via the Aslamazov-Larkin diagram of Fig. 20a [7, 88, 125, 156]. This is one of the diagrams that determine the RG flow of the susceptibility in the  $d$ -wave Pomeranchuk channel. A ladder series of these diagrams yields a nematic instability. The composition of the ladder series, however, depends on how we interpret the fundamental diagram in Fig. 20a [157].

Near a magnetic instability, the energy scale associated with the magnetic propagator (wavy lines in the diagram) is much smaller than the energy scale associated with the electronic degrees of freedom. In this case, the triangular diagrams in Fig. 20a, which involve only electronic propagators, can be replaced by a constant. By the same reason, the electronic propagators in higher-order diagrams can be assembled into effective interactions between low-energy magnetic fluctuations (Fig. 20b). An infinite ladder series resulting from the interactions between magnetic fluctuations can then be summed up, yielding a nematic susceptibility of the form of Eq. (34). When the SDW ground state is stripe-like ( $g > 0$  in Eq. (34)), the nematic susceptibility diverges before the bare magnetic susceptibility. This is the mechanism in which nematic order appears as an Ising-nematic order.

Far from a magnetic instability, however, the energy scale associated with magnetic fluctuations can become larger than  $E_F$ . If this is the case, then the electronic degrees of freedom should be viewed as the lowest-energy excitations. As a result, magnetic fluctuations can be integrated out, what in practice implies that the internal part of the diagram in Fig. 20a, which involves the

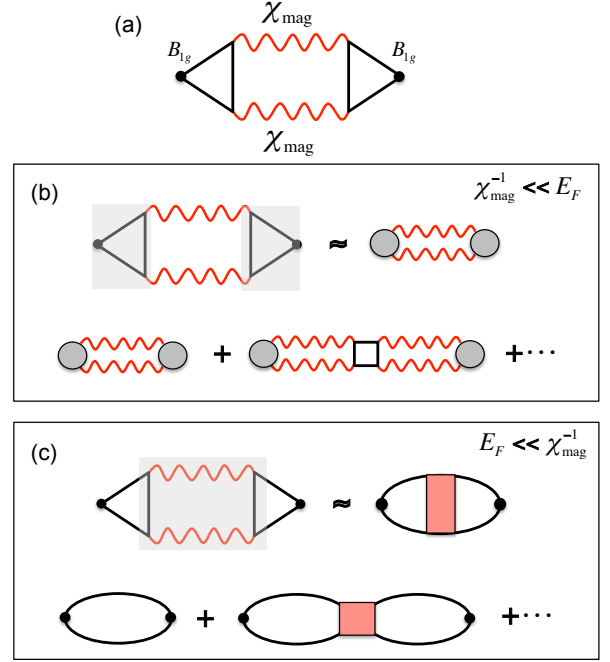


Figure 20. (a) Schematic Aslamazov-Larkin diagram representing the attraction in the Pomeranchuk channel promoted by the exchange of magnetic fluctuations. Solid lines represent electronic propagators, wavy lines denote the magnetic propagator, and the dots in the vertices refer to  $B_{1g}$  form factors. (b) In the case where the energy scale of the magnetic fluctuations is much smaller than the energy scale of the electronic states, the triangular diagrams involving the electron propagators can be replaced by an effective vertex. The nematic susceptibility is obtained by summing the ladder series in which magnetic fluctuations interact via square diagrams formed by higher-energy electronic propagators. (c) In the case where the energy scale of the electronic states is much smaller than the energy scale of the magnetic fluctuations, the square diagram involving the two magnetic propagators can be replaced by an effective attractive interaction. The nematic susceptibility is obtained by summing the corresponding ladder series.

two magnetic propagators, can be replaced by an effective attractive 4-fermion interaction in the  $d$ -wave Pomeranchuk channel ( Fig. 20c). An infinite ladder series of such terms then gives rise to an instability, which can be naturally identified as the development of a spontaneous Pomeranchuk instability arising from this effective attractive interaction. This is the mechanism by which nematic order arises via a spontaneous orbital order.

#### V. 1-FE VERSUS 2-FE UNIT CELLS

Up to this point our analysis of the low-energy microscopic model for the FeAs plane focused on the BZ formed by the in-plane Fe square lattice – the so-called 1-Fe BZ. The puckering of the As atoms, whose posi-

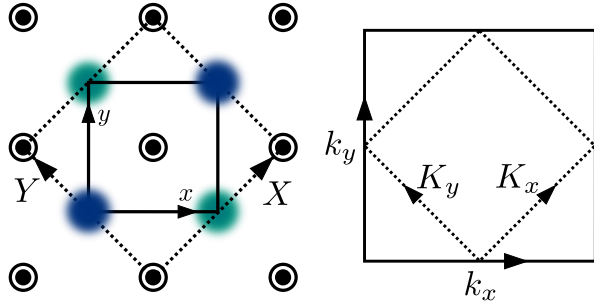


Figure 21. (left panel) The puckering of the As atoms above (green dots) and below (blue dots) the plane containing the Fe atoms (black dots) increase the size of the unit cell from 1 Fe atom (solid lines,  $x, y$  coordinates) to 2 Fe atoms (dashed lines,  $X, Y$  coordinates). (right panel) The unfolded ( $k_x, k_y$ ) BZ referring to the 1-Fe unit cell (solid lines) and the folded ( $K_x, K_y$ ) BZ referring to the 2-Fe unit cell (dashed lines). Figure from Ref. [55].

tions at the center of the Fe plaquettes alternate between above and below the Fe plane, changes the situation significantly. As we mentioned in the Introduction, one of the effects of the As puckering is to suppress the crystal field splittings between different orbitals and to promote a strong hybridization between them [11]. More importantly, however, the existence of two inequivalent sites for the As atoms enhances the size of the FeAs crystallographic unit cell to that containing 2 Fe atoms, see Fig. 21 [15, 16].

The first effect of the doubling of the unit cell is that one has to half the BZ and, consequently, fold the Fermi surface accordingly. Let the unfolded 1-Fe BZ be described by the coordinate system ( $k_x, k_y$ ), and the folded 2-Fe BZ by ( $K_x, K_y$ ). The momenta of each zone are then related by a trivial 45° rotation:

$$\begin{aligned} K_x &= k_x - k_y \\ K_y &= k_x + k_y \end{aligned} \quad (87)$$

where the momentum in the unfolded zone is measured in units of the inverse lattice constant of the 1-Fe unit cell,  $1/a$ , whereas the momentum in the folded zone is measured in units of the inverse lattice constant of the 2-Fe unit cell,  $1/(\sqrt{2}a)$ . Hereafter we denote with symbols with a bar high-symmetry points of the folded BZ. Using Eq. (87), we find  $\bar{M} = X = Y$  and  $\bar{\Gamma} = \Gamma = M$ .

The band-structure folding resulting from the halving of the BZ is shown schematically in Fig. 22. To obtain the folded Fermi surface, one makes a copy of the original Fermi surface (in red in Fig. 22) and translates it by the folding vector  $\mathbf{Q}_{\text{fold}} = (\pi, \pi)$  (in blue in Fig. 22). Besides the 45° degree rotation, the main effect of the folding is to move the two electron pockets to  $\bar{M}$  and the third hole pocket to  $\bar{\Gamma}$ .

Because  $\bar{M} = X = Y$ , another consequence of the doubling of the unit cell is that the two magnetic or-

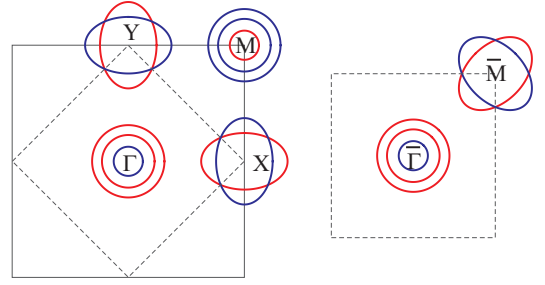


Figure 22. Schematics for the folding of the 1-Fe BZ (solid line) onto the 2-Fe BZ (dashed line). The red Fermi pockets correspond to the original ones in the 1-Fe BZ, whereas the blue Fermi pockets correspond to the original ones translated by the folding vector  $\mathbf{Q}_{\text{fold}} = (\pi, \pi)$ . The folded zone, rotated by 45° in the right panel for better visualization, contains both the original and translated pockets.

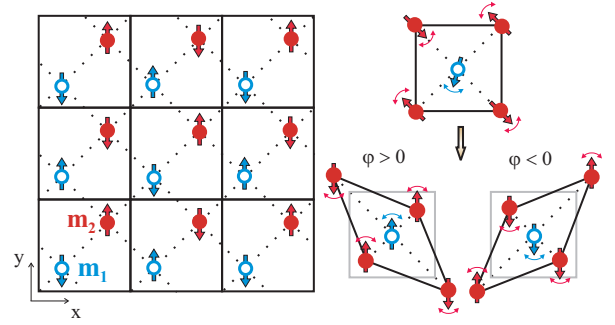


Figure 23. Nematic order in the 2-Fe unit cell: different signs of the nematic order parameter  $\varphi$  correspond to different relative orientations of the spins of the two Fe atoms (red and blue) in the same unit cell. Figure from Ref. [125].

dering vectors  $\mathbf{Q}_X = (\pi, 0)$  and  $\mathbf{Q}_Y = (0, \pi)$  in the unfolded zone are mapped onto the same ordering vector  $\mathbf{Q}_{\bar{M}} = (\pi, \pi)$  of the folded zone. Therefore, nematic order, which in the 1-Fe unit cell is related to the competition between  $\mathbf{Q}_X$  and  $\mathbf{Q}_Y$  SDW orders, is more conveniently associated, in the 2-Fe unit cell, with the relative orientation of the spins of the two Fe atoms inside the same unit cell (see Fig. 23) [122, 125]. Similarly, the fact that  $\bar{\Gamma} = \Gamma = M$  implies that any instability involving  $\mathbf{Q}_M = (\pi, \pi)$  ordering in the unfolded zone becomes an intra-unit cell order, without additional translational symmetry breaking. As a result, Neel-type SDW order becomes more difficult to be observed experimentally since the ordering vector coincides with a lattice Bragg peak.

The band folding is also accompanied by important effects that affect both the electronic dispersion as well as the instabilities of the system. These effects arise from terms in the Hamiltonian that couple electronic states separated by momentum  $\mathbf{Q}_{\text{fold}} = (\pi, \pi)$ . In the non-interacting level, two terms in the Hamiltonian become particularly important in the 2-Fe folded zone: the first one corresponds to the hybridization between states at

the  $X$  and  $Y$  pockets:

$$\mathcal{H}_{\text{hyb}} = \sum_{\mathbf{k}} f_{\text{hyb}}(\mathbf{k}) c_{e_X, \mathbf{k} + \mathbf{Q}_X \sigma}^\dagger c_{e_Y, \mathbf{k} + \mathbf{Q}_Y \sigma} + h.c. \quad (88)$$

As shown in Refs. [94, 158], this term arises from the hybridization between Fe  $3d$  states and As  $2p$  states. The momentum dependence of  $f_{\text{hyb}}(\mathbf{k})$  is a consequence of the orbital content of the Fermi surface, and vanishes along the diagonals of the folded BZ. The  $(\pi, \pi)$  terms also appear in the interacting part of the Hamiltonian.

The second non-interacting term corresponds to the atomic spin-orbit coupling (SOC), which connects states at the  $X$  and  $Y$  pockets according to  $\mathcal{H}_{\text{SOC}} = \lambda \mathbf{L} \cdot \mathbf{S}$ . In terms of the orbital operators, it corresponds to [49]

$$\begin{aligned} \mathcal{H}_{\text{SOC}} = & \frac{i}{2} \lambda \sum_{\mathbf{k}} d_{xz, \mathbf{k} + \mathbf{Q}_Y \alpha}^\dagger \sigma_{\alpha\beta}^x d_{xy, \mathbf{k} + \mathbf{Q}_X \beta} + h.c. \\ & + \frac{i}{2} \lambda \sum_{\mathbf{k}} d_{xy, \mathbf{k} + \mathbf{Q}_Y \alpha}^\dagger \sigma_{\alpha\beta}^y d_{yz, \mathbf{k} + \mathbf{Q}_X \beta} + h.c. \end{aligned} \quad (89)$$

In contrast to the hybridization term in Eq. (88), the SOC splits the folded electron pockets into two separate electron pockets – an inner one, of mostly  $d_{xz}$  and  $d_{yz}$  character, and an outer one, of mostly  $d_{xy}$  character. Besides these two non-interacting terms, interactions involving momentum transfer  $\mathbf{Q}_{\text{fold}} = (\pi, \pi)$  also couple the states at the  $X$  and  $Y$  pockets.

Below, we discuss how the models presented in the previous sections need to be modified to account for the doubling of the Fe unit cell.

### A. Orbital-basis models

We start with the models defined in the orbital basis only (Section II): in the 2-Fe BZ, one has to consider ten Fe  $3d$  orbitals (assuming that the six As  $2p$  orbitals can be integrated out). The general structure of the non-interacting Hamiltonian, in the folded zone, can be expressed by introducing the operator [15]:

$$\phi_{\mathbf{K}} = \begin{pmatrix} \phi_{1, \mathbf{K}} \\ \phi_{2, \mathbf{K}} \end{pmatrix} \quad (90)$$

where  $\phi_{i, \mathbf{K}}$  is a 5-component operator consisting of the orbital-basis operators  $d_{j, \mathbf{k}\sigma}^{(i)}$ , with  $j = xz, yz, x^2 - y^2, xy, z^2$  (the orbitals remain labeled with respect to the coordinate system of the 1-Fe BZ). In this notation, the non-interacting Hamiltonian assumes the form:

$$\mathcal{H}_0 = \sum_{\mathbf{k}} \phi_{\mathbf{K}}^\dagger \begin{pmatrix} \hat{H}_{11}(\mathbf{K}) & \hat{H}_{12}(\mathbf{K}) \\ \hat{H}_{12}^*(\mathbf{K}) & \hat{H}_{11}^*(\mathbf{K}) \end{pmatrix} \phi_{\mathbf{K}} \quad (91)$$

where  $\hat{H}_{i_1 i_2}$  are  $5 \times 5$  matrices. We refrain here from giving the full expressions for these tight-binding dispersions, which can be found in Ref. [15].

If terms that couple  $\phi_{1, \mathbf{K}}$  and  $\phi_{2, \mathbf{K}}$  are present, like those in Eqs. (88) and (89), then one has no choice but to work with the full ten-orbital model. However, if these specific interactions are absent, it is possible to “unfold” the 2-Fe BZ using a glide-plane symmetry of the FeAs plane. Indeed, the space group of a single FeAs plane is the non-symmorphic  $P4/nmm$  group, which contains a glide-plane symmetry corresponding to a translation by  $T = (\frac{1}{2}, \frac{1}{2})$  in the 2-Fe unit cell followed by a reflection  $\sigma_z$  with respect the  $xy$  plane. Inspection of Fig. 21 shows that indeed under this sequence of operations the lattice is mapped back onto itself.

The key point is that the  $d_{x^2-y^2}$ ,  $d_{xy}$ , and  $d_{z^2}$  orbitals are even under the reflection  $\sigma_z$ , while the orbitals  $d_{xz}$  and  $d_{yz}$  are odd. Consequently, because the two Fe sites in the same unit cell are related by a  $T = (\frac{1}{2}, \frac{1}{2})$  translation, the  $d_{xz}$  and  $d_{yz}$  orbitals change sign from one of these Fe sites to the other. As a result, one can use the eigenvalues of the operator  $T\sigma_z$  to diagonalize the Hamiltonian and express the electronic states in terms of a pseudocrystal momentum  $\tilde{\mathbf{k}}$ . The orbital states  $\tilde{d}_{\mu, \tilde{\mathbf{k}}\sigma}$  with pseudocrystal momentum  $\tilde{\mathbf{k}}$  are related to the orbital states  $d_{\mu, \mathbf{k}\sigma}$  with momentum  $\mathbf{k}$  in the unfolded BZ according to [52]:

$$\tilde{d}_{\mu, \tilde{\mathbf{k}}\sigma} = \begin{cases} d_{\mu, \mathbf{k}\sigma} & , \mu \text{ even} \\ d_{\mu, \mathbf{k} + \mathbf{Q}_{\text{fold}}\sigma} & , \mu \text{ odd} \end{cases} \quad (92)$$

where  $\mathbf{Q}_{\text{fold}} = (\pi, \pi)$ . Therefore, most of the results obtained in the studies of the orbital models defined in the unfolded zone can be directly translated to results in the actual crystallographic zone by means of the pseudocrystal momentum. Such a procedure has been implemented in different works [52, 80, 159–162], highlighting the importance of the glide-plane symmetry in the properties of the electronic spectrum (particularly the spectral weight of the electron pockets observed by ARPES) and of the SC state (such as the role of the so-called  $\eta$ -pairing).

We emphasize that this analysis is restricted to a single FeAs plane. The real materials, however, consist of many coupled layers. In the materials whose unit cells contain a single FeAs plane, such as the 1111 (e.g. LaFeAsO), the 111 (e.g. NaFeAs), and the 11 (e.g. FeSe) compounds, the stacking of the FeAs planes is such that the three-dimensional crystallographic unit cell retains the  $P4/nmm$  space group. As a result, even after including the  $k_z$  dispersion, this approach to describe the tight-binding dispersions in the full BZ remains essentially the same [49]. The situation is however different in the 122 (e.g. BaFe<sub>2</sub>As<sub>2</sub>) compounds, because their unit cell becomes body-centered tetragonal, instead of simple tetragonal. As a result, the space group of the crystallographic unit cell is  $I4/mmm$ , which is symmorphic. In this case, the “folding vector” changes from  $\mathbf{Q}_{\text{fold}} = (\pi, \pi, 0)$  to  $\mathbf{Q}_{\text{fold}} = (\pi, \pi, \pi)$ , which has important consequences for

the  $k_z$  dispersion of the different Fermi pockets [163]. The effect of the inter-layer coupling to the properties of the FeSC is important [66], but is beyond the scope of this review in which we consider only the case of a single FeAs layer effectively uncoupled from the other layers.

### B. Orbital-projected band models

One of the advantages of the orbital-projected band models of Section IV is that they can be generalized in a straightforward way to the 2-Fe BZ, without having to include additional electronic states. This is in contrast to the orbital-basis models, in which the number of orbitals double when going from the 1-Fe unit cell to the 2-Fe unit cell.

The reason for this behavior stems from the properties of the  $P4/nmm$  space group describing the single FeAs plane. As discussed in details in Ref. [49], the non-symmorphic nature of this group implies that, while the irreducible representations at the  $\bar{\Gamma}$  point are essentially the same as those of the standard  $D_{4h}$  group, the irreducible representations at the  $\bar{M}$  point must all be two-dimensional. As a result, all electronic states at the  $\bar{M}$  point must be doubly-degenerate and form doublets, and the electronic instabilities must be classified according to these irreducible representations (for details, see Ref. [49]).

Physically, this double-degeneracy at the  $\bar{M}$  point is manifested in the tight-binding dispersions of the 1-Fe BZ by the fact that  $\epsilon_{xx}(\mathbf{Q}_Y) = \epsilon_{yy}(\mathbf{Q}_X)$  and  $\epsilon_{xy}(\mathbf{Q}_Y) = \epsilon_{xy}(\mathbf{Q}_X)$ . These doublets can be expressed as spinors  $\psi_{\bar{M}_1}$  and  $\psi_{\bar{M}_3}$  (following the notation of Ref. [49]) formed by combinations of the spinors  $\psi_X$  and  $\psi_Y$  defined in Subsection IV C 5:

$$\begin{aligned} \psi_{\bar{M}_1, \mathbf{k} + \mathbf{Q}_{\bar{M}}} &= \begin{pmatrix} c_{xz, \mathbf{k} + \mathbf{Q}_2 \sigma} \\ c_{yz, \mathbf{k} + \mathbf{Q}_1 \sigma} \end{pmatrix} \\ \psi_{\bar{M}_3, \mathbf{k} + \mathbf{Q}_{\bar{M}}} &= \begin{pmatrix} c_{xy, \mathbf{k} + \mathbf{Q}_2 \sigma} \\ c_{xy, \mathbf{k} + \mathbf{Q}_1 \sigma} \end{pmatrix} \end{aligned} \quad (93)$$

Note, however, that the block-diagonal non-interacting Hamiltonian in Eq. (59) remains unchanged. To obtain the band structure and Fermi surfaces in the folded zone, one only needs to change the coordinates according to Eq. (87). Fig. 24 presents both the band dispersions and the Fermi pockets for this model in the folded zone. The meaning of the parameters  $\epsilon_1$  and  $\epsilon_3$  in Eqs. (47) and (54) is now evident: they are nothing but the energies of the two doublets at the  $\bar{M}$  point. Interestingly, these orbital-projected band models have generally three doublets: two of them arising from the  $\bar{M}_1$  and  $\bar{M}_3$  two-dimensional irreducible representations at the  $\bar{M}$  point and one arising from the  $E_g$  two-dimensional irreducible representation at the  $\bar{\Gamma}$  point. These three doublets form the two  $\Gamma$  hole pockets and the two  $X, Y$  electron pockets in the unfolded zone. On the other hand, the additional

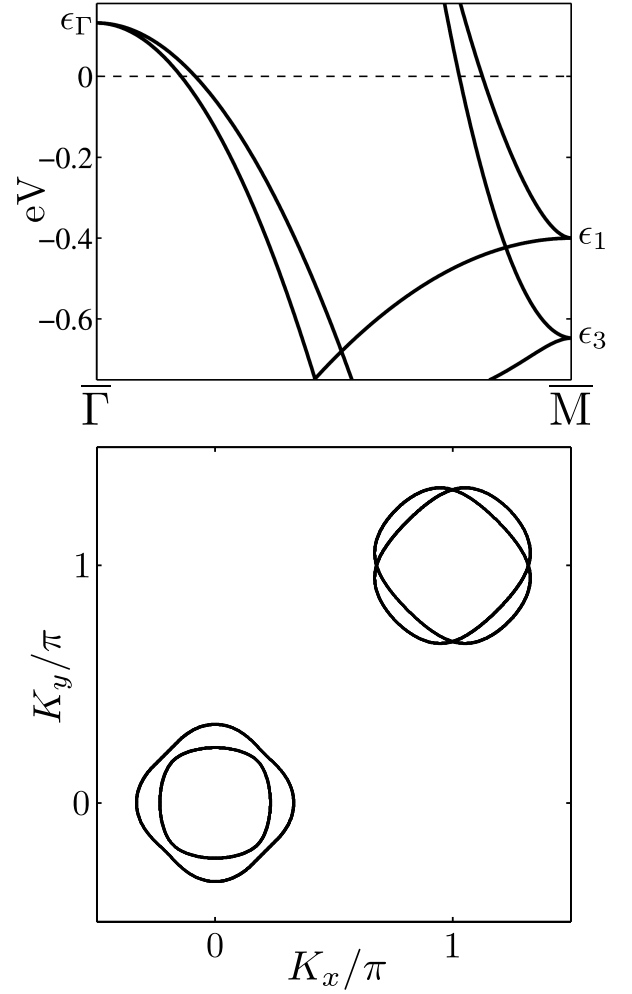


Figure 24. Band dispersion (upper panel) and Fermi surface (lower panel) of the orbital-projected band model in the folded BZ associated with the 2-Fe unit cell. Figure from Ref. [55].

hole pocket at the  $M$  point of the unfolded zone does not form a doublet, as it belongs to the one-dimensional  $B_{1g}$  irreducible representation at the  $\bar{\Gamma}$  point.

The advantages offered by the orbital-projected band model when dealing with the 2-Fe BZ become even more clear when one considers the effect of the spin-orbit coupling (SOC). As we discussed above, the pseudocrystal approach of the orbital-basis models works well as long as the glide-plane symmetry is kept intact, i.e. when there are no terms coupling states of the two different Fe sites of the unit cell. However, the atomic-like SOC alters this scenario, as it couples the  $d_{xy}$  states of one Fe site with the  $d_{xz/yz}$  states of the other Fe site of the unit cell via the  $\sigma_x$  and  $\sigma_y$  spin operators, see Eq. (89) above.

To account for SOC in the orbital-basis model, one has to work with  $10 \times 10$  matrices. On the other hand, in the orbital-projected band model, the SOC introduces off-diagonal terms into the non-interacting Hamiltonian (59) without increasing the number of low-energy degrees

of freedom. In particular, one finds [49, 164]:

$$\mathcal{H}_{\text{SOC}} = \sum_{\mathbf{k}} \Psi_{\mathbf{k}}^\dagger \hat{H}_{\text{SOC}}(\mathbf{k}) \Psi_{\mathbf{k}}, \quad (94)$$

with:

$$\hat{H}_{\text{SOC}}(\mathbf{k}) = \begin{pmatrix} 0 & h_M^{\text{SOC}}(\mathbf{k}) & 0 \\ (h_M^{\text{SOC}}(\mathbf{k}))^\dagger & 0 & 0 \\ 0 & 0 & h_\Gamma^{\text{SOC}}(\mathbf{k}) \end{pmatrix} \quad (95)$$

and  $4 \times 4$  matrices:

$$\begin{aligned} h_\Gamma^{\text{SOC}}(\mathbf{k}) &= \frac{1}{2} \lambda (\tau^y \otimes \sigma^z) \\ h_M^{\text{SOC}}(\mathbf{k}) &= \frac{i}{2} \lambda (\tau^+ \otimes \sigma^x + \tau^- \otimes \sigma^y) \end{aligned} \quad (96)$$

Here,  $\tau^\pm = \frac{1}{2}(\tau^x \pm i\tau^y)$  and the Pauli matrices  $\sigma$  refer to spin space, whereas  $\tau$  refer to spinor space. The SOC has very important consequences for the electronic properties of the FeSC. While it splits the degeneracy between the  $d_{xz}$  and  $d_{yz}$  orbitals at the  $\bar{\Gamma}$  point, it preserves the doublets at the  $\bar{M}$  point. This feature allows one to distinguish signatures of nematic order and SOC in the ARPES spectrum of the FeSC [164]. Note in this regard that the typical SOC observed experimentally is  $\lambda \sim 10$  meV [135], which is roughly of the same order as the band splittings due to SDW, SC, and orbital order. Thus, a consistent description of the normal state of the FeSC must account for the SOC.

The classification of the pairing states also change, as components identified with singlet and triplet pairing mix (although the Kramers degeneracy of the electronic states is kept intact by SOC) [49]. Finally, the SOC causes a spin anisotropy, which selects different magnetization directions for the different types of SDW order [55].

## VI. CONCLUDING REMARKS

In this work we reviewed the hierarchy of potential instabilities in FeSC by analyzing different low-energy models. We focused primarily on the interplay between superconductivity, SDW order,  $\mathbf{Q} = 0$  charge Pomeranchuk order (often associated with orbital order), and Ising-nematic spin order. The last two orders break  $C_4$  symmetry and lead to the phase dubbed nematic. We considered three sets of models: (i) Purely orbital models, in which all computations are performed within the orbital basis without separation into contributions from low-energy and high-energy sectors. (ii) Band models, in which the instabilities are viewed as coming from states near the Fermi surface, but the orbital composition of the Fermi surfaces is neglected. (iii) Orbital-projected band models, in which the analysis is restricted to low energies, but the orbital composition of the Fermi pockets is fully embraced. In our view, the last class of models are

the most promising ones due to their simplicity and due to the separation between high-energy and low-energy states.

The orbital-projected band models involve three orbitals ( $d_{xz}$ ,  $d_{yz}$ , and  $d_{xy}$ ) from which the low-energy excitations are constructed. The interactions between low-energy states contain angle-dependent prefactors that reflect the orbital composition of the Fermi surfaces. The full five-pocket orbital-projected model is rather involved and contains 40 distinct coupling constants. The analysis involving the RG technique, however, yields similar results in different approximated orbital-projected band models. Namely, at intermediate energies, magnetic fluctuations are the strongest. These fluctuations give rise to attractive interactions in  $s^{+-}$  and  $d$ -wave superconducting channels, as well as in  $s^{+-}$  and  $d$ -wave Pomeranchuk channels. Once interactions in these two channels become attractive, SC fluctuations compete with magnetic fluctuations and eventually win over them, while Pomeranchuk fluctuations develop with little competition with SDW. The final outcome, i.e. which order develops first, depends on the details of the electronic dispersion. For certain system parameters, the leading symmetry-breaking instability is in the  $\mathbf{Q} = 0$   $d$ -wave Pomeranchuk channel, which gives rise to spontaneous orbital order, the subleading instability is in the SC channel, and SDW order does not develop. For other system parameters, however, the leading instability is either SDW or superconductivity, while spontaneous orbital order does not develop. In this last case, the nematic order is a vestigial order of the stripe SDW state.

We also discussed the description of the physics in the 1-Fe and 2-Fe BZ, and the importance of the sizable spin-orbit coupling, which significantly affects the normal state and superconducting state properties. We argued that the orbital-projected models are very convenient to study the problem in the crystallographic 2Fe BZ, as they do not require the inclusion of additional electronic degrees of freedom. This is in contrast to orbital-basis models, in which the number of electronic degrees of freedom doubles.

We believe that the approach we reviewed in this paper is a promising framework to obtain a unified description of different Fe-based superconductors.

## ACKNOWLEDGMENTS

We thank B. Andersen, E. Bascones, L. Benfatto, E. Berg, L. Classen, M. Christensen, E. Dagotto, I. Eremin, L. Fanfarillo, M. Gastiasoro, P. Hirschfeld, C. Honerkamp, J. Kang, S. Kivelson, M. Khodas, H. Kontani, G. Kotliar, S. Maiti, I. Mazin, A. Millis, A. Moreo, I. Paul, R. Thomale, J. Schmalian, M. Schuett, O. Vafek, R. Valenti, B. Valenzuela, R. Xing, X. Wang, and Y. Wang for useful discussions. We would like to give special thanks to M. Christensen and J. Kang for assistance in producing some of the figures in this review. This work

was supported by the Office of Basic Energy Sciences, (AVC) and de-sc0012336 (RMF).  
U.S. Department of Energy, under awards de-sc0014402

## Appendix A: Band dispersion parameters

Here we explicitly present band dispersion parameters for selected models discussed in the main text.

### 1. Five-orbital model

We use the same notation of the Graser *et al* [12]. Note that in Fig. 3 of the main text, we used the parameters of the model of Ikeda *et al.*, which contains many more neighbor hoppings [18]. The tight binding parametrization is given by:

$$\begin{aligned}
\epsilon_{xz,xz}(\mathbf{k}) &= \epsilon_{xz}^{(0)} + 2t_x^{11} \cos k_x + 2t_y^{11} \cos k_y + 4t_{xy}^{11} \cos k_x \cos k_y + 2t_{xx}^{11} (\cos 2k_x - \cos 2k_y) \\
&\quad + 4t_{xy}^{11} \cos 2k_x \cos k_y + 4t_{xy}^{11} \cos k_x \cos 2k_y + 4t_{xxyy}^{11} \cos 2k_x \cos 2k_y, \\
\epsilon_{yz,yz}(\mathbf{k}) &= \epsilon_{yz}^{(0)} + 2t_y^{11} \cos k_x + 2t_x^{11} \cos k_y + 4t_{xy}^{11} \cos k_x \cos k_y - 2t_{xx}^{11} (\cos 2k_x - \cos 2k_y) \\
&\quad + 4t_{xy}^{11} \cos 2k_x \cos k_y + 4t_{xy}^{11} \cos k_x \cos 2k_y + 4t_{xxyy}^{11} \cos 2k_x \cos 2k_y, \\
\epsilon_{x^2-y^2,x^2-y^2}(\mathbf{k}) &= \epsilon_{x^2-y^2}^{(0)} + 2t_x^{33} (\cos k_x + \cos k_y) + 4t_{xy}^{33} \cos k_x \cos k_y + 2t_{xx}^{33} (\cos 2k_x + \cos 2k_y), \\
\epsilon_{xy,xy}(\mathbf{k}) &= \epsilon_{xy}^{(0)} + 2t_x^{44} (\cos k_x + \cos k_y) + 4t_{xy}^{44} \cos k_x \cos k_y + 2t_{xx}^{44} (\cos 2k_x + \cos 2k_y) \\
&\quad + 4t_{xy}^{44} (\cos 2k_x \cos k_y + \cos k_x \cos 2k_y) + 4t_{xxyy}^{44} \cos 2k_x \cos 2k_y, \\
\epsilon_{z^2,z^2}(\mathbf{k}) &= \epsilon_{z^2}^{(0)} + 2t_x^{55} (\cos k_x + \cos k_y) + 2t_{xx}^{55} (\cos 2k_x \cos 2k_y) \\
&\quad + 4t_{xxyy}^{55} (\cos 2k_x \cos k_y + \cos k_x \cos 2k_y) + 4t_{xxyy}^{55} \cos 2k_x \cos 2k_y, \\
\epsilon_{xz,yz}(\mathbf{k}) &= -4t_{xy}^{12} \sin k_x \sin k_y - 4t_{xxyy}^{12} (\sin 2k_x \sin k_y + \sin k_x \sin 2k_y) - 4t_{xxyy}^{12} \sin 2k_x \sin 2k_y, \\
\epsilon_{xz,x^2-y^2}(\mathbf{k}) &= i2t_{xy}^{13} \sin k_y + i4t_{xy}^{13} \cos k_x \sin k_y - i4t_{xxyy}^{13} (\cos k_x \sin 2k_y - \cos 2k_x \sin k_y), \\
\epsilon_{xz,xy}(\mathbf{k}) &= i2t_x^{14} \sin k_x + i4t_{xy}^{14} \sin k_x \cos k_y + i4t_{xxyy}^{14} \sin 2k_x \cos k_y, \\
\epsilon_{xz,z^2}(\mathbf{k}) &= i2t_x^{15} \sin k_y - i4t_{xy}^{15} \cos k_x \sin k_y - i4t_{xxyy}^{15} \cos 2k_x \sin 2k_y, \\
\epsilon_{yz,x^2-y^2}(\mathbf{k}) &= -i2t_x^{13} \sin k_x - i4t_{xy}^{13} \sin k_x \cos k_y + i4t_{xxyy}^{13} (\sin 2k_x \cos k_y - \sin k_x \cos 2k_y), \\
\epsilon_{yz,xy}(\mathbf{k}) &= i2t_x^{14} \sin k_y + i4t_{xy}^{14} \cos k_x \sin k_y + i4t_{xxyy}^{14} \cos k_x \sin 2k_y, \\
\epsilon_{yz,z^2}(\mathbf{k}) &= i2t_x^{15} \sin k_x - i4t_{xy}^{15} \sin k_x \cos k_y - i4t_{xxyy}^{15} \sin 2k_x \cos 2k_y, \\
\epsilon_{x^2-y^2,xy}(\mathbf{k}) &= 4t_{xxyy}^{34} (\sin k_x \sin 2k_y - \sin 2k_x \sin k_y), \\
\epsilon_{x^2-y^2,z^2}(\mathbf{k}) &= 2t_x^{35} (\cos k_x - \cos k_y) + 4t_{xxyy}^{35} (\cos 2k_x \cos k_y - \cos k_x \cos 2k_y), \\
\epsilon_{xy,z^2}(\mathbf{k}) &= 4t_{xy}^{45} \sin k_x \sin k_y + 4t_{xxyy}^{45} \sin 2k_x \sin 2k_y
\end{aligned} \tag{A1}$$

The tight-binding hopping parameters from Graser *et al.* are given in Table I. For an occupation number of 6, the onsite energies are given by:  $\epsilon_{xz}^{(0)} = \epsilon_{yz}^{(0)} = 130$  meV,  $\epsilon_{x^2-y^2}^{(0)} = -220$  meV,  $\epsilon_{xy}^{(0)} = 300$  meV, and  $\epsilon_{z^2}^{(0)} = -211$  meV.

### 2. Two-orbital model

The band dispersion in the two orbital model by Raghu *et al.* is [38]:

$$\begin{aligned}
\epsilon_{xx}(\mathbf{k}) &= -2t_1 \cos k_x - 2t_2 \cos k_y - 4t_3 \cos k_x \cos k_y \\
\epsilon_{yy}(\mathbf{k}) &= -2t_2 \cos k_x - 2t_1 \cos k_y - 4t_3 \cos k_x \cos k_y \\
\epsilon_{xy}(\mathbf{k}) &= -4t_4 \sin k_x \sin k_y
\end{aligned} \tag{A2}$$

$t_{\alpha}^{\mu\nu}$	$\alpha = x$	$\alpha = y$	$\alpha = xy$	$\alpha = xx$	$\alpha = xxy$	$\alpha = xyy$	$\alpha = xxyy$
$(\mu, \nu) = (xz, xz)$	-140	-400	280	20	-35	5	35
$(\mu, \nu) = (x^2 - y^2, x^2 - y^2)$	350	X	-105	-20	X	X	X
$(\mu, \nu) = (xy, xy)$	X	X	150	-30	-30	X	-30
$(\mu, \nu) = (z^2, z^2)$	X	X	X	-40	20	X	-10
$(\mu, \nu) = (xz, yz)$	X	X	50	X	-15	X	35
$(\mu, \nu) = (xz, x^2 - y^2)$	-354	X	99	X	21	X	X
$(\mu, \nu) = (xz, xy)$	339	X	14	X	28	X	X
$(\mu, \nu) = (xz, z^2)$	-198	X	-85	X	X	X	-14
$(\mu, \nu) = (x^2 - y^2, xy)$	X	X	X	X	-10	X	X
$(\mu, \nu) = (x^2 - y^2, z^2)$	-300	X	X	X	-20	X	X
$(\mu, \nu) = (xy, z^2)$	X	X	-150	X	X	X	10

Table I. Tight-binding hopping parameters (in meV) for the 5-orbital of Eq. (A1).

The tight-binding parameters used in Fig. 5 are taken from Ref. [39] and shown in Table II. For an occupation number of 2, the chemical potential is  $\mu = 550$  meV.

$t_1$	$t_2$	$t_3$	$t_4$
-330	385	-234	-260

Table II. Tight-binding hopping parameters (in meV) for the 2-orbital model of Eq. (A2).

### 3. Three-orbital model

The band dispersion in the three orbital model by Daghofer *et al.* is [53]:

$$\begin{aligned}
\epsilon_{xz,xz}(\mathbf{k}) &= -2t_1 \cos k_x - 2t_2 \cos k_y - 4t_3 \cos k_x \cos k_y \\
\epsilon_{yz,yz}(\mathbf{k}) &= -2t_2 \cos k_x - 2t_1 \cos k_y - 4t_3 \cos k_x \cos k_y \\
\epsilon_{xy,xy}(\mathbf{k}) &= -2t_5 (\cos k_x + \cos k_y) - 4t_6 \cos k_x \cos k_y + \Delta_{\text{CF}} \\
\epsilon_{xz,yz}(\mathbf{k}) &= -4t_4 \sin k_x \sin k_y \\
\epsilon_{xz,xy}(\mathbf{k}) &= -2it_7 \sin k_x - 4it_8 \sin k_x \cos k_y \\
\epsilon_{yz,xy}(\mathbf{k}) &= -2it_7 \sin k_y - 4it_8 \sin k_y \cos k_x
\end{aligned} \tag{A3}$$

The tight-binding parameters are shown in Table II. For an occupation number of 4, the chemical potential is  $\mu = 212$  meV and the crystal field splitting is  $\Delta_{\text{CF}} = 400$  meV.

$t_1$	$t_2$	$t_3$	$t_4$	$t_5$	$t_6$	$t_7$	$t_8$
-60	-20	-30	10	-200	-300	200	-100

Table III. Tight-binding hopping parameters (in meV) for the 3-orbital model of Eq. (A2).

### 4. Orbital-projected band model

The band dispersion in the model by Vafeek *et al.* is described in terms of the non-interacting Hamiltonian [49]:

$$\hat{H}_0(\mathbf{k}) = \begin{pmatrix} h_Y(\mathbf{k}) & 0 & 0 \\ 0 & h_X(\mathbf{k}) & 0 \\ 0 & 0 & h_\Gamma(\mathbf{k}) \end{pmatrix} \tag{A4}$$

with:

$$\begin{aligned}
h_Y(\mathbf{k}) &= \begin{pmatrix} \epsilon_1 + \frac{k^2}{2m_1} + a_1 k^2 \cos 2\theta & -iv_Y(\mathbf{k}) \\ iv_Y(\mathbf{k}) & \epsilon_3 + \frac{k^2}{2m_3} + a_3 k^2 \cos 2\theta \end{pmatrix} \otimes \sigma^0 \\
h_X(\mathbf{k}) &= \begin{pmatrix} \epsilon_1 + \frac{k^2}{2m_1} - a_1 k^2 \cos 2\theta & -iv_X(\mathbf{k}) \\ iv_X(\mathbf{k}) & \epsilon_3 + \frac{k^2}{2m_3} - a_3 k^2 \cos 2\theta \end{pmatrix} \otimes \sigma^0 \\
h_\Gamma(\mathbf{k}) &= \begin{pmatrix} \epsilon_\Gamma + \frac{k^2}{2m_\Gamma} + bk^2 \cos 2\theta & ck^2 \sin 2\theta \\ ck^2 \sin 2\theta & \epsilon_\Gamma + \frac{k^2}{2m_\Gamma} - bk^2 \cos 2\theta \end{pmatrix} \otimes \sigma^0
\end{aligned} \tag{A5}$$

and:

$$\begin{aligned}
v_X(\mathbf{k}) &= 2k \sin \theta [v + p_1 k^2 (2 + \cos 2\theta) - p_2 k^2 \cos 2\theta] \\
v_Y(\mathbf{k}) &= 2k \cos \theta [v + p_1 k^2 (2 - \cos 2\theta) + p_2 k^2 \cos 2\theta]
\end{aligned} \tag{A6}$$

Here,  $k$  is given in units of the inverse lattice constant of the 1-Fe unit cell. To obtain a better description of the Fermi surface, cubic terms are included in  $v_X$  and  $v_Y$ , while in the discussion in the main text we considered only linear terms. All the figures in the main text refer to the dispersions with the cubic terms present. The dispersion parameters are presented in Table IV. The chemical potential is set to  $\mu = 0$ .

$\epsilon_\Gamma$	$\epsilon_1$	$\epsilon_3$	$\frac{1}{2m_\Gamma}$	$\frac{1}{2m_1}$	$\frac{1}{2m_3}$	$a_1$	$a_3$	$b$	$c$	$v$	$p_1$	$p_2$
132	-400	-647	-368	298	634	419	-533	56.5	124.6	-243	-40	10

Table IV. Band dispersion parameters (in meV) for the band-orbital model of Eq. (A5).

- 
- |  |   |
|--|---|
| <p>[1] Y. Kamihara, T. Watanabe, M. Hirano, and H. Hosono, <i>Journal of the American Chemical Society</i> <b>130</b>, 3296 (2008).</p> <p>[2] M. Rotter, M. Tegel, and D. Johrendt, <i>Phys. Rev. Lett.</i> <b>101</b>, 107006 (2008).</p> <p>[3] K. Ishida, Y. Nakai, and H. Hosono, <i>Journal of the Physical Society of Japan</i> <b>78</b>, 062001 (2009).</p> <p>[4] D. C. Johnston, <i>Advances in Physics</i> <b>59</b>, 803 (2010).</p> <p>[5] J. Paglione and R. L. Greene, <i>Nature Physics</i> <b>6</b>, 645 (2010).</p> <p>[6] G. R. Stewart, <i>Rev. Mod. Phys.</i> <b>83</b>, 1589 (2011).</p> <p>[7] R. M. Fernandes, A. V. Chubukov, and J. Schmalian, <i>Nature Physics</i> <b>10</b>, 97 (2014).</p> <p>[8] P. J. Hirschfeld, M. M. Korshunov, and I. I. Mazin, <i>Reports on Progress in Physics</i> <b>74</b>, 124508 (2011).</p> <p>[9] A. Chubukov, <i>Annual Review of Condensed Matter Physics</i> <b>3</b>, 57 (2012).</p> <p>[10] A. Chubukov, "Itinerant electron scenario," in <i>Iron-Based Superconductivity</i>, edited by D. P. Johnson, G. Xu, and W.-G. Yin (Springer International Publishing, Cham, 2015) pp. 255–329.</p> <p>[11] V. Cvetkovic and Z. Tesanovic, <i>EPL (Europhysics Letters)</i> <b>85</b>, 37002 (2009).</p> <p>[12] S. Graser, T. A. Maier, P. J. Hirschfeld, and D. J. Scalapino, <i>New Journal of Physics</i> <b>11</b>, 025016 (2009).</p> <p>[13] I. A. Nekrasov, Z. V. Pchelkina, and M. V. Sadvovskii,</p> | <p><i>JETP Letters</i> <b>88</b>, 144 (2008).</p> <p>[14] M. J. Calderón, B. Valenzuela, and E. Bascones, <i>Phys. Rev. B</i> <b>80</b>, 094531 (2009).</p> <p>[15] H. Eschrig and K. Koepf, <i>Phys. Rev. B</i> <b>80</b>, 104503 (2009).</p> <p>[16] O. Andersen and L. Boeri, <i>Annalen der Physik</i> <b>523</b>, 8 (2011).</p> <p>[17] K. Kuroki, S. Onari, R. Arita, H. Usui, Y. Tanaka, H. Kontani, and H. Aoki, <i>Phys. Rev. Lett.</i> <b>101</b>, 087004 (2008).</p> <p>[18] H. Ikeda, R. Arita, and J. Kuneš, <i>Phys. Rev. B</i> <b>81</b>, 054502 (2010).</p> <p>[19] C. Mirri, A. Dusza, S. Bastelberger, M. Chinotti, L. Degiorgi, J.-H. Chu, H.-H. Kuo, and I. R. Fisher, <i>Phys. Rev. Lett.</i> <b>115</b>, 107001 (2015).</p> <p>[20] K. Seo, B. A. Bernevig, and J. Hu, <i>Phys. Rev. Lett.</i> <b>101</b>, 206404 (2008).</p> <p>[21] Q. Si and E. Abrahams, <i>Phys. Rev. Lett.</i> <b>101</b>, 076401 (2008).</p> <p>[22] F. Krüger, S. Kumar, J. Zaanen, and J. van den Brink, <i>Phys. Rev. B</i> <b>79</b>, 054504 (2009).</p> <p>[23] R. Applegate, R. R. P. Singh, C.-C. Chen, and T. P. Devereaux, <i>Phys. Rev. B</i> <b>85</b>, 054411 (2012).</p> <p>[24] W.-G. Yin, C.-C. Lee, and W. Ku, <i>Phys. Rev. Lett.</i> <b>105</b>, 107004 (2010).</p> <p>[25] P. Dai, J. Hu, and E. Dagotto, <i>Nature Physics</i> <b>8</b>, 709</p> |
|--|---|

- (2012).
- [26] R. Yu and Q. Si, Phys. Rev. B **86**, 085104 (2012).
  - [27] P. Richard, T. Qian, and H. Ding, Journal of Physics: Condensed Matter **27**, 293203 (2015).
  - [28] M. Aichhorn, L. Pourovskii, V. Vildosola, M. Ferrero, O. Parcollet, T. Miyake, A. Georges, and S. Biermann, Phys. Rev. B **80**, 085101 (2009).
  - [29] Z. Yin, K. Haule, and G. Kotliar, Nature materials **10**, 932 (2011).
  - [30] A. Georges, L. d. Medici, and J. Mravlje, Annu. Rev. Condens. Matter Phys. **4**, 137 (2013).
  - [31] L. de' Medici, G. Giovannetti, and M. Capone, Phys. Rev. Lett. **112**, 177001 (2014).
  - [32] S. Backes, H. O. Jeschke, and R. Valentí, Phys. Rev. B **92**, 195128 (2015).
  - [33] E. Bascones, B. Valenzuela, and M. J. Calderón, Comptes Rendus Physique **17**, 36 (2016).
  - [34] L. de' Medici, "Weak and strong correlations in Fe superconductors," in *Iron-Based Superconductivity*, edited by D. P. Johnson, G. Xu, and W.-G. Yin (Springer International Publishing, Cham, 2015) pp. 409–441.
  - [35] K. Kuroki, H. Usui, S. Onari, R. Arita, and H. Aoki, Phys. Rev. B **79**, 224511 (2009).
  - [36] P. C. Canfield and S. L. Bud'ko, Annu. Rev. Condens. Matter Phys. **1**, 27 (2010).
  - [37] H.-H. Wen and S. Li, Annual Review of Condensed Matter Physics **2**, 121 (2011).
  - [38] S. Raghu, X.-L. Qi, C.-X. Liu, D. J. Scalapino, and S.-C. Zhang, Phys. Rev. B **77**, 220503 (2008).
  - [39] R. Sknepnek, G. Samolyuk, Y.-b. Lee, and J. Schmalian, Phys. Rev. B **79**, 054511 (2009).
  - [40] A. Moreo, M. Daghofer, J. A. Riera, and E. Dagotto, Phys. Rev. B **79**, 134502 (2009).
  - [41] Y. Ran, F. Wang, H. Zhai, A. Vishwanath, and D.-H. Lee, Phys. Rev. B **79**, 014505 (2009).
  - [42] P. Ghaemi and A. Vishwanath, Phys. Rev. B **83**, 224513 (2011).
  - [43] L. Pan, J. Li, Y.-Y. Tai, M. J. Graf, J.-X. Zhu, and C. S. Ting, Phys. Rev. B **88**, 214510 (2013).
  - [44] H. Yamase and R. Zeyher, Phys. Rev. B **88**, 180502 (2013).
  - [45] Z. Wang and A. H. Nevidomskyy, Journal of Physics: Condensed Matter **27**, 225602 (2015).
  - [46] T. Ong, P. Coleman, and J. Schmalian, Proceedings of the National Academy of Sciences **113**, 5486 (2016).
  - [47] P. T. Dumitrescu, M. Serbyn, R. T. Scalettar, and A. Vishwanath, arXiv:1512.08523 (2015).
  - [48] A. V. Chubukov and R.-Q. Xing, Phys. Rev. B **93**, 165141 (2016).
  - [49] V. Cvetkovic and O. Vafek, Phys. Rev. B **88**, 134510 (2013).
  - [50] J. Ferber, K. Foyevtsova, R. Valentí, and H. O. Jeschke, Phys. Rev. B **85**, 094505 (2012).
  - [51] F. Hardy, A. E. Böhrer, D. Aoki, P. Burger, T. Wolf, P. Schweiss, R. Heid, P. Adelmann, Y. X. Yao, G. Kotliar, J. Schmalian, and C. Meingast, Phys. Rev. Lett. **111**, 027002 (2013).
  - [52] P. A. Lee and X.-G. Wen, Phys. Rev. B **78**, 144517 (2008).
  - [53] M. Daghofer, A. Nicholson, A. Moreo, and E. Dagotto, Phys. Rev. B **81**, 014511 (2010).
  - [54] M. N. Gastiasoro and B. M. Andersen, Phys. Rev. B **92**, 140506 (2015).
  - [55] M. H. Christensen, J. Kang, B. M. Andersen, I. Eremin, and R. M. Fernandes, Phys. Rev. B **92**, 214509 (2015).
  - [56] Z. Yin, K. Haule, and G. Kotliar, Nature Physics **10**, 845 (2014).
  - [57] F. Ahn, I. Eremin, J. Knolle, V. B. Zabolotnyy, S. V. Borisenko, B. Büchner, and A. V. Chubukov, Phys. Rev. B **89**, 144513 (2014).
  - [58] I. I. Mazin, D. J. Singh, M. D. Johannes, and M. H. Du, Phys. Rev. Lett. **101**, 057003 (2008).
  - [59] A. V. Chubukov, D. V. Efremov, and I. Eremin, Phys. Rev. B **78**, 134512 (2008).
  - [60] H. Kontani and S. Onari, Phys. Rev. Lett. **104**, 157001 (2010).
  - [61] C.-C. Lee, W.-G. Yin, and W. Ku, Phys. Rev. Lett. **103**, 267001 (2009).
  - [62] C.-C. Chen, J. Maciejko, A. P. Sorini, B. Moritz, R. R. P. Singh, and T. P. Devereaux, Phys. Rev. B **82**, 100504 (2010).
  - [63] W. Lv, F. Krüger, and P. Phillips, Phys. Rev. B **82**, 045125 (2010).
  - [64] W.-C. Lee and P. W. Phillips, Phys. Rev. B **86**, 245113 (2012).
  - [65] Y. Yamakawa, S. Onari, and H. Kontani, Phys. Rev. X **6**, 021032 (2016).
  - [66] S. Graser, A. F. Kemper, T. A. Maier, H.-P. Cheng, P. J. Hirschfeld, and D. J. Scalapino, Phys. Rev. B **81**, 214503 (2010).
  - [67] E. Bascones, M. J. Calderón, and B. Valenzuela, Phys. Rev. Lett. **104**, 227201 (2010).
  - [68] P. M. R. Brydon, M. Daghofer, and C. Timm, Journal of Physics: Condensed Matter **23**, 246001 (2011).
  - [69] Q. Luo and E. Dagotto, Phys. Rev. B **89**, 045115 (2014).
  - [70] S. Avcı, O. Chmaissem, J. Allred, S. Rosenkranz, I. Eremin, A. V. Chubukov, D. Bugaris, D. Chung, M. Kanatzidis, J.-P. Castellán, *et al.*, Nature Comm. **5**, 3845 (2014).
  - [71] A. Böhrer, F. Hardy, L. Wang, T. Wolf, P. Schweiss, and C. Meingast, Nature Comm. **6**, 7911 (2015).
  - [72] J. M. Allred, K. M. Taddei, D. E. Bugaris, M. J. Krogstad, S. H. Lapidus, D. Y. Chung, H. Claus, M. G. Kanatzidis, D. E. Brown, J. Kang, R. M. Fernandes, I. Eremin, S. Rosenkranz, O. Chmaissem, and R. Osborn, Nature Physics **12**, 493 (2016).
  - [73] T. Morinari, E. Kaneshita, and T. Tohyama, Phys. Rev. Lett. **105**, 037203 (2010).
  - [74] J. Knolle, I. Eremin, and R. Moessner, Phys. Rev. B **83**, 224503 (2011).
  - [75] D. J. Scalapino, Rev. Mod. Phys. **84**, 1383 (2012).
  - [76] L. Fanfarillo, A. Cortijo, and B. Valenzuela, Phys. Rev. B **91**, 214515 (2015).
  - [77] M. H. Christensen, J. Kang, B. M. Andersen, and R. M. Fernandes, Phys. Rev. B **93**, 085136 (2016).
  - [78] J. C. S. Davis and D.-H. Lee, Proceedings of the National Academy of Sciences **110**, 17623 (2013).
  - [79] J. Hu and H. Ding, Scientific reports **2**, 381 (2012).
  - [80] J. Hu, Phys. Rev. X **3**, 031004 (2013).
  - [81] S. Maiti and A. V. Chubukov, Phys. Rev. B **82**, 214515 (2010).
  - [82] P. M. R. Brydon and C. Timm, Phys. Rev. B **80**, 174401 (2009).
  - [83] R. M. Fernandes and J. Schmalian, Phys. Rev. B **82**, 014521 (2010).
  - [84] A. B. Vorontsov, M. G. Vavilov, and A. V. Chubukov, Phys. Rev. B **81**, 174538 (2010).
  - [85] I. Eremin and A. V. Chubukov, Phys. Rev. B **81**, 024511

- (2010).
- [86] R. M. Fernandes, A. V. Chubukov, J. Knolle, I. Eremin, and J. Schmalian, *Phys. Rev. B* **85**, 024534 (2012).
  - [87] P. M. R. Brydon, J. Schmiedt, and C. Timm, *Phys. Rev. B* **84**, 214510 (2011).
  - [88] U. Karahasanovic, F. Kretzschmar, T. Böhm, R. Hackl, I. Paul, Y. Gallais, and J. Schmalian, *Phys. Rev. B* **92**, 075134 (2015).
  - [89] J. Knolle, I. Eremin, J. Schmalian, and R. Moessner, *Phys. Rev. B* **84**, 180510 (2011).
  - [90] J. Kang and Z. Tešanović, *Phys. Rev. B* **83**, 020505 (2011).
  - [91] A. F. Kemper, T. A. Maier, S. Graser, H.-P. Cheng, P. J. Hirschfeld, and D. J. Scalapino, *New Journal of Physics* **12**, 073030 (2010).
  - [92] A. V. Chubukov and I. Eremin, *Phys. Rev. B* **82**, 060504 (2010).
  - [93] A. B. Vorontsov and I. Vekhter, *Phys. Rev. Lett.* **105**, 187004 (2010).
  - [94] M. Khodas and A. V. Chubukov, *Phys. Rev. B* **86**, 144519 (2012).
  - [95] R. M. Fernandes and A. J. Millis, *Phys. Rev. Lett.* **111**, 127001 (2013).
  - [96] L. Ortenzi, E. Cappelluti, L. Benfatto, and L. Pietronero, *Phys. Rev. Lett.* **103**, 046404 (2009).
  - [97] A. V. Chubukov, M. Khodas, and R. M. Fernandes, *arXiv:1602.05503* (2016).
  - [98] R. Thomale, C. Platt, J. Hu, C. Honerkamp, and B. A. Bernevig, *Phys. Rev. B* **80**, 180505 (2009).
  - [99] F. Wang, H. Zhai, Y. Ran, A. Vishwanath, and D.-H. Lee, *Phys. Rev. Lett.* **102**, 047005 (2009).
  - [100] F. Wang and D.-H. Lee, *Science* **332**, 200 (2011).
  - [101] C. Platt, W. Hanke, and R. Thomale, *Advances in Physics* **62**, 453 (2013).
  - [102] J. M. Murray and O. Vafek, *Phys. Rev. B* **89**, 205119 (2014).
  - [103] D. Podolsky, H.-Y. Kee, and Y. B. Kim, *EPL (Europhysics Letters)* **88**, 17004 (2009).
  - [104] A. V. Chubukov, R. M. Fernandes, and J. Schmalian, *Phys. Rev. B* **91**, 201105 (2015).
  - [105] R. M. Fernandes, D. K. Pratt, W. Tian, J. Zarestky, A. Kreyssig, S. Nandi, M. G. Kim, A. Thaler, N. Ni, P. C. Canfield, R. J. McQueeney, J. Schmalian, and A. I. Goldman, *Phys. Rev. B* **81**, 140501 (2010).
  - [106] J. Lorenzana, G. Seibold, C. Ortix, and M. Grilli, *Phys. Rev. Lett.* **101**, 186402 (2008).
  - [107] G. Giovannetti, C. Ortix, M. Marsman, M. Capone, J. van den Brink, and J. Lorenzana, *Nature communications* **2**, 398 (2011).
  - [108] X. Wang, J. Kang, and R. M. Fernandes, *Phys. Rev. B* **91**, 024401 (2015).
  - [109] R. M. Fernandes, S. A. Kivelson, and E. Berg, *Phys. Rev. B* **93**, 014511 (2016).
  - [110] X. Wang and R. M. Fernandes, *Phys. Rev. B* **89**, 144502 (2014).
  - [111] M. Hoyer, R. M. Fernandes, A. Levchenko, and J. Schmalian, *Phys. Rev. B* **93**, 144414 (2016).
  - [112] T.-M. Chuang, M. P. Allan, J. Lee, Y. Xie, N. Ni, S. L. Bud'ko, G. S. Boebinger, P. C. Canfield, and J. C. Davis, *Science* **327**, 181 (2010).
  - [113] M. Yi, D. Lu, J.-H. Chu, J. G. Analytis, A. P. Sorini, A. F. Kemper, B. Moritz, S.-K. Mo, R. G. Moore, M. Hashimoto, W.-S. Lee, Z. Hussain, T. P. Devereaux, I. R. Fisher, and Z.-X. Shen, *Proceedings of the National Academy of Sciences* **108**, 6878 (2011).
  - [114] J.-H. Chu, H.-H. Kuo, J. G. Analytis, and I. R. Fisher, *Science* **337**, 710 (2012).
  - [115] S. Kasahara, H. J. Shi, K. Hashimoto, S. Tonegawa, Y. Mizukami, T. Shibauchi, K. Sugimoto, T. Fukuda, T. Terashima, A. H. Nevidomskyy, and Y. Matsuda, *Nature* **486**, 382 (2012).
  - [116] Y. Gallais, R. M. Fernandes, I. Paul, L. Chauvière, Y.-X. Yang, M.-A. Méasson, M. Cazayous, A. Sacuto, D. Colson, and A. Forget, *Phys. Rev. Lett.* **111**, 267001 (2013).
  - [117] E. P. Rosenthal, E. F. Andrade, C. J. Arguello, R. M. Fernandes, L. Y. Xing, X. C. Wang, C. Q. Jin, A. J. Millis, and A. N. Pasupathy, *Nature Physics* **10**, 225 (2014).
  - [118] X. Lu, J. Park, R. Zhang, H. Luo, A. H. Nevidomskyy, Q. Si, and P. Dai, *Science* **345**, 657 (2014).
  - [119] A. E. Bohmer and C. Meingast, *Comptes Rendus Physique* **17**, 90 (2016).
  - [120] Y. Gallais and I. Paul, *Comptes Rendus Physique* **17**, 113 (2016).
  - [121] P. Chandra, P. Coleman, and A. I. Larkin, *Phys. Rev. Lett.* **64**, 88 (1990).
  - [122] C. Fang, H. Yao, W.-F. Tsai, J. Hu, and S. A. Kivelson, *Phys. Rev. B* **77**, 224509 (2008).
  - [123] C. Xu, M. Müller, and S. Sachdev, *Phys. Rev. B* **78**, 020501 (2008).
  - [124] M. D. Johannes and I. I. Mazin, *Phys. Rev. B* **79**, 220510 (2009).
  - [125] R. M. Fernandes, L. H. VanBebber, S. Bhattacharya, P. Chandra, V. Keppens, D. Mandrus, M. A. McGuire, B. C. Sales, A. S. Sefat, and J. Schmalian, *Phys. Rev. Lett.* **105**, 157003 (2010).
  - [126] S. Liang, A. Moreo, and E. Dagotto, *Phys. Rev. Lett.* **111**, 047004 (2013).
  - [127] Y. Qi and C. Xu, *Phys. Rev. B* **80**, 094402 (2009).
  - [128] J. Kang, A. F. Kemper, and R. M. Fernandes, *Phys. Rev. Lett.* **113**, 217001 (2014).
  - [129] F. Yang, F. Wang, and D.-H. Lee, *Phys. Rev. B* **88**, 100504 (2013).
  - [130] R. Thomale, C. Platt, W. Hanke, J. Hu, and B. A. Bernevig, *Phys. Rev. Lett.* **107**, 117001 (2011).
  - [131] J. Kang, X. Wang, A. V. Chubukov, and R. M. Fernandes, *Phys. Rev. B* **91**, 121104 (2015).
  - [132] G. Livanas, A. Aperis, P. Kotetes, and G. Varelogianis, *Phys. Rev. B* **91**, 104502 (2015).
  - [133] W.-C. Lee, S.-C. Zhang, and C. Wu, *Phys. Rev. Lett.* **102**, 217002 (2009).
  - [134] L. Fanfarillo, J. Mansart, P. Toulemonde, H. Cercellier, P. L. Fevre, F. Bertran, B. Valenzuela, L. Benfatto, and V. Brouet, *arXiv:1605.02482* (2016).
  - [135] S. Borisenko, D. Evtushinsky, Z.-H. Liu, I. Morozov, R. Kappenberger, S. Wurmehl, B. Büchner, A. Yaresko, T. Kim, M. Hoesch, *et al.*, *Nature Physics* **12**, 311 (2016).
  - [136] M. D. Watson, T. K. Kim, A. A. Haghighirad, N. R. Davies, A. McCollam, A. Narayanan, S. F. Blake, Y. L. Chen, S. Ghannadzadeh, A. J. Schofield, M. Hoesch, C. Meingast, T. Wolf, and A. I. Coldea, *Phys. Rev. B* **91**, 155106 (2015).
  - [137] A. Fedorov, A. Yaresko, T. Kim, E. Kushnirenko, E. Haubold, T. Wolf, M. Hoesch, A. Grueneis, B. Buechner, and S. Borisenko, *arXiv:1606.03022* (2016).
  - [138] A. V. Chubukov, M. G. Vavilov, and A. B. Vorontsov,

- Phys. Rev. B **80**, 140515 (2009).
- [139] R. S. Dhaka, S. E. Hahn, E. Razzoli, R. Jiang, M. Shi, B. N. Harmon, A. Thaler, S. L. Bud'ko, P. C. Canfield, and A. Kaminski, Phys. Rev. Lett. **110**, 067002 (2013).
  - [140] V. Brouet, P.-H. Lin, Y. Texier, J. Bobroff, A. Taleb-Ibrahimi, P. Le Fèvre, F. Bertran, M. Casula, P. Werner, S. Biermann, F. Rullier-Albenque, A. Forget, and D. Colson, Phys. Rev. Lett. **110**, 167002 (2013).
  - [141] K. Jiang, J. Hu, H. Ding, and Z. Wang, Phys. Rev. B **93**, 115138 (2016).
  - [142] Y. Su, H. Liao, and T. Li, Journal of Physics: Condensed Matter **27**, 105702 (2015).
  - [143] T. A. Maier, S. Graser, D. J. Scalapino, and P. J. Hirschfeld, Phys. Rev. B **79**, 224510 (2009).
  - [144] Y. Wang, A. Kreisel, V. B. Zabolotnyy, S. V. Borisenko, B. Büchner, T. A. Maier, P. J. Hirschfeld, and D. J. Scalapino, Phys. Rev. B **88**, 174516 (2013).
  - [145] S. Maiti, M. M. Korshunov, T. A. Maier, P. J. Hirschfeld, and A. V. Chubukov, Phys. Rev. Lett. **107**, 147002 (2011).
  - [146] T. Böhm, A. F. Kemper, B. Moritz, F. Kretschmar, B. Muschler, H.-M. Eiter, R. Hackl, T. P. Devereaux, D. J. Scalapino, and H.-H. Wen, Phys. Rev. X **4**, 041046 (2014).
  - [147] T. Saito, S. Onari, Y. Yamakawa, H. Kontani, S. V. Borisenko, and V. B. Zabolotnyy, Phys. Rev. B **90**, 035104 (2014).
  - [148] A. Abanov, A. V. Chubukov, and J. Schmalian, Advances in Physics **52**, 119 (2003).
  - [149] S. Baek, D. Efremov, J. Ok, J. Kim, J. van den Brink, and B. Büchner, Nature materials **14**, 210 (2015).
  - [150] A. E. Böhm, T. Arai, F. Hardy, T. Hattori, T. Iye, T. Wolf, H. v. Löhneysen, K. Ishida, and C. Meingast, Phys. Rev. Lett. **114**, 027001 (2015).
  - [151] K. Kothapalli, A. Böhm, W. Jayasekara, B. Ueland, P. Das, A. Sapkota, V. Taufour, Y. Xiao, E. Alp, S. Bud'ko, *et al.*, arXiv:1603.04135 (2016).
  - [152] T. Terashima, N. Kikugawa, S. Kasahara, T. Watashige, Y. Matsuda, T. Shibauchi, and S. Uji, Phys. Rev. B **93**, 180503 (2016).
  - [153] H. Zhai, F. Wang, and D.-H. Lee, Phys. Rev. B **80**, 064517 (2009).
  - [154] L. e. Classen, unpublished (2016).
  - [155] R. M. Fernandes, M. Khodas, and A. V. Chubukov, unpublished (2016).
  - [156] S. Onari and H. Kontani, Phys. Rev. Lett. **109**, 137001 (2012).
  - [157] A. Hinojosa, J. Cai, and A. V. Chubukov, Phys. Rev. B **93**, 075106 (2016).
  - [158] M. Khodas and A. V. Chubukov, Phys. Rev. Lett. **108**, 247003 (2012).
  - [159] C.-H. Lin, T. Berlijn, L. Wang, C.-C. Lee, W.-G. Yin, and W. Ku, Phys. Rev. Lett. **107**, 257001 (2011).
  - [160] M. Tomić, H. O. Jeschke, and R. Valentí, Phys. Rev. B **90**, 195121 (2014).
  - [161] C.-H. Lin, C.-P. Chou, W.-G. Yin, and W. Ku, arXiv:1403.3687 (2014).
  - [162] Y. Wang, T. Berlijn, P. J. Hirschfeld, D. J. Scalapino, and T. A. Maier, Phys. Rev. Lett. **114**, 107002 (2015).
  - [163] J. T. Park, D. S. Inosov, A. Yaresko, S. Graser, D. L. Sun, P. Bourges, Y. Sidis, Y. Li, J.-H. Kim, D. Haug, A. Ivanov, K. Hradil, A. Schneidewind, P. Link, E. Faulhaber, I. Glavatsky, C. T. Lin, B. Keimer, and V. Hinkov, Phys. Rev. B **82**, 134503 (2010).
  - [164] R. M. Fernandes and O. Vafek, Phys. Rev. B **90**, 214514 (2014).